X-Ray Detection Using Amorphous Silicon Technology

by

Koorosh Aflatooni

A thesis

presented to the University of Waterloo

in fulfilment of the

thesis requirement for the degree of

Doctor of Philosophy

in

Electrical Engineering

Waterloo, Ontario, Canada, 1998

The University of Waterloo requires the signatures of all persons using or photocopying this thesis. Please sign below, and give address and date.

.

.

Abstract

This thesis describes the design and fabrication of a novel direct-conversion X-ray detector based on Mo/a-Si:H Schottky diodes. The choice of Mo as a Schottky contact follows from its low stress, temperature stability, and relatively large X-ray absorption. Furthermore, it is compatible with the standard hydrogenated amorphous silicon (a-Si:H) thin film transistor (TFT) technology. Here, the TFTs are intended for use as switching elements in large area imaging applications.

Investigations of device stability at low bias suggest that the time dependent variations of reverse current can be attributed to the release of trapped charge in the amorphous material. Here, the instabilities in reverse current during X-ray detection is limited to less than 2.5%. Various experimental studies of noise characteristics in Mo/a-Si:H Schottky diodes show that flicker noise dominates at low frequencies, where the detectors are expected to be operated. Here, the noise current power spectral density has a quadratic dependence on reverse current.

X-ray sensitivity experiments, performed in a medical environment for a wide range of X-ray energies (40 to 100 kVp), show a linear response of the detector with respect to the number of absorbed X-ray photons. Analysis shows that detector sensitivity reaches its maximum for a Mo layer thickness of around 500 nm at 60 kVp. The impact of other geometric and bias conditions on the detector performance has also been studied.

Acknowledgements

I would like to express my special thanks to my supervisors, Professor Arokia Nathan, and Professor Richard Hornsey for their technical support, guidance, and encouragement. They were the voice of reason in moments of anxiety during my research.

I would like to thank Dr. Ian Cunningham, Robarts Research Institute, University of Western Ontario for numerous stimulating discussions, and help in providing the X-ray source and XRAYLIB computer program.

I am honored to have Professor B. Hobbs, Department of Radiology, University of Western Ontario as my external examiner, and my appreciation to the members of my PhD examination committee.

I would like to thank my colleagues and friends in the SiDIC group, ECE department, and Robarts Research Institute; Roger Grant for providing the necessary training in the fabrication laboratory; Paul Madeira for his help with the equipment; Ardeshir Namdar, Byung Park, Dr. R. V. R. Murthy, Dr. S. Mohajerzadeh, and Dr. A. Miri for numerous inspiring discussions; and M. Lee for access to the X-ray source.

Finally, I would like to express my deep gratitude to my family for their continuous support and encouragement. They were my source of moral support. Special thanks, to my wife, Mehrnaz, who was always there to patiently listen, and unselfishly put up with all the late nights, weekends, and holidays that I was working.

To My Wife,
      and My Parents

Contents

.

List of Tables

List of Figures

List of Symbols

A	Area
a	Tunneling parameter
a_h	Bohr's radius ($= 0.0529\ nm$)
A_w	Atomic weight
A^*	Richardson's constant
B	Bandwidth
c	Speed of light
C	Capacitance
C_1	Dispersive transport coefficient
C_2	Capture cross section
c_{Mo}	Heat capacity of Mo
d	Thickness
E	Energy
E_o	Electron rest energy ($= 0.511\ MeV$)
E_{bind}	Binding energy
E_B	Bremsstrahlung threshold energy
E_c	Energy level of conduction band
E_{fm}	Metal Fermi level
E_{K-edge}	Binding energy of K-shell electrons
E_{L-edge}	Binding energy of L-shell electrons
E_{qf}	Quasi Fermi level

f	Frequency
F	Electric field
ΔT	Electron energy loss
h	Planck's constant ($= 6.6256 \times 10^{-34}\ Nms$)
$\hbar$	Planck's constant/2π ($= 1.0545 \times 10^{-34}\ Nms$)
I	Intensity of beam
$< i^2 >$	Noise current power spectra density
I_{op}	Initial intensity of X-ray beam
I_p	Intensity of the X-ray beam
I_{abs}	Absorbed intensity
I_{ion}	The mean excitation energy
I_{ref}	Reflected fraction
I_{rev}	Reverse current
J_{TE}	Thermionic emission current
J_T	Tunneling current
J_{th}	Thermal generation reverse current
g_t	Density of band tail states
g_{to}	Density of band tail states on the bottom of conduction band ($\approx 10^{21}\ cm^{-3}eV^{-1}$)
g_d	Density of deep states
g_{do}	Density of deep states on the bottom of conduction band ($\approx 9.6 \times 10^{18}\ cm^{-3}eV^{-1}$)
K	Flicker noise parameter
k	Boltzman's constant

m_o	Rest mass of electron ($= 9.1095 \times 10^{-31}$ kg)
m^*	Effective mass of electrons
n_{abs}	Number of absorbed photons
n_c	Number of electrons in conduction band
N_D	Density of ionized centers
N_e	Number of atoms per gram
n_e	Number of transmitted electrons
n_{it}	Number of electrons trapped in i^{th} trap state
n_{inc}	Initial number of photons impinging on the surface
n_{oi}	Initial number of photoelectrons in ith energy interval
n_{max}	Maximum number of transmitted photoelectrons
N_{tot}	Total number of traps between two position of depletion region
n_{e-tot}	Total number of generated photoelectrons
P	Energy transfer to the medium
Q	Heat absorbed in film
q	Unit charge (1.6×10^{-19} C)
R	Resistance
R_{dynm}	Dynamic resistance
R_y	Rydberg constant ($= 13.6$ eV)
R_i	Trapping rate to the ith trap state

r_i	Release rate from i^{th} trap state
S	Stopping power
r_s	Average electron distance
T	Electron kinetic energy
T_o	Electron initial kinetic energy
$\|T\|^2$	Tunneling probability
t	Thickness of the film
t_{Mo}	Thickness of Mo film
t_{Si}	Thickness of Si film
u	Thermal energy
V	Voltage
v	Velocity
$< v^2 >$	Noise voltage
W	Empirical energy for creating one e-h pair
w	Depletion width
x	Distance
Z	Atomic number
α	Dispersive transport parameter $(= \theta/\theta_c)$
α_{opt}	Optical absorption coefficient
β	Velocity normalized to speed of light
β_e	Electron's stretched exponential parameter

β_h	Hole's stretched exponential parameter
δ	Density effect correction
ϵ_o	Dielectric constant of air (8.85×10^{-14} F/cm)
ϵ_{si}	Relative dielectric constant of silicon (11.9)
ϕ_o	Barrier height
ϕ_{eff}	Effective barrier height
θ	Temperature
θ_c	Characteristics temperature of tail states ($250 - 300$ K)
θ_{cut}	Cut off angle
θ_d	Characteristics temperature of deep states (1000 K)
θ_v	Characteristics temperature of tail states in valence band ($250 - 300$ K)
λ_e	Electron mean free path
λ_p	Photon mean free path
λ_s	Empirical constant ($= 0.182$)
μ_D	Drift mobility
ν	Photon frequency
ρ	Density
σ	Cross section
σ_{photo}	Photoelectric cross section
σ_{ion}	Ionization cross section
ω_o	Escape frequency (10^{12} s^{-1})

ω_p Plasmon frequency

$d\Omega$ Solid angle $(= 2\pi sin(\theta)d\theta)$

τ Transient time

τ_e Electron time constant

τ_h Hole time constant

Chapter 1

Introduction

X-rays were first discovered in 1895 by German physicist, W. K. Roentgen. Later, in the same year, he used a photographic film to capture an image of his wife's hand, the first X-ray image. Shortly after this discovery, X-ray technology found its way into hospitals all around the world. During the past century, there have been many studies which constructed our knowledge of production, interaction, and applications of X-rays in different areas. Radiology is a product of these studies, meeting the ever increasing demand for X-rays in medical applications, including diagnostics and treatment. Today, we use X-rays not only for medical imaging but also for industrial, security, and purely scientific purposes.

1.1   X-ray Radiation

X-rays, formed from electromagnetic radiation, can be emitted when atomic electrons change their atomic energy levels (fluorescence). X-rays can also be produced when energetic free electrons travel near a nucleus (Bremsstrahlung). Often X-rays are cate-

gorized by their energy ranges [1]:

0.1-20 keV	124-0.62 Å	Low-energy or soft X-rays
20-120 keV	0.62-0.1 Å	Diagnostic-range X-rays
120-300 keV	0.1-0.04 Å	Orthovoltage X-rays
300 keV- 1 MeV	0.04-0.01 Å	Intermediate-energy X-rays
1 MeV upwards	0.01- Å	Megavoltage X-rays.

X-ray photons are energetic and can penetrate deep within the material; their attenuation is greater in denser regions of the medium. The intensity distribution of X-rays after they pass through the medium, can reveal density variations in the material.

1.2 Conventional Methods for X-ray Imaging

Several methods have been developed to capture the information gathered by X-rays. Film, the first and the easiest method to capture X-ray intensity distributions, has seen tremendous sensitivity improvements over the past century. In modern applications, X-rays are converted to visible light using a phosphor material (such as Gd_2O_2S, $LaOBr$, or $Y_2O_2S : Tb$), and the generated image is then captured on photographic film.

Despite the advantages of the photographic method, there are several disadvantages:

- Storage and retrieval of information

- Limitations in image processing

- Difficulties in transferring information

- Chemical waste problems associated with the development of films

- Lack of real-time imaging capabilities.
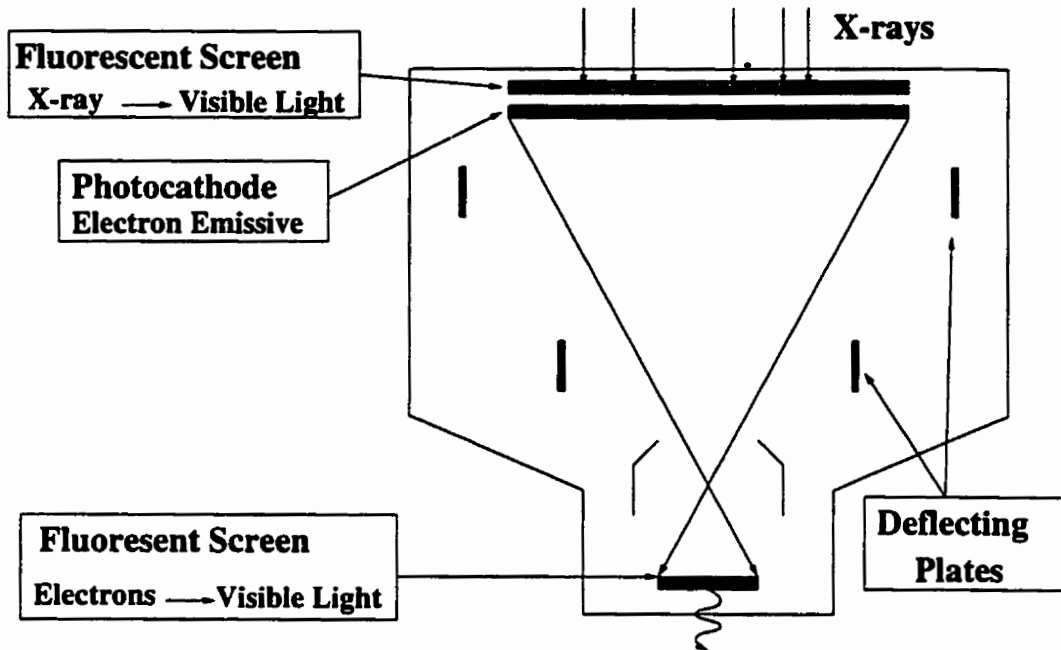
Figure 1.1: Schematic of an image intensifier.

Another widely used method for the X-ray imaging is based on image-intensifier tubes (Fig. 1.1). They can be integrated with a CCD camera. This combination allows for the real-time X-ray image sensing (fluoroscopy) that is essential for medical surgery applications. However, the problems associated with this method are:

- Bulky size of tubes

- Maintenance and high voltage requirements

- Relatively low quality images

- Significant capital and maintenance costs.

1.3 Motivation

Many of the issues attributed to the conventional X-ray imaging methods can be overcome with large area semiconductor X-ray image sensor arrays. These sensors offer the convenience of integration with external electronics, while providing capabilities, such as real time imaging, image processing, information storage, and retrieval. Moreover, these sensors can facilitate the transfer of information, which is highly desirable for remote diagnosis and treatment.

A semiconductor detector suitable for this purpose must have a high resistance to radiation damage. Additionally, the underlying fabrication technology must provide a large area deposition capability, such requirements are often not met by conventional crystalline semiconductor technologies.

Recent developments in large area flat panel active matrix liquid crystal displays (AMLCDs) have lead to development of a new technology based on hydrogenated amorphous silicon (a-Si:H). Indeed, the a-Si:H technology also offers a suitable platform for medical X-ray imaging. This mainly stems from a-Si:H capability for large area electronics [2, 3] and its resistance to radiation damage [4].

1.4 Other Detection Schemes

The potential applications of large area semiconductor X-ray image sensor arrays have generated a growing interest in this field. Detection schemes for medical X-rays, reported hitherto, are based on

- Direct detection methods, where the X-ray photon energy is directly converted into an electrical signal
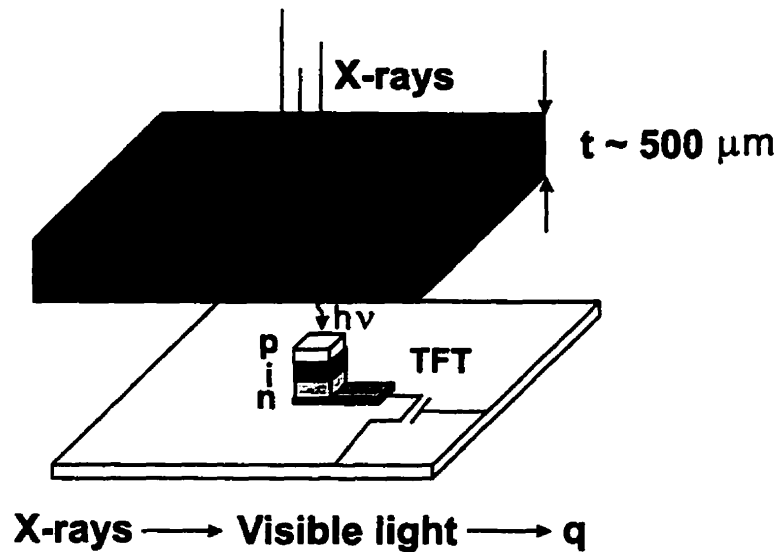
Figure 1.2: X-ray image sensor proposed by XEROX, based on combination of a phosphor layer and an a-Si:H image sensor.

- Indirect detection methods, where the X-ray photon energy is converted into visible light first by a phosphor layer and, subsequently, is sensed by photodetectors (Fig. 1.2).

Since 1985, there have been a number of reports on the fabrication and testing of X-ray imaging arrays [5, 6, 4, 7, 8, 9, 10, 11, 12, 13, 14], most of which rely on the indirect detection mechanism. The efficiency of indirect detection is determined by a number of factors, e.g., the efficiency of conversion of X-ray photons to visible light, the efficiency of the photodetectors in converting the visible light to a useful electrical signal (70-90%), and fill factor. The resolution of the indirect method depends on both the scattering of visible photons inside the scintillator layer and the dimensions of the sensing pixels.

Direct detection methods offer advantages in resolution and efficiency. Moreover, they do not depend on scintillation layers. There have been some efforts to implement X-ray image sensors based on the direct detection method using a thick amorphous sele-
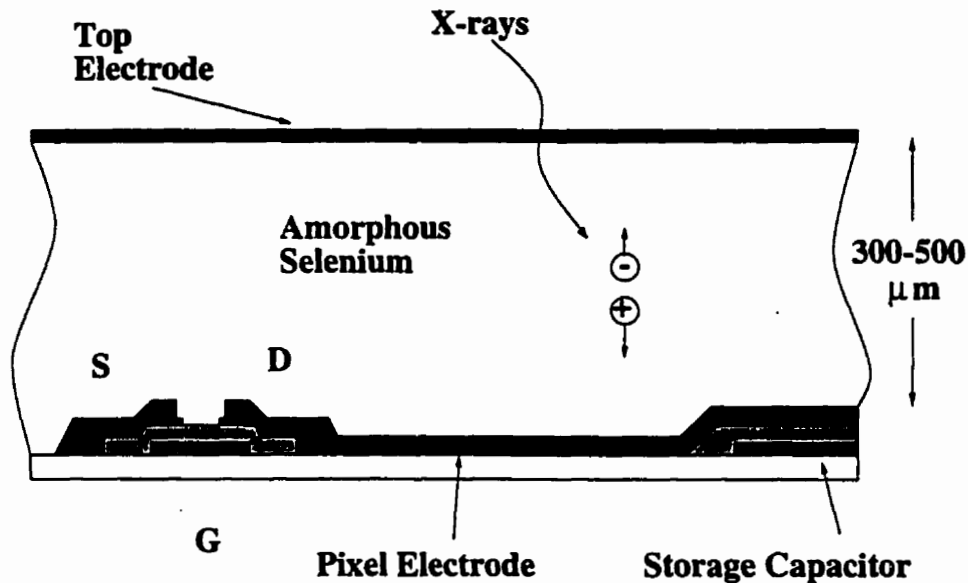
Figure 1.3: Schematic of X-ray detection using a thick amorphous selenium layer.

nium (a-Se) layer (Fig. 1.3) [15, 16, 17]. In this method, X-ray photons are absorbed in the a-Se layer, where their energies are transferred to generation of electron hole pairs (e-h). Subsequently, the e-h pairs are separated by an applied electric field and collected to form the signal. Despite the potentially high resolution of these image sensors, the thick selenium layer introduces severe problems in the collection of the generated charge. A strong electric field is often required for efficient charge collection, which is achieved by applying a bias as high as $4 - 10 \ kV$ across the a-Se layer. Furthermore, charge trapping in the a-Se layer leads to an image lag, which reduces the frame rate of the imaging array.

1.5   Detection Scheme Under Study

In this thesis, a direct detection scheme using heavy metal/a-Si:H Schottky diodes for low X-ray energies is presented. This detection method is based on the photoelectric
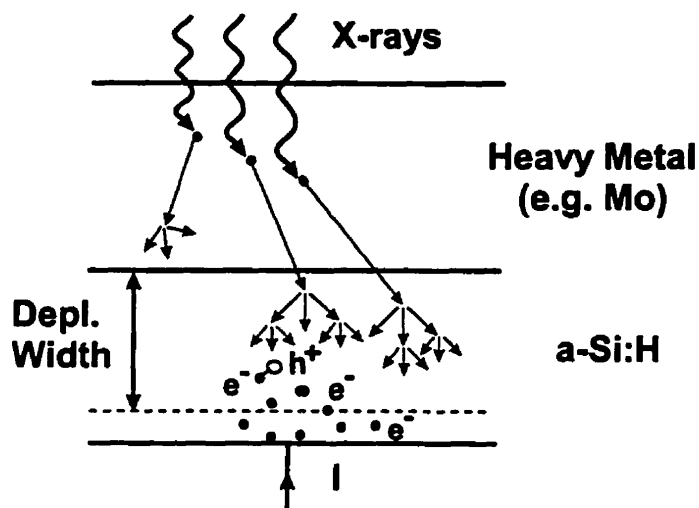
Figure 1.4: Schematic of the direct detection scheme proposed in this thesis.

interaction of X-ray photons with a heavy metal layer (e.g., Mo), and the ejection of energetic electrons into the a-Si:H layer (Fig. 1.4) [18, 19, 20, 21]. Inside the a-Si:H layer, the energetic electrons undergo various scattering events, thus transferring their energies to the generation of multiple electron hole (e-h) pairs. The e-h pairs are then separated by the electric field inside the depletion region of the reverse biased Schottky diode, thereby forming the output signal. This detection scheme does not require any high voltage operation. The structure of the detectors is also fully compatible with the standard a-Si:H thin film transistors (TFTs), intended for use as switching elements.

For optimum detector performance, various material, electrical, and sensitivity aspects need to be considered. The fabrication conditions and the associated material properties are discussed in Chapter 2. These are critical in selecting a metal that not only gives a high X-ray absorption, but also yields desirable detector electrical characteristics, and full compatibility with the thin film transistor fabrication processes. An issue intrinsic to a-Si:H is metastability, and this could potentially undermine the sensitivity by the time

dependent variations of the reverse current. Instability mechanisms and identification of optimum operating conditions are discussed in Chapter 3. The detection resolution is ultimately limited by the noise intrinsic to the device, particularly for operation at relatively low frequencies. Characterization of noise performance in the fabricated Schottky diodes is given in Chapter 4. The X-ray sensitivity of the fabricated Schottky diodes is discussed in Chapter 5, along with the influence of various geometric and operating parameters on the sensitivity.

Chapter 2

Fabrication

The advantages of amorphous silicon technology stem from its ability for large area and low temperature deposition, film uniformity, and use of a variety of possible substrates, such as glass or foil. However, these unique capabilities introduce new requirements and conditions, which are different from those of standard crystalline silicon technology. The various materials and process aspects involved with the fabrication of Schottky diodes are presented in this chapter. These aspects have a strong bearing on selection of a metal layer that meets various requirements, including high X-ray absorption, high Schottky barrier height, low leakage current, low built-in stress, and compatibility with the standard a-Si:H TFT process.

2.1 Material

The performance of any device strongly depends on the quality of the material and process conditions used in its fabrication. In this section, the deposition conditions used to prepare the Schottky diodes are presented, along with the associated characterization

results.

2.1.1 Amorphous Silicon Films

Amorphous silicon films can be prepared with a variety of deposition methods, e.g., chemical vapor deposition (CVD), plasma enhanced chemical vapor deposition (PECVD), or hot wire. The most widely used method to prepare device quality materials is PECVD. Here, the amorphous silicon is deposited by plasma assisted dissociation of silane (SiH_4) [22]. The low deposition temperature ($< 350^\circ$ C) prevents formation of silicon crystal grains on the surface and results in an amorphous structure. In typical amorphous structures, not all the valence band electrons can bond with neighboring atoms, thus creating a high density of dangling bonds. The incorporation of hydrogen in the amorphous silicon film prepared by the PECVD method ensures the passivation of some dangling bonds consequently improving its electrical characteristics. Commonly, the inclusion of 10% hydrogen in the film is considered as an optimum ratio for achieving high quality amorphous silicon films. Exposure to temperatures greater than 300° C facilitates the dissociation of hydrogen, thus degrading the film quality. It is determined that the optimum deposition temperature is at 260° C [23].

Micro-crystalline silicon (μc-Si) is another phase of silicon that can be prepared at low temperatures, by introducing a high concentration of hydrogen. The conductivity of the doped μc-Si is found to be higher than doped amorphous silicon [23], and the former is sometimes used to provide ohmic contact in a-Si:H TFTs.

In this study, all the a-Si:H films were prepared by using the Plasma Therm VII PECVD System. It is a one-chamber system capable of achieving base pressures as low as 10^{-6} $torr$. Different layers, including intrinsic a-Si:H, n^+ a-Si:H, and silicon nitride can be deposited using appropriate selection of gases. Figure 2.1 shows the configuration
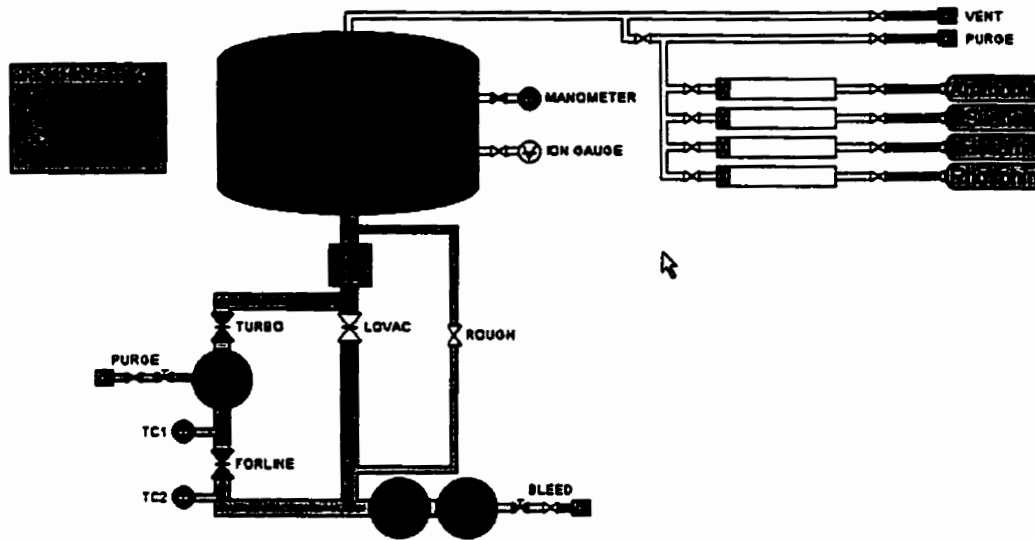
Figure 2.1: Schematic of the Plasma Therm VII system, showing the available gas lines.

of the system and the available gas lines.

Intrinsic a-Si:H layer

The undoped amorphous silicon layer was deposited by the dissociation of pure silane. The deposition conditions are listed in Table 2.1. With the settings given in Table 2.1, a deposition rate of ≈ 119 $\mathring{A}/min$ has been achieved (Fig. 2.2). The grown films show an optical band gap of 1.82 eV (Appendix A). The field effect mobility is 1.1 cm^2/Vs for the thin film transistors fabricated with identical conditions.

The patterning is performed using a mixture of potassium hydroxate and methanol with the following ratios:

KOH 240 gr

CH_3OH 230 ml
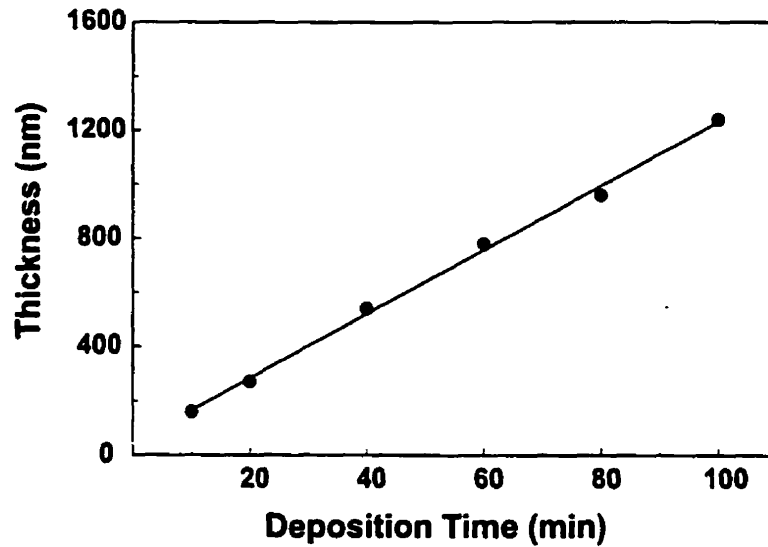
Figure 2.2: Variation of a-Si:H thickness with deposition time.

H_2O $300\ ml$

At $35°$ C this solution yields an etch rate of $\approx 300\pm50\AA/min$. The etching of the a-Si:H films can also be achieved by using tetra methyl ammonium hydroxide (TMAH) with a slower etching rate.

Doped a-Si:H Layer

Often, thin layers of n-doped a-Si:H and μc-Si are employed to provide the ohmic contact between metal and the intrinsic a-Si:H. In this research, a thin layer of n^+ a-Si:H is used to provide the ohmic contact between the back contact and the intrinsic a-Si:H. The choice of n^+ a-Si:H over μc-Si is determined by the need to achieve a clean interface between the n^+ and the intrinsic layer without breaking the vacuum.

The deposition conditions used for the n^+ are reported in Table 2.1 with a gas ratio of 1 : 10^{-2} between SiH_4 and PH_3. For all the n^+ layers fabricated for this study, a

Conditions-Layer	Intrinsic a-Si:H	n^+ a-Si:H	Silicon Nitride
Deposition system	Plasma Therm	Plasma Therm	Plasma Therm
Temperature	$260^\circ\ C$	$260^\circ\ C$	$260^\circ\ C$
Gases	SiH_4	PH_3/SiH_4	$NH_3 \& SiH_4$
Flow (sccm)	50	10	100&10
Pressure(mtorr)	150	250	400
RF Power (W)	10	10	110
Deposition rate ($\AA/min$)	119	50	120

Table 2.1: Deposition conditions for intrinsic a-Si:H, doped a-Si:H, and silicon nitride.

deposition period of 10 min has been used, which yields a layer thickness of $\approx$ 50 nm. Measurements, using test structures incorporated on the wafer, yield a dark conductivity of 280 Ωcm. The ohmic contact between the Cr layer and n^+ layer is confirmed by I-V measurements on the test structures. The patterning of the n^+ layer was also performed using KOH solution. Its etch rate is similar to that of intrinsic a-Si:H.

Silicon Nitride

Silicon nitride serves as a masking material for patterning the a-Si:H and metal layers. The choice of silicon nitride over silicon oxide is determined by the lower defect and trapped charge densities that can be achieved at low deposition temperatures ($< 400^\circ\ C$). These nitride films are deposited by dissociation of a mixture of ammonia and silane (NH_3/SiH_4) in the PECVD system. A nitride-rich film (deposited with the gas ratio of 10 : 1 between NH_3 : SiH_4) is used as it is reported to produce device quality nitride layers [23]. The deposition conditions are listed in Table 2.1. For all the samples prepared for this study, a deposition time of 23 min was used to produce nitride films of thickness $\approx$ 280 nm. This thickness is found to provide the necessary protection

against the KOH. C-V measurements at 100 kHz on test capacitors based on Cr-nitride sandwiches yield a relative dielectric constant of $\approx$ 5.2 for the silicon nitride deposited at 260° C. It is also found that the dielectric constant varies with the deposition temperature. The quality of the nitride layer is critical, since the existence of a large number of pinholes could undermine the integrity of the nitride film, and allow the etchants to attack the underlying a-Si:H and metal layers. A base pressure lower than 8×10^{-6} $torr$, clean gas lines, and a clean chamber ensures reasonably high quality films.

The pattering of the nitride layer is achieved by either a dilute solution of hydrofluoric acid (5% HF and 95% H_2O), for fast etch rate, or buffered hydrofluoric acid (49% HF and 40% NH_4F), for a slower etch rate and hence, better control.

2.1.2 Metal Films

In the proposed detector structure the metal films not only connect the devices to the pads and hence, the outside world, but also provide the conversion mechanism to transfer X-ray photons to energetic electrons. With the latter, the study of the fabrication and interface properties of the metals and a-Si:H is crucial. Since compatibility with the standard TFT process is a main criterion in this research, the metals investigated include Cr, Mo, W, Al. The metal layers were sputtered using the Canadian Vacuum Equipment (CVE) and the EDWARDS sputtering systems. The CVE system has a single chamber with a capability of DC sputtering from one target. The vacuum level in this system can reach 5×10^{-7} $torr$. The EDWARDS system is also a single chamber system, with a capability of holding 3 target materials for either RF or DC sputtering. The base pressure in this system can reach 5×10^{-8} $torr$, which is desirable for achieving high quality interfaces. All the thickness measurements were performed using DEKTAK IIA with a vertical resolution of $200 - 2000$ $\mathring{A}/mm$. The accuracy following the technical data sheet
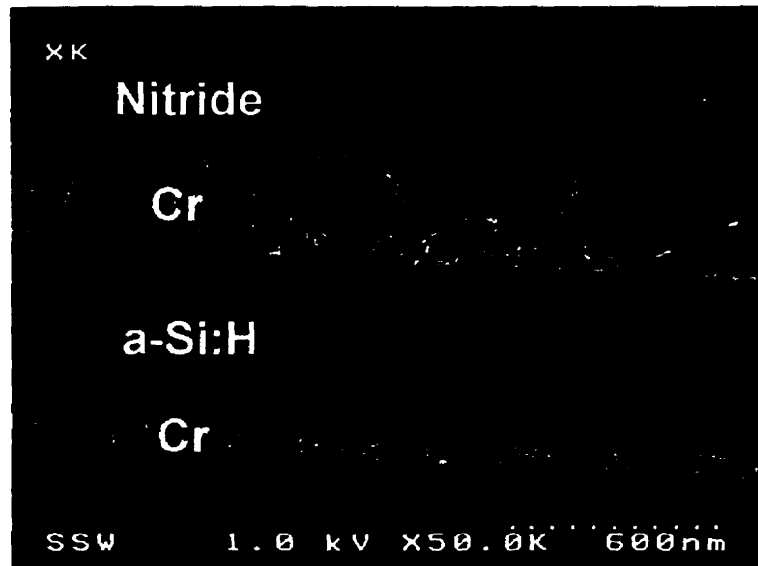
Figure 2.3: Cross sectional view of the interface between Cr and a-Si:H.

is 5%. These thickness values were also confirmed using a bifocal microscope, surface scanning microscope, and scanning electron microscope (SEM).

Chromium

The diode back contact is formed by sputter-deposition of a chromium (Cr) layer using the CVE system. A number of factors make Cr a suitable material for the back contact: good stability in high temperatures, good resistance to the a-Si:H etchant, and ohmic contact formation to the n^+ layer. The Cr can also be used as Schottky contact; the drawback of Cr is its low atomic number ($Z = 24$), which gives a low attenuation coefficient for X-ray photons. Furthermore, the Cr does not form a smooth interface with overlaying nitride passivation layer (Fig. 2.3).

The process conditions used for the deposited films are shown in Table 2.2. Under these conditions, Cr can be deposited with an average rate of $\approx 38 \pm 6 \text{Å}/min$ measured
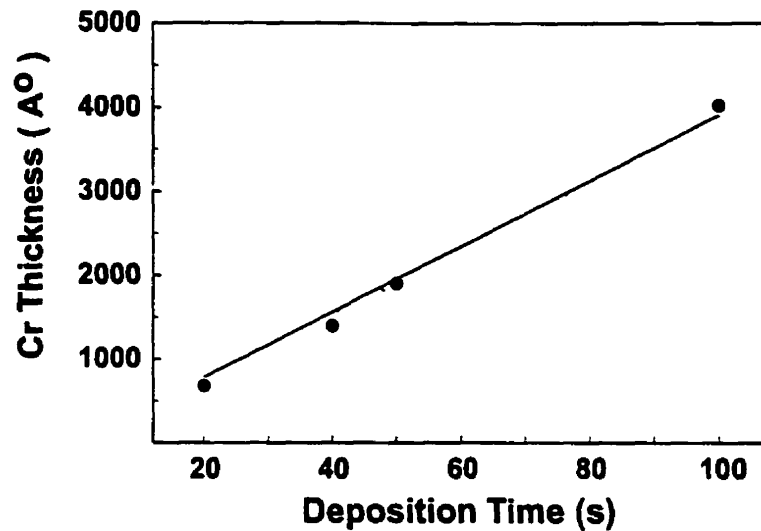
Figure 2.4: Variation of Cr thickness with deposition time.

for four different thicknesses over a sample size of 38 (Fig. 2.4); this is lower than the 50 $\mathring{A}/min$ reported in [23]. The film nonuniformity on different corners of a wafer was $\approx$ 15% over 17 samples, arising mainly from the angle that the wafer holder makes with the horizontal level. The thickness variation among different wafers on a deposition run was $\approx$ 6% over a sample size of 15. The deposited films over different deposition runs show a nonuniformity of $\approx$ 10% over a sample size of 33, since the film thickness strongly depends on the substrate rotation, which is set manually. The film resistivity measured by the four point probe method was $(5.5 \pm 0.8) \times 10^{-4}$ Ωcm. The quality of the film strongly depends on the base pressure of the deposition system, and special care needs to be taken to achieve low pressures, such as heating the chamber before deposition and allowing sufficient time to achieve low pressures.

The Cr layers were patterned using a mixture of ceric ammonium nitride and acetic acid with the following ratio:

$Ce(NH_4)_2(NO_3)_6$ 120 gr
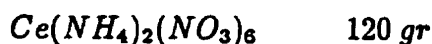
CH_3COOH 100 ml

H_2O 500 ml

This solution gives an etch rate of $20 \pm 4 \overset{\circ}{A}/min$.

Molybdenum

The popularity of molybdenum (Mo) in a-Si:H technology stems from good thermal stability and relatively higher electrical conductivity compared to chromium (a significant issue for pixel addressing). Sputter-deposition of Mo on intrinsic a-Si:H produces smooth interfaces (Fig. 2.5). Moreover, thick layers of Mo ($< 1.1\ \mu m$) can be deposited on a-Si:H without any limitations due to internal stress, which might otherwise cause the films to peel off. Molybdenum also has a higher atomic number ($Z = 42$) which makes it more suitable for photoelectric absorption of X-rays. The only drawback for Mo is that KOH attacks Mo layer as well as the a-Si:H. Thus, it is essential to mask the Mo layer when in a KOH solution.

The deposition of the Mo layers was performed using the EDWARDS sputtering system; the deposition conditions are presented in Table 2.2. Under these conditions, a deposition rate of $125.4 \pm 5.6\ \overset{\circ}{A}/min$ has been achieved (Fig. 2.7).

The measurement of Mo thickness were performed on test glass wafers accompanying the samples during the deposition. With these wafers, the local uniformity of the deposited films measured over an area of $125 \times 125\ \mu m$, using the surface scanning microscope, was better than 99.25% over a sample size of 6 (Fig. 2.6). The thickness variations on different corners of a test wafer measured by DEKTAK II were less than 5.4% over a sample size of 13. The measured variations in thickness of the layers deposited on different runs, with identical deposition conditions and time, was below the accuracy of the DEKTAK II system over a sample size of 5.
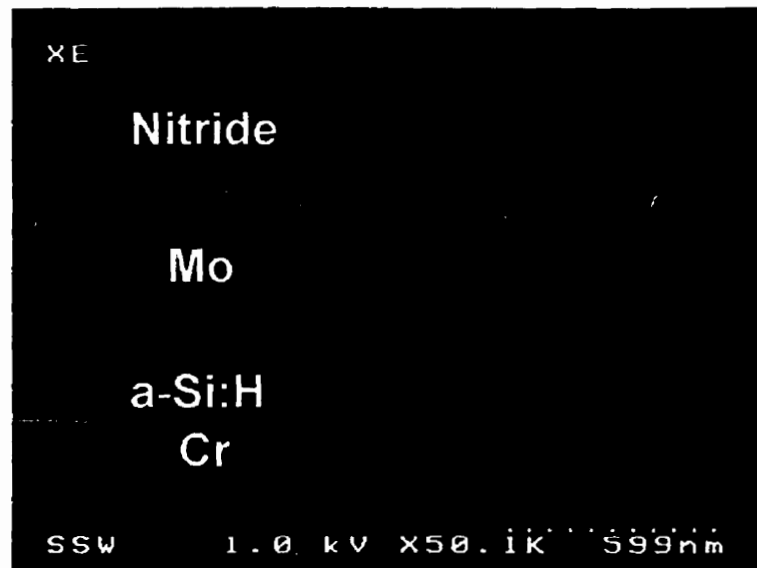
Figure 2.5: SEM of the interface between Mo and a-Si:H.

The patterning of the Mo layers was achieved using a mixture of

H_3PO_4 456 ml

CH_3COOH 36 ml

HNO_3 18 ml

H_2O 90 ml

At room temperature, this solution results an average etch rate of 30.1 ± 3.5 $\mathring{A}/min$. The measured resistivity of the films yields an average of $(1.8 \pm 0.32) \times 10^{-5}$ Ωcm measured over a sample size of 10.

Tungsten

Deposition of tungsten (W) on a-Si:H also creates a Schottky barrier, with interface properties similar to that of Mo (Fig 2.8). However, the internal stress caused by depositing
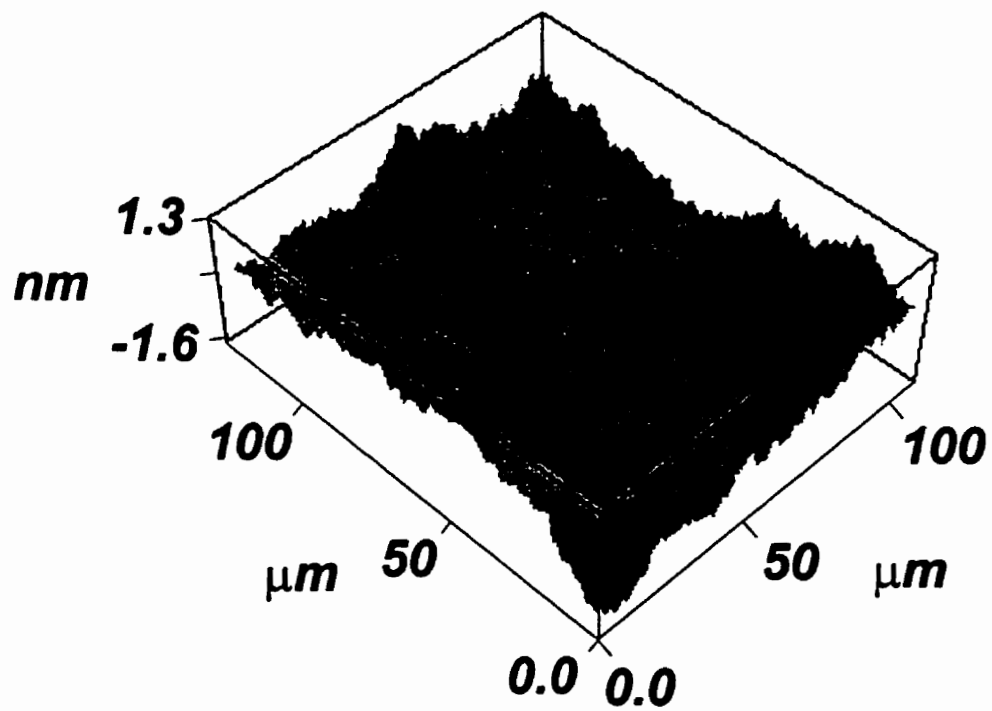
Figure 2.6: Surface smoothness of the deposited Mo film, measured using a surface scanning microscope.
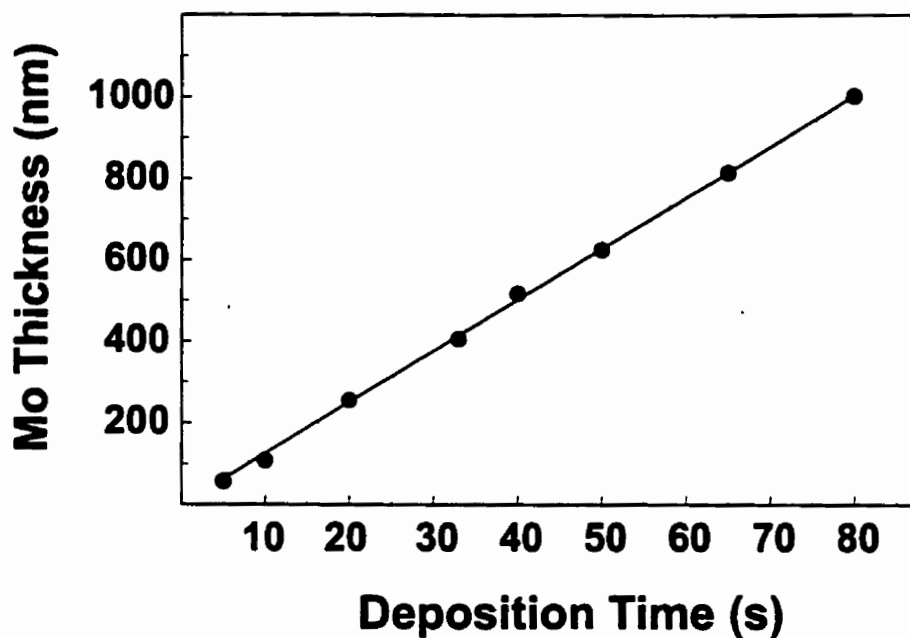
Figure 2.7: Variation of Mo thickness with deposition time.

thick layers of W (< 0.4 μm) causes films to peel off. Therefore, despite the larger atomic number ($Z = 74$) which gives a high attenuation coefficient, tungsten is not used as the Schottky metal.

The deposition conditions for W are similar to Mo (see Table 2.2), using the ED-WARDS system. Based on these settings, an approximate deposition rate of 68 ± 6 $\mathring{A}/min$ has been achieved. The W films were patterned at room temperature using a mixture of [24, 25],

KH_2PO_4	34 gr
KOH	13.4 gr
$K_3Fe(CN)_6$	33 gr
H_2O	1 l

The four point probe resistivity measurements of the films show a conductivity of
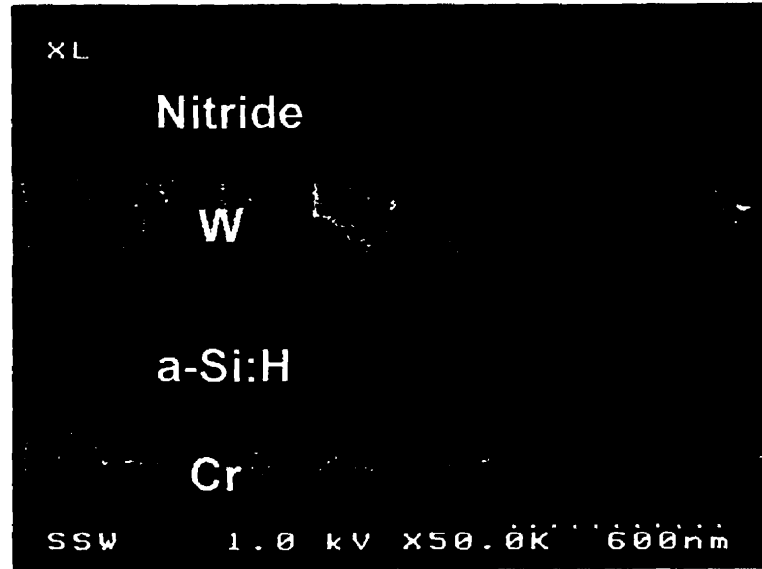
Figure 2.8: SEM cross section of W/a-Si:H interface.

$(7.5 \pm 1.2) \times 10^{-5} \ \Omega cm.$

Aluminum

The high conductivity of aluminum (Al) makes this material desirable for large area arrays. However, due to poor thermal stability, the material is limited to top level interconnects. On contact with intrinsic a-Si:H, aluminum not only gives a Schottky barrier, but also causes crystallization at the interface (Fig. 2.9). The exact mechanisms resulting in this behavior have not been completely understood, hitherto. The low atomic number of aluminum ($Z = 13$) also gives a small X-ray absorption; therefore, this material is not suitable for the Schottky metal. Moreover, further applications of this metal for integrated Schottky diodes and TFTs requires special care and use of barrier metals.

The deposition parameters for Al are shown in Table 2.2. These settings yield a deposition rate of 174 $\text{Å}/min$. The patterning of the Al layers was achieved using a
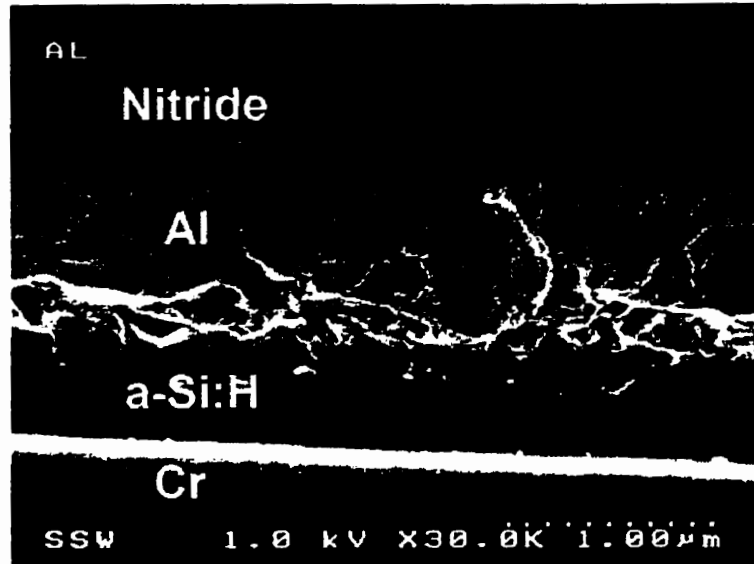
Figure 2.9: SEM cross section of Al/a-Si:H interface.

mixture of, a solution similar to that of Mo was used,

H_3PO_4	456 ml
CH_3COOH	36 ml
HNO_3	18 ml
H_2O	90 ml

The resistivity of the deposited films was measured at $(3.1 \pm 0.1) \times 10^{-6}\Omega cm$ by the four point probe method.

2.2 Fabrication Process

The Schottky diodes were fabricated by vertically stacking different layers on a Corning 7052 glass substrate. The flow of the process is shown in Fig. 2.10. The process starts

Process conditions-Material	Cr	Mo	W	Al
Sputtering System	CVE	EDWARDS	EDWARDS	EDWARDS
DC Power (W)	400	-	-	400
RF Power (W)	-	400	400	-
Temperature ($^\circ C$)	Room	Room	Room	Room
Gas	Ar	Ar	Ar	Ar
Gas Flow (sccm)	$30 - 40$	75	75	75
Base Pressure (mTorr)	5×10^{-7}	5×10^{-8}	5×10^{-8}	5×10^{-8}
Process Pressure (mTorr)	2×10^{-2}	8×10^{-3}	8×10^{-8}	8×10^{-8}
Rotation (rpm)	10	cont.	cont.	cont.
Deposition rate ($\overset{\circ}{A}/min$)	≈ 38	≈ 125	≈ 68	≈ 174

Table 2.2: Deposition conditions for various metal films.

with RCA cleaning of glass wafers (Appendix B), followed by sputter deposition and patterning of Cr to form the back contact (mask #1). Subsequently, the samples are loaded into the Plasma Therm system for deposition of n^+ and intrinsic a-Si:H layers. After this deposition step, samples are quickly removed from the Plasma Therm system and are loaded into EDWARDS sputtering system for deposition of top metal (Schottky metal). In all the samples prepared for this study, the period between introducing nitrogen to Plasma Therm chamber and establishing a vacuum ($< 10^{-1}$ torr) in the EDWARDS chamber was less than 5 *min*. Following this deposition step, the top metal films were patterned (mask #2), and the samples were loaded into Plasma Therm again for silicon nitride deposition. Subsequently, the protective silicon nitride layer was patterned to define the devices (mask #3) and to protect the top metal against KOH. Following this, the Schottky diodes were isolated by removing intrinsic and doped a-Si:H layers. To avoid side wall conduction paths, the area of a-Si:H layers was designed to be larger than

the top metal by ($\approx 2\mu m$). Finally, etching silicon nitride from the pad areas defines the last step of the process (mask #4). Figure 2.11 shows a photograph of a die and electron micrograph of a fabricated Schottky diode. The integrity of the protective silicon nitride is essential for the fabrication yield. As shown in Fig 2.12, a large density of pin-holes could undermine the integrity of the various layers on the wafer.

2.3 Electrical Characteristics

Due to its desirable material properties, Mo has been selected as the suitable metal for X-ray detection. Therefore we have focused on characterizing Mo/a-Si:H Schottky diodes.

The barrier height for Mo/a-Si:H Schottky diodes was measured to be 0.77 eV, by measuring I-V characteristics over a temperature range of $250-300$ K, and by generating an Arrhenius plot, i.e., activation energy against inverse of the temperature.

Typical I-V characteristics of Mo/a-Si:H Schottky diodes of different areas are shown in Fig. 2.13. A DC parametric test system, comprising Keithley 236 Source Measure Units (SMUs), was used for the characterization of the Schottky diodes. The current measurement resolution of the SMUs was 100 fA. Test sequencing and data acquisition were accomplished using a Keithley 2361 Trigger Controller and a dedicated PC. These diodes present an on/off ratio of $\approx 10^6$ at ± 1 V. The reverse current density is lower than 10^{-8} A/cm^{-2} at -1 V. A typical C-V measurement is shown in Fig. 2.14, These measurements were taken using the Keithley 590 CV analyzer, Keithley 595 quasistatic CV meter, and Keithley 230 programmable voltage source with a resolution of 0.1 pF. Often the C^{-2}-V graph is used to extract information about the density of ionized centers in crystalline silicon, using,

$$\frac{1}{C^2} = \frac{2V}{q\epsilon_{ri}\epsilon_o N_D A^2},$$

(2.1)
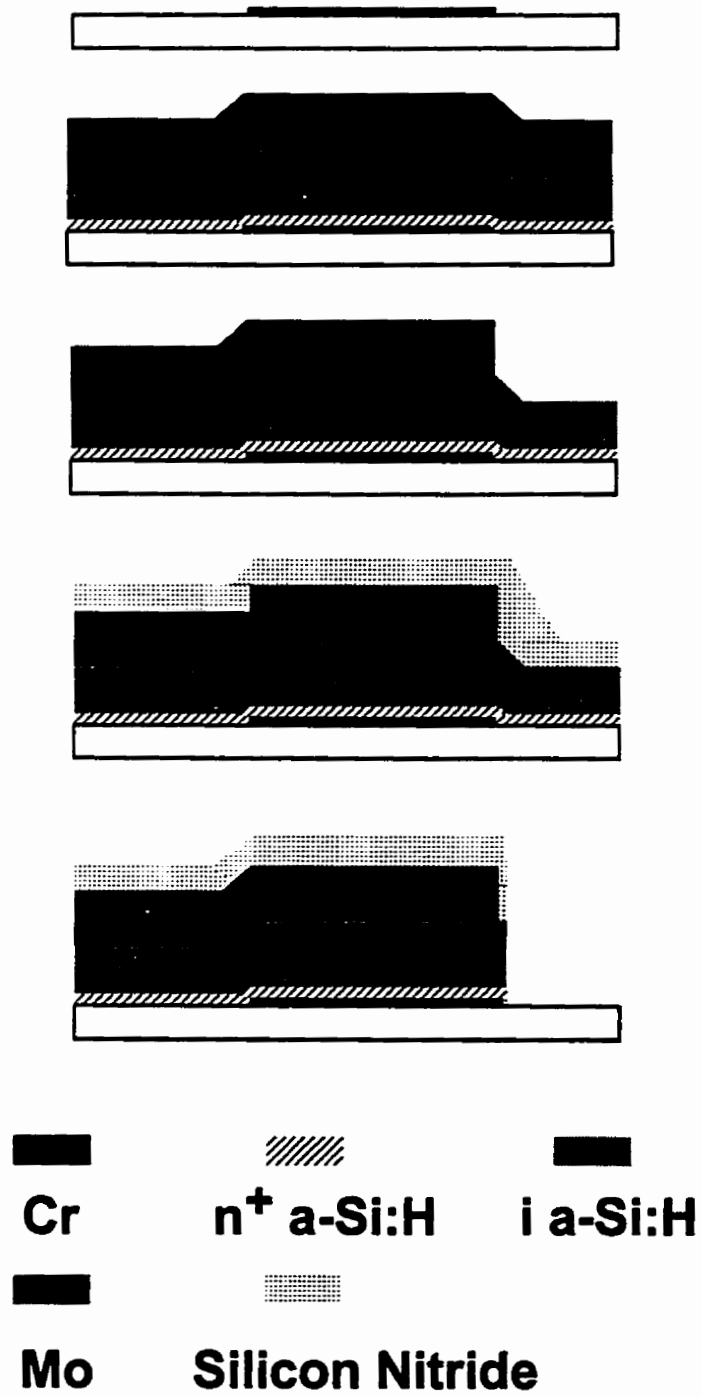
Figure 2.10: Fabrication sequence for Mo/a-Si:H Schottky diodes.
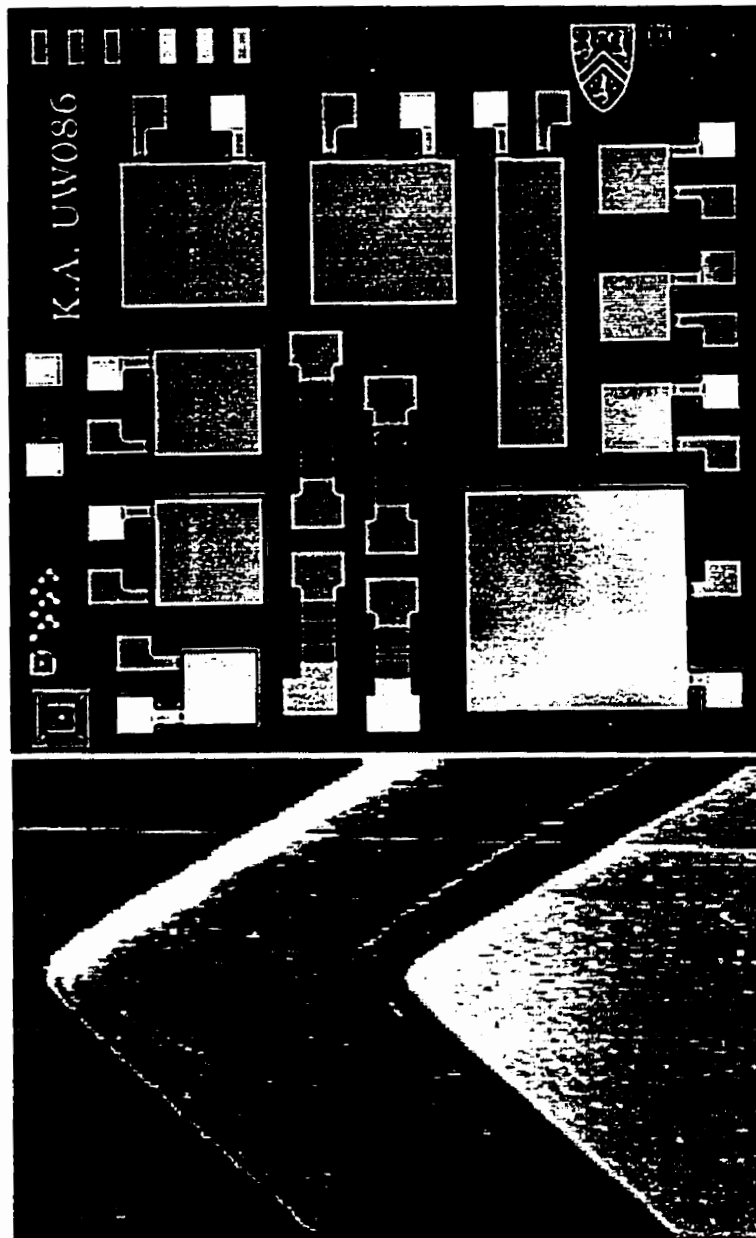
Figure 2.11: Photograph of fabricated die (top) showing detectors with various area; test structures are in the middle of the die; corresponding SEM (bottom) of Schottky diode.

Figure 2.12: Integrity of the masking nitride layer in KOH etching.
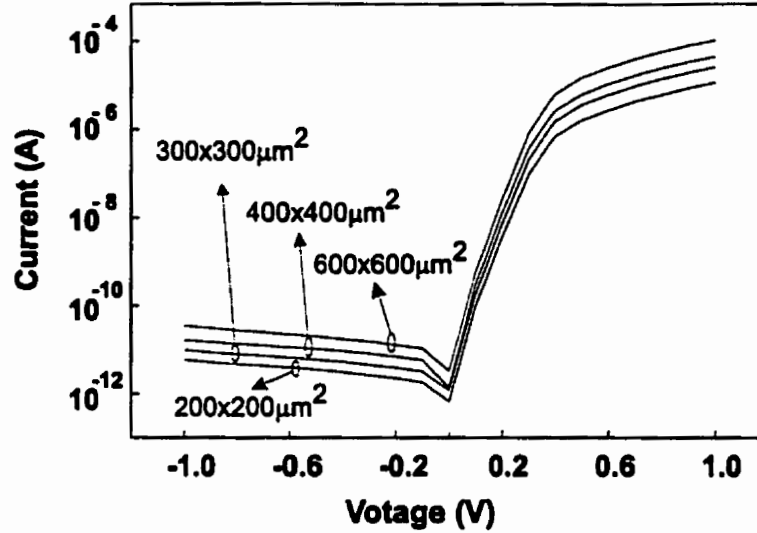
Figure 2.13: Typical I-V characteristic of fabricated Mo/a-Si:H Schottky diodes with various geometries.

where N_D is the density of ionized centers, A is the area, ϵ_{si} is the dielectric constant of a-Si:H ($\approx$ 11.9), ϵ_o is the dielectric constant of vacuum, q is the electron charge (1.6×10^{-19}), and V is the total voltage. However, for a-Si:H due to low mobility of free carriers, C^{-2} does not vary linearly with voltage (Fig. 2.15). Therefore, fitting using (2.1) can not give correct values for the density of ionized centers.
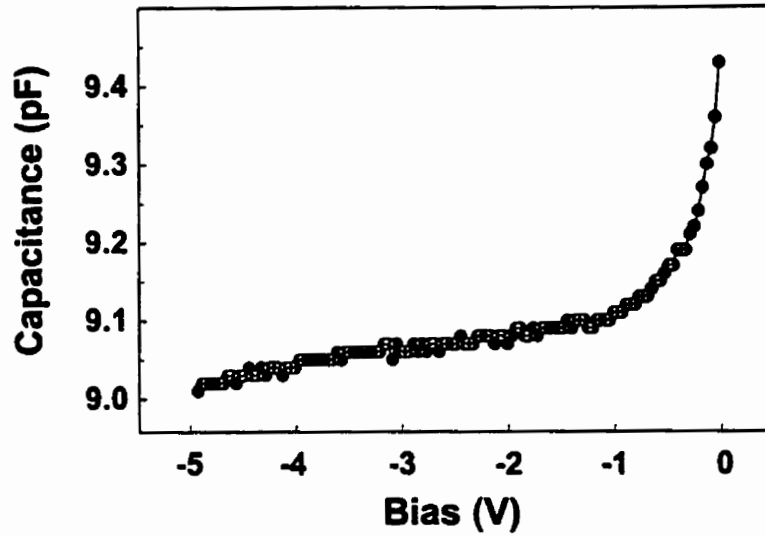
Figure 2.14: Typical C-V characteristic of a $(200 \ \mu m)^2$ Mo/a-Si:H Schottky diode.
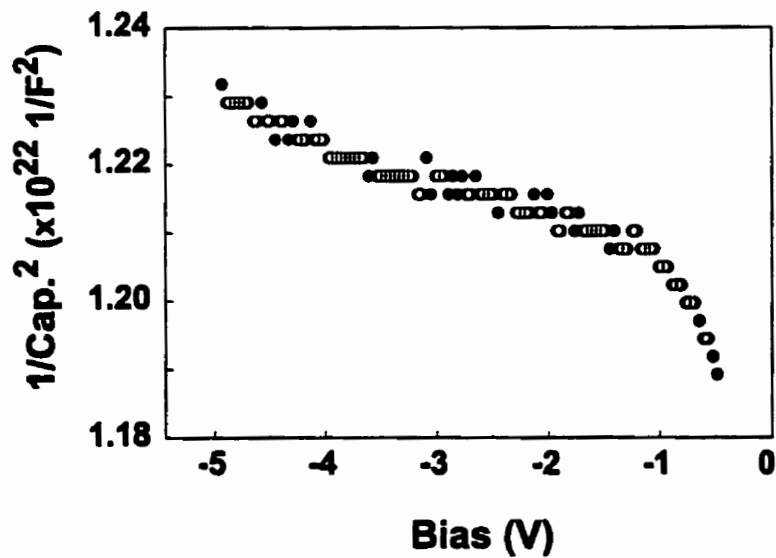
Figure 2.15: Typical C^{-2}-V characteristic of a $(200 \ \mu m)^2$ Mo/a-Si:H Schottky diode.

Chapter 3

Stability

An issue critical to applications of a-Si:H devices is the metastability intrinsic to the amorphous silicon. This metastability yields an electrical characteristic that varies with time. For Schottky diodes, the metastability manifests itself in terms of a time-dependence of the diode reverse current, which ultimately limits the sensitivity of the detector since detection is accomplished by comparing the reverse currents in the presence and absence of X-rays. Therefore, an investigation of the time-dependent reverse current, including identification and reduction of possible sources is essential for detector operation.

In Section 3.1, the sources of metastability intrinsic to a-Si:H are investigated. Subsequently, in Section 3.2, the mechanisms causing the reverse current are studied. The experimental method is explained in Section 3.3, and a discussion of results in Section 3.4.

3.1 Mid-gap States

Many of the unique properties of the a-Si:H arise from its large density of states in the band gap, e.g., metastability, low mobility, and large optical absorption. These states are mainly due to the random structure of the a-Si:H, where a large number of silicon atoms can not fulfill their valence states by bonding to four other silicon atoms, thereby forming dangling bonds. This not only causes a large defect density in the middle of the band gap, but also broadens the conduction and valence bands into the gap, thus forming extended states, tail states, and deep states (i.e., smearing of band edges into the gap). The density and distribution of these states in the band gap determine various electrical and optical properties of the amorphous silicon, including electrical conduction, mobility, and optical absorption. Often the distributions of the band tail (g_t) and deep states (g_d) are represented by exponential functions as (Fig. 3.1) [26, 27, 28],

$$g_t(E) = g_{to} \exp\left(\frac{-E}{k\theta_c}\right) \qquad (3.1)$$

and

$$g_d(E) = g_{do} \exp\left(\frac{-E}{k\theta_d}\right), \qquad (3.2)$$

where g_{to} is the density of tail states on the bottom of the conduction band ($\approx 10^{21} cm^{-3} eV^{-1}$), g_{do} is the density of the defect states at the bottom of conduction band ($\approx 9.6 \times 10^{18} cm^{-3} eV^{-1}$), E is the energy from the bottom of the conduction band, θ is the absolute temperature, k is the Boltzman's constant, θ_c is the characteristic temperature of the tail states ranging between $250 - 300$ K, and θ_d is the characteristic temperature of the deep states (≈ 1000 K) [22][26]. Similar distributions exist for the tail of the valence band, with $\theta_v \approx 400 - 450$ K.

Due to the large number of scattering events, the electrons trapped in the band tail and deep states are localized, and their transport is restricted to tunneling to other mid-gap states or to thermal excitation to the conduction band.
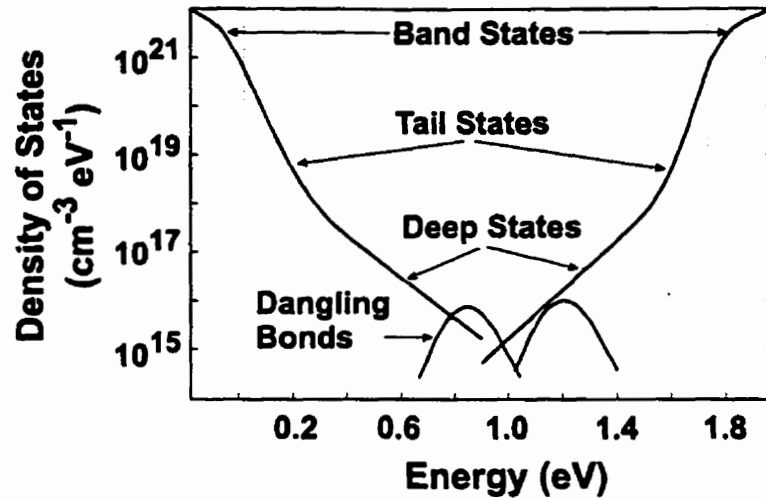
Figure 3.1: Density of states distribution in the band gap of a-Si:H.

3.2 Time Dependent Reverse Current

The reverse current in the a-Si:H Schottky diodes can originate from a number of sources, including the release of trapped charges, thermal generation, thermionic emission, and tunneling [29, 30, 22, 31, 32]. These components can be affected in a number of ways by the instabilities intrinsic to the a-Si, causing the temporal variations of the reverse current. The prevailing mechanisms are primarily determined by the magnitude of the reverse bias. Therefore, our study of the time dependent variation in reverse current is classified into its behavior at low biases and at medium biases.

3.2.1 Low Biases

At low biases ($\leq$ 3 V), it is believed that the reverse current mainly consists of trap discharge, thermal generation, and thermionic emission current [33, 34]. In this range of voltages, tunneling is assumed negligible due to the small electric field at the interface.

The trap discharge component is caused by the release of trapped charge from mid-

gap states and is the dominant component. In equilibrium, mid-gap states located below the Fermi level are occupied by the trapped electrons. The population of these states are in a thermal balance with the number of electrons in the the conduction band (n_c) [35], as

$$\frac{dn_c}{dt} = -R_i n_c + \sum_i r_i n_{it},$$

$$\frac{dn_{it}}{dt} = -r_i n_{it} + R_i n_c, \qquad (3.3)$$

where R_i is the trapping rate to the ith trap state, n_i is the population of trapped electrons in the ith trap state, and r_i is the thermal generation rate, which is defined as

$$r = \omega_o \exp\left(\frac{E_i}{k\theta}\right), \qquad (3.4)$$

where E_i is the energy level of ith trap state, which is defined from the edge of the conduction band, and ω_o is the escape frequency ($\propto 10^{12}\ s^{-1}$).

Shortly after applying the reverse bias, the electrons from the conduction band and extended states are swept away by the electric field. Therefore, the balance condition between conduction band and trap states is removed. Here, the thermal release becomes the dominant mechanism, and the elapse of time enables the trapped electrons to gain the necessary energy to escape from the trap states and reach the conduction band. This causes the quasi Fermi level to move downwards in the band gap. In the conduction band, the released electrons drift in the direction of the applied electric field to contribute to the reverse current. However, the electrons experience further scattering events while drifting towards the terminals, where they can lose their energies and be trapped again in the shallower states. The overall transport is achieved by multiple trap-and-release events which causes dispersive transport (Fig. 3.2) [36, 37]. In dispersive transport, the charge packet is broadened while traveling through the material, and the current on the other terminal presents time dependence as in (Fig. 3.3),
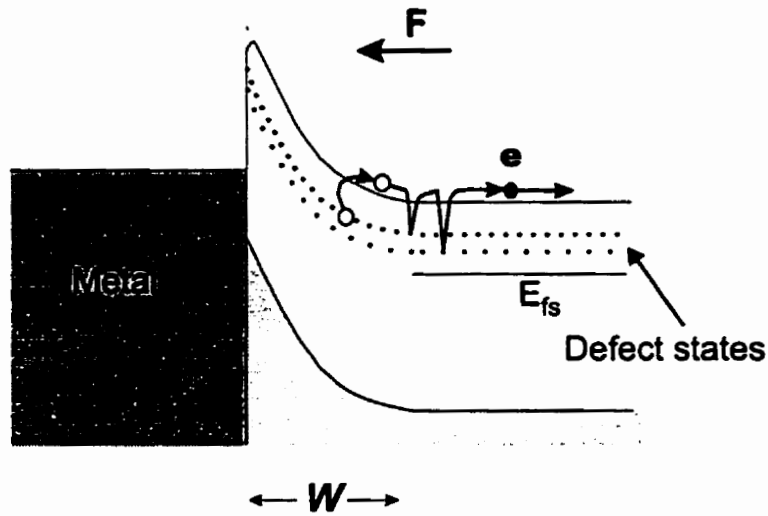
Figure 3.2: Electron transport in a-Si:H layer; F represents the electric field, E_{f_s} shows the Fermi level in a-Si:H, and w is the depletion width.

$$I \propto t^{\alpha-1}, \qquad (3.5)$$

where $\alpha = \theta/\theta_c$. Relation (3.5) is only valid for time scales smaller than the transient time (τ), which can be approximated as,

$$\tau = \frac{d}{\mu_D F}. \qquad (3.6)$$

Here, d is the distance traveled, μ_D is the drift mobility, and F is the electric field. Thus, the overall time dependence resulting from this component consists of the time required for the initial release of the trapped charges, plus the time it takes for the released charge to reach the output terminal.

The dispersive transport also controls the filling of the traps; thus, it affects the flow of the current to the diodes after the bias stress is removed. This can be further quantified by considering that the rate of trap filling is proportional both to the number of traps available to be filled and the number of electrons per second available to do the filling. Following this assumption, the latter quantity is simply the dispersive current observed
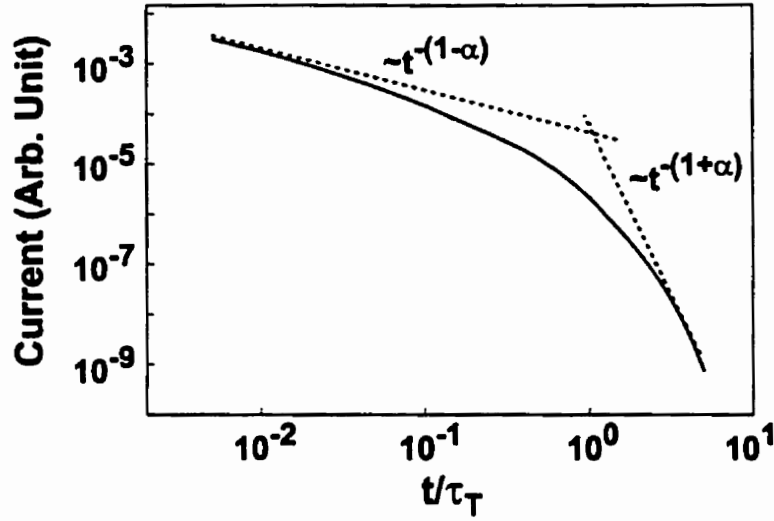
Figure 3.3: Typical transient current caused by dispersive transport.

during trap emptying. The number of available traps is $N_{tot} - N(t)$, where N_{tot} is the total number of traps in the volume between the present and previous positions of the depletion region and $N(t)$ is the number of occupied traps at time, t. Hence, the rate of change of occupied traps is

$$\frac{dN(t)}{dt} = qC_1C_2 \left[N_{tot} - N(t)\right] t^{-(1-\alpha)}, \tag{3.7}$$

where C_1 is the dispersive transport coefficient, q is the electronic charge, and C_2 is a coefficient representing the capture cross section of the process. Solving (3.7) for $N(t)$ gives

$$N(t) = \frac{Q(t)}{q} = N_{tot} \left\{1 - \exp\left[-\frac{qC_1C_2}{\alpha}t^\alpha\right]\right\}, \tag{3.8}$$

where we note that the number of filled traps is related to $Q(t)$ by the electronic charge. The current in the relaxation period, $I(t)$, is related to $dN(t)/dt$, so it displays a more complex time dependence than the simple stretched-exponential.

After the initial discharge of the trap states, the system reaches a steady state that is determined by thermionic emission and thermal generation. In this situation, the contri-

bution of thermal generation to the reverse current can be approximately shown as,

$$J_{th} = qg(E_{qF})k\theta\omega_o \exp\left(-\frac{E_{qf} - E_c}{k\theta}\right) V, \tag{3.9}$$

where E_{qF} is the quasi Fermi level, $g(E_{qf})$ is the density of trap states at the position of quasi Fermi level, and V is the volume of the device. Relation (3.9) is obtained based on the assumption that the mid-gap states located within a distance of $k\theta$ around the quasi Fermi level can contribute to the reverse current. Assuming $g(E_{qf}) = 10^{17}\ cm^{-3}eV^{-1}$, $E_{qF} - E_c = 0.9\ eV$, and $\omega_o = 10^{13}\ s^{-1}$ [22], yields a current of $\approx 4 \times 10^{-14}\ A$ for a $200 \times 200 \times 0.45\ \mu m^3$ diode. The thermal generation rate is not expected to vary significantly with time, hence its contribution to the time dependent reverse current is not considered. The metastability can affect the thermal generation rate only by altering the density of defect states. However, such variations at low biases are not observed experimentally.

Thermionic emission, another mechanism contributing to the reverse current, will be discussed in great detail in the next section. At low biases, however, it is not expected that this component causes any time-dependent variations in the reverse current. This is mainly due to a small electric field at the interface.

3.2.2 Medium Bias

In the medium bias range (3 V to 7 V), we assume that the reverse current mainly stems from thermionic emission and tunneling. In thermionic emission, the transport of an electron to the conduction band is achieved by thermal excitation over the barrier (ϕ_0). Hence, the resulting reverse current strongly depends on both the temperature and height of the encountered barrier. Ideally, the barrier height is related to the difference between the metal work function and the semiconductor affinity, and is a constant. But in fact, the

barrier height encountered by an electron is modified in a number of ways, *viz.*, image force lowering, and trapping of charge on the interface. The modified barrier is often referred to as effective barrier height (ϕ_{eff}).

It is also possible for electrons with energies lower than the barrier height to penetrate through the barrier to the a-Si conduction band, by quantum mechanical tunneling. In general, the tunneling rate depends on the width and the height of the barrier; the barrier width encountered by an electron depends on its thermal energy (Fig. 3.4). Therefore, the resultant current is also temperature dependent, and this mechanism is sometimes referred to as thermionic field emission. The barrier width also depends on the bending of the conduction band, which is related to the electric field inside the depletion region. Furthermore this electric field is controlled by the applied bias and the depletion width.

In a-Si devices, the depletion width can vary with time, even for a constant applied bias (Fig. 3.5). The reason for this behavior can be established by considering the distorted band structure of a-Si, and the existence of defect states inside the band gap. Usually, these defect states result from dangling bonds with the three possible charge states of D^-, D^o, and D^+, where D^+ denotes a dangling bond with no electron, D^o to a singly occupied, and D^- to a doubly occupied dangling bond.

In equilibrium, the defect states located below the Fermi level are occupied by trapped electrons. The applied reverse bias quickly removes the mobile electrons from the conduction band and the extended states, but not the electrons trapped in deep defect states. The trapped electrons mask the depletion charge (mainly resulting from ionized defect sites) and causes the depletion region to be larger than the steady state value. With time, trapped electrons can gain the necessary energy to escape from the trap states, hence allowing the depletion width to decrease. Eventually, the depletion width approaches its steady state value, which is larger than its zero bias value.
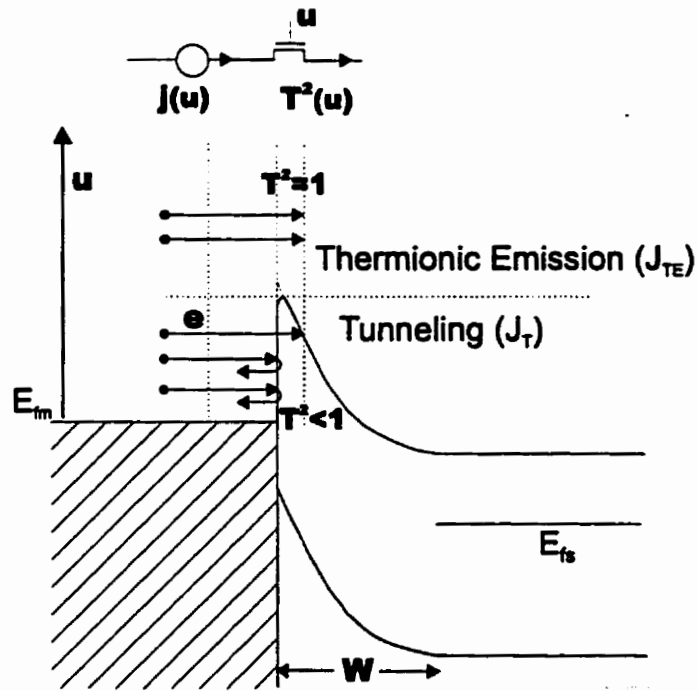
Figure 3.4: Schematic view of the two reverse current mechanisms: thermionic emission and tunneling; w represents the depletion width, u is the electron thermal energy, E_{fs} indicates the Fermi level in a-Si, E_{fm} is the metal Fermi level, and T^2 is the tunneling probability. The reverse current can be symbolically shown as a combination of current source (the flow of electrons towards the barrier) and a pass transistor (the tunneling rate), which is controlled by the thermal energy of the electrons.
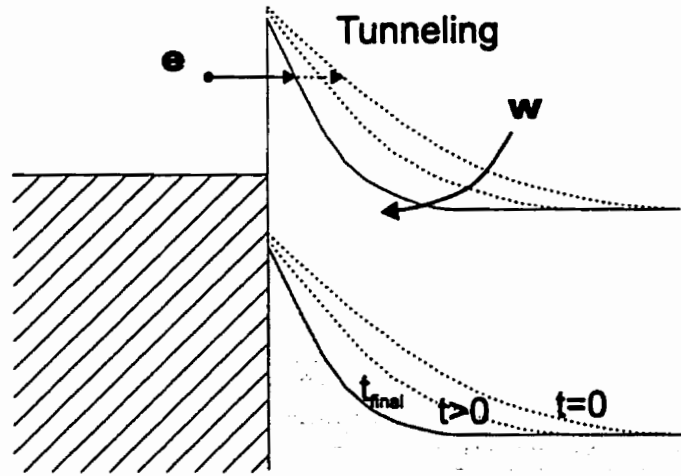
Figure 3.5: Time-dependent variation of depletion width (w) leading to variation in reverse current.

For the time scale of interest in this study, the time-dependent changes of the defect charge follow a stretched exponential form [38] [22]. Thus, similar dependencies are expected for the depletion width and the reverse current. Such a time-dependent behavior can be further quantified by examining the reverse current resulting from the thermionic emission and the tunneling process. For thermionic emission, the current can be obtained from [39]

$$J_{TE} = \int_{E_{fm}+q\phi_{eff}}^{\infty} qv_x dn, \tag{3.10}$$

where v_x defines the velocity of the electron in the x direction and dn defines the number of electrons with that velocity in the x direction. In relation (3.10), it is assumed that all the electrons with energies above the barrier can overcome the barrier and contribute to the current. The number of electrons in a particular energy range of E to $E + dE$ is given by multiplying the density of available states ($N(E)$) by the probability of occupancy ($F(E)$) as

$$
\begin{aligned}
dn &= N(E)F(E)dE \\
&= \frac{4\pi(2m^*)^{3/2}}{h^3}\sqrt{E - E_{fm}}\exp(-\frac{E - E_{fm}}{k\theta})dE,
\end{aligned}
\tag{3.11}
$$

where m^* is the isotropic effective mass of electrons, E_{fm} is the Fermi level of the metal, and h is Planck's constant. The energy of a mobile electron can be approximated by its kinetic energy, so,

$$E - E_f = \frac{1}{2}m^*v^2, \tag{3.12}$$

where $v^2 = v_x^2 + v_y^2 + v_z^2$. From (3.10), (3.11) and (3.12), the thermionic current can be shown to be,

$$J_{TE} = 2q(\frac{m^*}{h})^3 \int v_x \exp(-\frac{m^*v^2}{2k\theta})(4\pi v^2)dv. \tag{3.13}$$

Rewriting (3.13) in Cartesian coordinates and integrating over y and z give,

$$J_{TE} = \frac{2\pi q m^{*2}k\theta}{h^3} \int_{v_{ox}}^{\infty} v_x \exp(-\frac{m^*v^2}{2k\theta})dv_x, \tag{3.14}$$

where $v_{ox} = \sqrt{\frac{2q\phi_{eff}}{m^*}}$, defines the minimum velocity needed to overcome the barrier. Defining the kinetic energy ($u = \frac{1}{2}m^*v_x^2$),

$$J_{TE} = \frac{A^*\theta^2}{k\theta} \int_{q\phi_{eff}}^{\infty} \exp(-\frac{u}{k\theta})du, \tag{3.15}$$

where A^* is Richardson's constant, given by

$$A^* = \frac{4\pi q m^* k^2}{h^3}, \tag{3.16}$$

which is approximately equal to $120A/(cm^2 K^2)$, assuming a free electron mass. For tunneling, the current can be divided into a two step process: the electron current reaching the barrier and the fraction that passes through the barrier. The latter is given by tunneling probability ($\|T\|^2$), so

$$J_T = \int_{E_f}^{E_f+q\phi_{eff}} qv_z\|T(v_X, \phi_{eff}, F)\|^2 dn. \tag{3.17}$$

Commonly, for a slowly varying potential barrier, the tunneling rate is calculated using the Wentzel-Kramers-Brillouin (WKB) approximation, which expresses the transmission

of a particle through a given barrier [40]. For this reason, the metal/a-Si barrier is usually approximated by a triangular potential ($V(x)$) such as [41],

$$V(x) = \phi_{eff} - qFx, \qquad (3.18)$$

where ϕ_{eff} is the effective barrier height, q is the unit charge, F is the electric field in the depletion region of a-Si, and x denotes the distance away from the interface. Here, the maximum height of the barrier (V_{max}) occurs at the interface ($x = 0$), and is equal to the effective barrier height (ϕ_{eff}). Since the triangular approximation can describe the barrier very well only close to the interface, F is usually considered to be constant at the maximum value of the electric field, which occurs at the interface. Using (3.18) for the barrier and assuming a thermal energy equal to u, the transmission probability ($\|T\|^2$) can be shown to be

$$\|T(u)\|^2 \approx \exp\left[-(\frac{8m^*}{\hbar^2})^{1/2} \int dx \sqrt{\phi_{eff} - qFx - u}\right]. \qquad (3.19)$$

The tunneling current can be obtained by multiplying the transmission probability of the electron current reaching the barrier with a given thermal energy and by performing a summation, giving

$$J_T = \frac{A^*\theta^2}{k\theta} \int_0^{q\phi_{eff}} \|T(u)\|^2 \exp(-\frac{u}{k\theta})du, \qquad (3.20)$$

or

$$J_T = \frac{A^*\theta^2}{k\theta} \int_0^{q\phi_{eff}} \exp\left[-\frac{u}{k\theta} - (\frac{8m^*}{\hbar^2})^{1/2} \int dx \sqrt{\phi_{eff} - qFx - u}\right]. \qquad (3.21)$$

Finally the net reverse current is

$$J_{tot} = J_{TE} + J_T. \qquad (3.22)$$

Unfortunately, there is no analytical solution for J_{tot}, and numerical evaluation is the only possibility. Such numerical calculations yield the behavior shown in Fig. 3.6. For
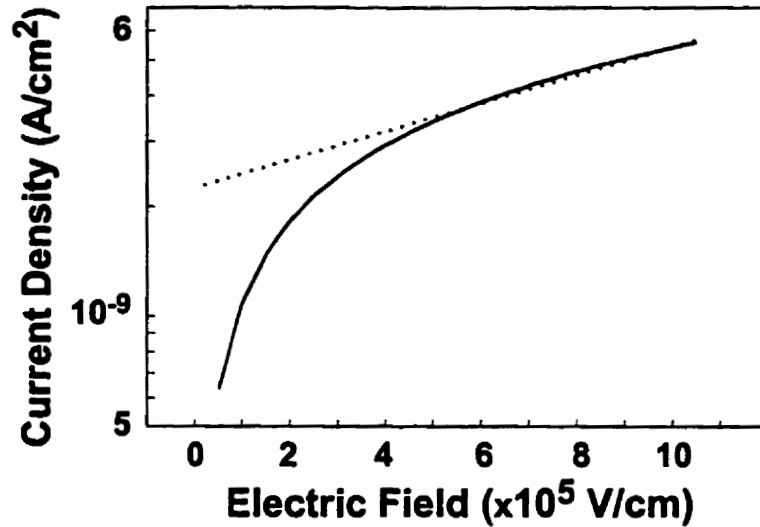
Figure 3.6: Variation of reverse current with electric field.

the moderate biases (electric fields above $2 \times 10^5 V/cm$), the numerical results of the reverse current can be modeled as [42] [43] [41]

$$J_{tot} = A^* T^2 \exp\left[-q\frac{(\phi_o - a\|F\|)}{k\theta}\right], \qquad (3.23)$$

where a is the effective tunneling parameter, which depends on process dependent parameters such as the dielectric constant, the effective mass, the surface charge density, and the potential barrier profile. From relation (3.23), time variations of the reverse current can be related to the time dependence of the electric field. In a-Si:H, due to the metastable changes triggered by the movement of the quasi Fermi level [44], it is difficult to define a distribution of ionized sites. But we can still introduce a net density of ionized states that produces the same electric field at the interface; hence,

$$F_{max} = \sqrt{\frac{qN_D^-(t)V_{tot}}{\epsilon_s}}, \qquad (3.24)$$

where $N_D^-(t)$ is the time-dependent net density of ionized defect states (positive sites, D^+) and V_{tot} is the potential across the depletion layer. The time variations of the ionized

sites follow the expression

$$N_D^-(t) = N_D - N_{trap}(t) = N_D - N_o \exp\left[-\left(\frac{t}{\tau_e}\right)^{\beta_e}\right], \tag{3.25}$$

where N_o is a parameter that defines the change of the defect density from its initial value N_i, N_D is the final density of ionized defect states, τ_e is a time constant, and β_e is a constant that depends on the characteristic temperature of mid-gap states. From (3.24) and (3.25),

$$F_{max} = \sqrt{\frac{qV_{tot}}{\epsilon_s}[N_D - N_o \exp(-(t/\tau)^{\beta_e})]}, \tag{3.26}$$

which can be approximated to (assuming $N_o < N_D$ and ignoring higher order terms in a Maclaurin expansion)

$$\begin{aligned}
F_{max} &= F_o + F(t) \\
&= \sqrt{\frac{qV_{tot}N_D}{\epsilon_s}} - \frac{1}{2}\sqrt{\frac{qV_{tot}N_D}{\epsilon_s}}\frac{N_0}{N_D}\exp\left[-(t/\tau)^{\beta_e}\right].
\end{aligned} \tag{3.27}$$

From (3.23) and (3.27), the time-dependent reverse current becomes

$$J_{tot} = A^*T^2 \exp\left[-q\frac{(\phi_o - a\|F\| - a\|F(t)\|)}{k\theta}\right]. \tag{3.28}$$

In addition to the variations of the electric field, the trapping of holes and metastable changes at the interface can also contribute to the time-dependent reverse current. As a result of the applied bias and the extension of the depletion region, a packet of holes is swept away by the electric field, drifting towards the interface. Part of this packet gets trapped in the mid-gap states that exist at the interface. Trapping of holes can result in $D^- \rightarrow D^o$ or $D^o \rightarrow D^+$ transitions, thereby increasing the tunneling current by means of assisted tunneling (Fig. 3.7). Further, the holes can get trapped in the thin interfacial layer where they reduce the effective barrier height. Under most circumstances (assuming that the occupation of interface states is determined by the metal Fermi level), both of these

mechanisms result in modification of the tunneling parameter a as,

$$a = a_f + a(t), \tag{3.29}$$

where a_f is the time-independent component of a, and $a(t)$ is the time-dependent component. For a simple triangular approximation, we assume

$$a(t) \propto N_{trap-h}, \tag{3.30}$$

where N_{trap-h} is the number of holes that get trapped in mid-gap states. The trapping of holes is directly related to the rate at which they reach the interface (dispersive transport), and the probability of trapping in the mid-gap states [33]. Therefore,

$$\frac{dN_{trap-h}}{dt} = \zeta\eta\left[N_{o-h} - N_{trap-h}\right]t^{-(1+\alpha_h)}, \tag{3.31}$$

where ζ is the capture cross section for holes, and η is the dispersive transport coefficient. From (3.31),

$$N_{trap-h} \propto \left\{1 - \exp\left[-\left(\frac{t}{\tau_h}\right)^{\beta_h}\right]\right\}, \tag{3.32}$$

where τ_h is the time constant for the hole trapping, and β_h depends on the dispersive transport. From (3.29), (3.31), and (3.32),

$$a = a_f - a_r \exp\left[-\left(\frac{t}{\tau_h}\right)^{\beta_h}\right], \tag{3.33}$$

where a_r is the relative change of the tunneling parameter. From (3.28), (3.29), and (3.33),

$$J_{tot} = A^*T^2 \exp\left\{-q\frac{[\phi_o - (a_o + a(t))(\|F\| + \|F(t)\|]}{kT}\right\}. \tag{3.34}$$

This expression will be compared with experimental data in section 3.4.
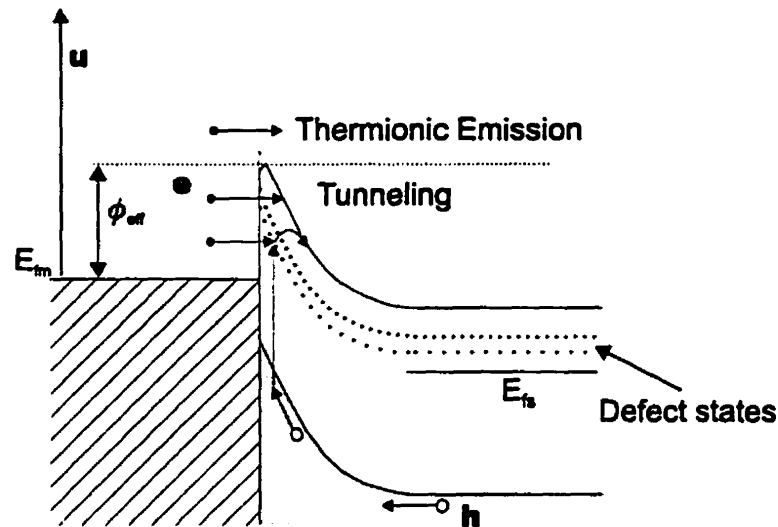
Figure 3.7: Effect of charge trapping on the reverse current mechanisms.

3.3 Measurement Setup

The electrical stressing experiments were performed in a dark, shielded environment using Keithley source measure units (SMU model 236) to provide a constant reverse bias to the sample for prolonged times (up to 3 hours), with a resolution of 10 μV. The current readings were taken at equal intervals of 0.4 s, owing to the integration time of the equipment, and with a resolution of 10 fA. Due to the extra time required for establishing the measurement parameters, the first data point was recorded 0.6 s after the application of the bias. Data acquisition and the control of the experiment were performed by a personal computer.

The measurements were performed by subjecting fresh devices to consecutive cycles of voltage stress, 300s of zero-bias relaxation, and thermal annealing (Fig. 3.8). Thermal annealing at 150°C for two hours ensured the removal of metastable defects. Care was taken to ensure that the voltages during the stress periods were in ascending order to

Fresh Sample

Electrical Stress
up to 3h

Relaxation
300 s

Thermal Annealing
2h @ 150° C
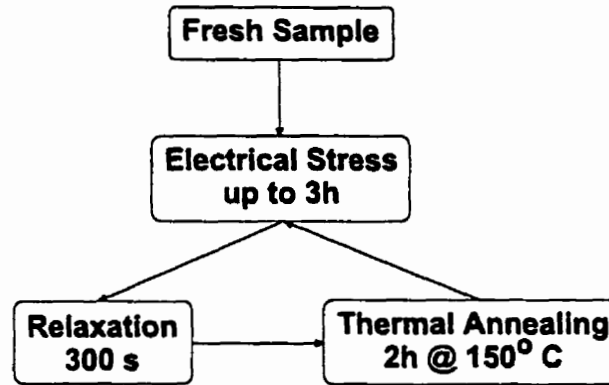
Figure 3.8: Measurement sequence for studying the time-dependent reverse current variation.

ensure the results were measured for undamaged devices.

3.4 Experimental Results

Typical time-dependent reverse current for different bias voltages is shown in Fig. 3.9. Here a sample was voltage-stressed, allowed to relax at zero volts, and then thermally annealed prior to the next voltage stress cycle. Reproducibility of the time-dependent characteristics was examined for more than 20 samples. In the low bias regime ($V <$ 3 V), the current initially decays with a power law dependence, and then levels off at a lower value which depends on the bias. In contrast, at medium biases ($3 V < V < 7 V$), the current initially follows a similar variation to that at low biases, but subsequently increases by several orders of magnitude and levels off at the higher value.

3.4.1 Low Bias Behavior

The time-dependent behavior illustrated in Fig. 3.9 is also observed with Schottky structures of other metals, e.g., W. This suggests that interface conditions are less likely to
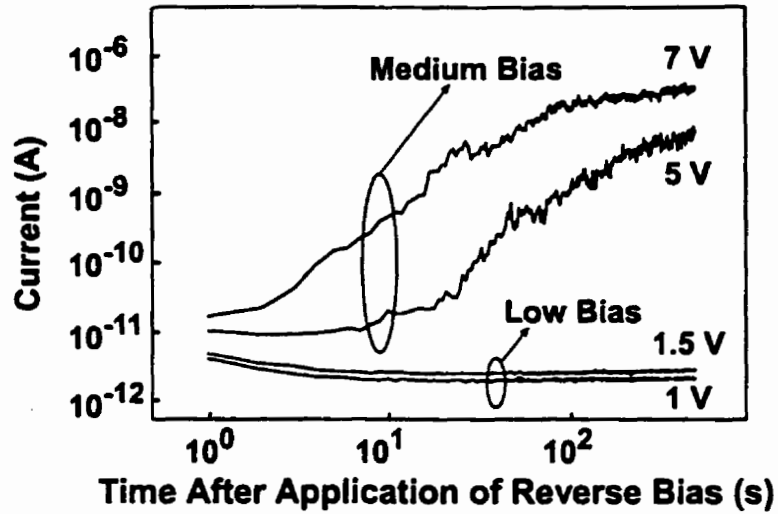
Figure 3.9: Typical variation of reverse current against time for different bias values.

be important at low biases. Furthermore, the bias stress curves are reproducible regardless of the inclusion of the thermal annealing step. This observation suggests that the behavior at low biases is not due to a metastable change in the material, but most likely originates from a reversible effect. Figure 3.10 shows a low bias behavior for a single device operated at several values of V_{rev}, and the inset presents the log-log plot of the current decrease over the first 10 s. This reveals that variation of the reverse current is as,

$$I \propto t^{-\gamma}, \tag{3.35}$$

with $\gamma = 0.44$ at a reverse bias of 1.5 V. Considering the average initial release time of 10 ms, as predicted for a Fermi level initially located at 0.6 eV below the conduction band, the release time of carriers is insignificant in the time scale of this experiment. Also considering the transit time (10 μs), this behavior can be associated only with the tail of a dispersive decay.

The results for a typical relaxation behavior at zero bias is shown in Fig. 3.11 for a device which has been stressed previously for 1 h at $V_{rev} = 1$ V. It is clear that the
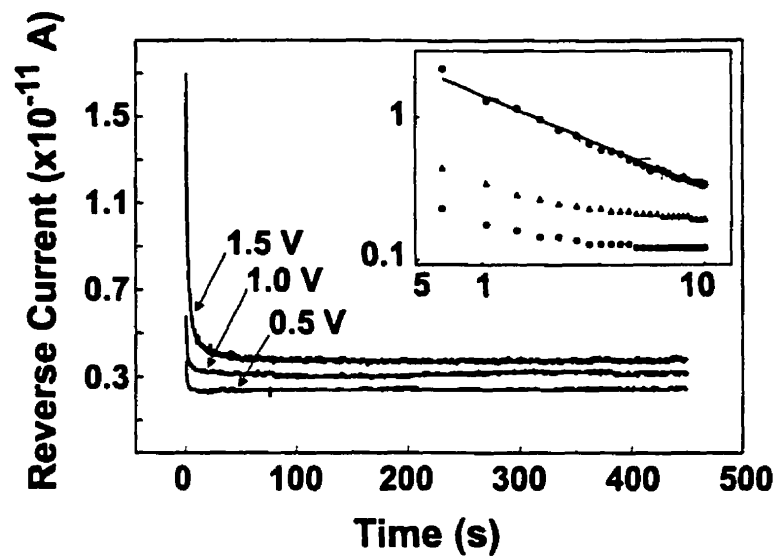
Figure 3.10: Variation of reverse current with time for a Schottky diode at the indicated reverse biases. The inset shows a log-log plot of the initial current variation for the same biases.

characteristics are not linear on this log-log scale, indicating that the recovery current does not follow the power law observed during the stressing period. Also shown in Fig. 3.11 is the same data plotted in terms of the cumulative charge transferred, $Q(t)$, calculated from the summation of the products of the current and the appropriate time intervals. The fitted curve shown in Fig. 3.11 is a stretched exponential of the form

$$Q(t) \approx Q_{tot} \left[1 - \exp\left(-\frac{t}{\tau}\right)^{\beta} \right], \tag{3.36}$$

with, in this case, $\tau = 10\ s, \beta = 0.9$, and $Q_{tot} = 3.9 \times 10^{-11}\ C$. This figure for the charge ejected during the stressing period is approximately equal to that recovered during the relaxation period, as would be expected.

It should be noted that the above value of Q_{tot} does not include the charge transferred before $t = 0.6\ s$, the first data point. Although the current is higher at smaller values of t, the area under the curve is dominated by the behavior at large t. Assuming that the
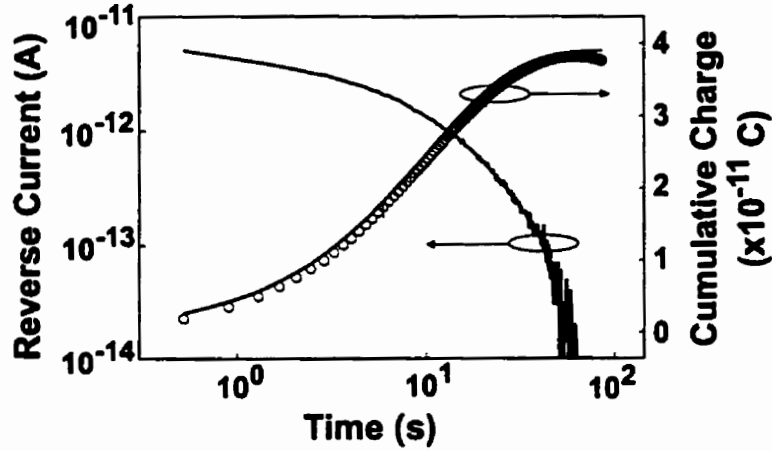
Figure 3.11: Time dependence of the zero-bias relaxation current and the cumulative charge transported. The solid line indicates a stretched-exponential fit to the data points.

spatial density of traps is constant, Q_{tot} should therefore be proportional to $\sqrt{V_b + V_{rev}}$ from the depletion approximation [39], where V_b is the built in potential of the Schottky diode. This relationship has been confirmed from the exponential data for both stress and relaxation periods.

From these results, the total number of traps between the initial and final positions of the depletion layer ($t \to \infty$) can be estimated at $N_{tot} = Q(\infty)/q = 2.4 \times 10^8$ traps.

3.4.2 Medium Bias Behavior

A typical time-dependent reverse current characteristic at $-5\ V$ bias is depicted in Fig. 3.12. Shortly after applying the reverse bias, the current shows an small decay, which is related to removal of electrons from the conduction band and the release from shallow tail states and further transport through the neutral region in a-Si [33]. Once the shallow states are evacuated, the current levels off at a low value for a short period. After this short period, the current rapidly increases, which is attributed to discharging of the negatively
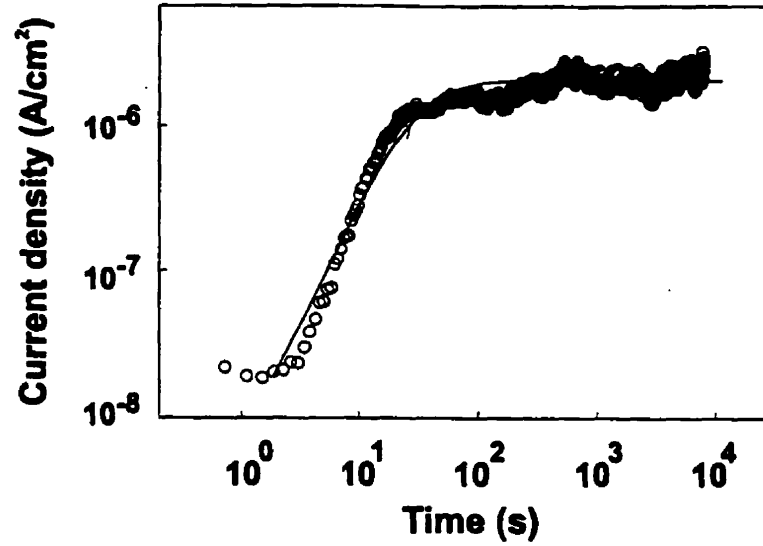
Figure 3.12: Time-dependent reverse current at -5 V bias. The solid line corresponds to fit resulted from relation (3.34), using $\beta_e = 0.7$, $\tau_e = 3$, $\beta_h = 0.6$, and $\tau_h = 8$.

charged defects at the interface. The further increase in the reverse current results from the collapse of the depletion region and the associated increase of the electric field. The reverse current eventually stabilizes at a certain value.

In order to describe the time-dependent current variations, we focus our analysis to the period in which the conduction band and extended states are depleted from electrons. The resulting variations using relation (3.34) are depicted in Fig. 3.12 as solid line. This fit yields the numerical values listed in Table 3.1. These values are consistent with the numerical values that have been extracted for these devices experimentally or with those found in the literature. Most of these parameters are closely related to the detailed fabrication process and must be characterized for each process. In particular, the values for barrier height (ϕ_o), tunneling parameter (a), and final defect density (N_D) are among the most important parameters affecting the reverse current. The measurement errors in Richardson's constant have less effect on the final error, due to the slow variations

of the logarithmic function. Moreover the magnitude of the reverse current variation is less sensitive to β_e, β_h, τ_e and τ_h; these parameters mostly determine the form of the variation. A summary of the methods used to extract these parameters is also provided in Table 3.1.

For the present devices, the rather large density of final defect states compare to the other published values maybe related to possible presence of a slight phosphine residual in the intrinsic a-Si films, since these samples were prepared using a single chamber deposition system. The tunneling parameter (a) reflects the interface quality and, for high quality metal/a-Si:H interface, values as low as 10 $\mathring{A}$ are reported [42]. The possible existence of residual oxygen and water in the deposition system may explain the presently high value for the tunneling parameter. This may also explain the low values for Richardson's constant and electron effective mass, which are consistent with the large inferred value of tunneling parameter and high density of defect states at the interface.

3.4.3 High Bias Behavior

Figure 3.13 illustrates the time-dependent reverse current for high biases. In contrast to both the low- and medium-bias cases, the initial state of devices cannot be restored either by providing sufficient relaxation time in a dark environment or by thermal annealing. In this case, the effects of bias are irreversible. After an extended stress period, the current decreases and the diode no longer exhibits rectifying characteristics. Post-bias-stress C-V (Fig. 3.14) and C-t measurements suggest the lack of a depletion region, which could be attributed to structural changes in the device.

Parameter/Units	Published range	Present values	Extraction Methods/ References
m^*/m_o	$0.05 - 0.7$	0.007	[22][42][29]
ϕ_o (eV)		0.77	$I - V$ in different T [39][22] or internal photoemission
a $(\times 10^{-7}\ cm)$	$1 - 10$	4	$I - V$ [22][42]
a_r $(\times 10^{-7}\ cm)$		3.5	
N_D $(\times 10^{17}\ cm^{-3})$	$1 - 5$	1.5	$I - t$ at fixed V after stabilization, [45][31][32]
N_i $(\times 10^{16}\ cm^{-3})$	$0.3 - 1$	1	$C - V$ and $1/C^2$[22][31][32]
N_o/N_D	$0.95 - 1$	0.95	Comparison between N_D and N_i
ϵ_{a-Si}	11.9	11.9	[42] [22][32]
β_e	$0.45 - 0.7$	0.7	[22]
τ_e (s)		3	
β_h	$0.5 - 0.7$	0.6	[22]
τ_h (s)		8	

Table 3.1: Numerical values employed for calculating time-dependent variations of the reverse current in Mo/a-Si:H Schottky diode at medium biases.
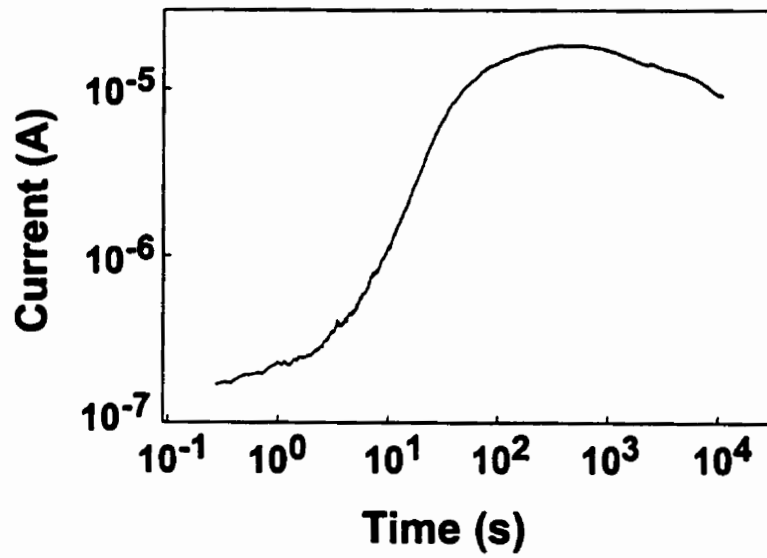
Figure 3.13: Time dependent reverse current for prolonged stressing under 10 V.
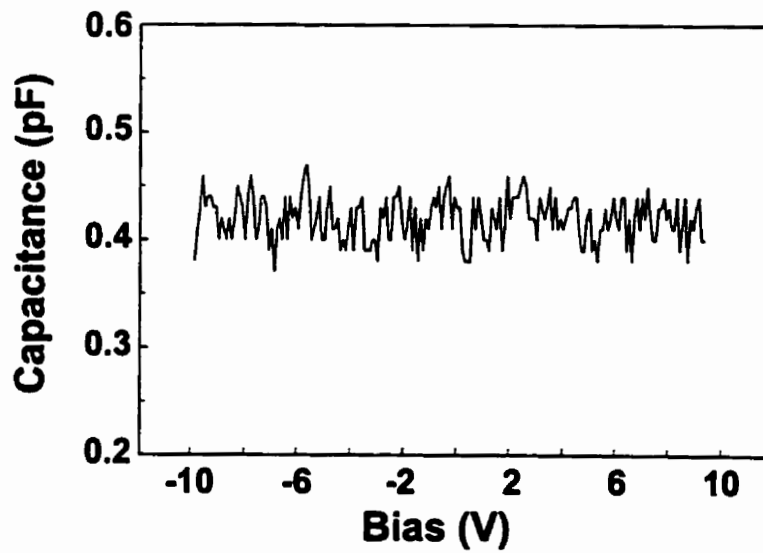
Figure 3.14: C-V measurements after prolonged stressing under 10 V.

Chapter 4

Electrical Noise

The detection resolution is ultimately limited by the noise intrinsic to the device, particularly at relatively low frequencies ($f \leq 10 \, kHz$), which is the frequency range of interest for detector operation [46, 10]. Although the exact mechanisms underlying noise have not been accurately identified, the trap and release of carriers is suspected to play a dominant role.

4.1 Measurement Setup

In the noise measurements, effects of extrinsic noise sources were minimized using the set-up shown in Fig. 4.1. The Schottky diodes were reverse biased using high amphour Sonnenschein sealed lead acid batteries and low noise metal film resistors. In these measurements, the value of the bias resistor (R) was chosen to be between $3.9 - 20 \, k\Omega$, depending on the signal level. The DC voltage drop across the resistor was filtered out using a high pass filter (HPF) with a corner frequency of $30 \, mHz$. The noise signals were subsequently amplified using a EG&G Brookdeal 5006 low noise amplifier (LNA),
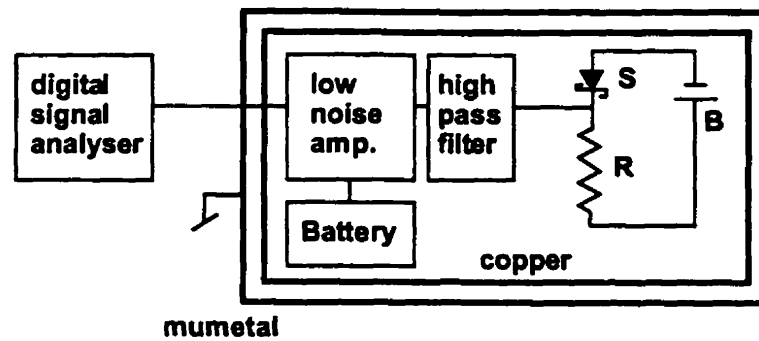
Figure 4.1: Experimental arrangement for low frequency noise measurements; S is the Schottky diode, R the biasing resistor, and B the bias source (battery).

which had a gain of 60 dB V. Power to the amplifier was supplied by similar, but separate, batteries in order to reduce possible noise coupling. The frequency response of the amplifier was 0.1 Hz to 1 $MHz \pm 3$ dB. Its equivalent input noise voltage was 13 nV $rms/\sqrt{Hz}$ at 10 Hz and 4 nV $rms/\sqrt{Hz}$ at 1 kHz. The equivalent input noise current of the LNA was 14 fA $rms/\sqrt{Hz}$ at 1 kHz. The output of the LNA was fed into a HP 3562A Dynamic Signal Analyzer which performed the necessary fast Fourier transform operations to yield the noise voltage power spectral density. The Schottky diode, HPF, and LNA were all housed in a double shielded enclosure composed of inner copper and outer mumetal boxes for shielding low frequency electrical and magnetic fields, respectively. The resulting system noise (at the LNA output), including the LNA and HPF, was better than -86 dB $V/\sqrt{Hz}$ at 1 Hz and -110 dB $V/\sqrt{Hz}$ at higher frequencies where white noise predominates.
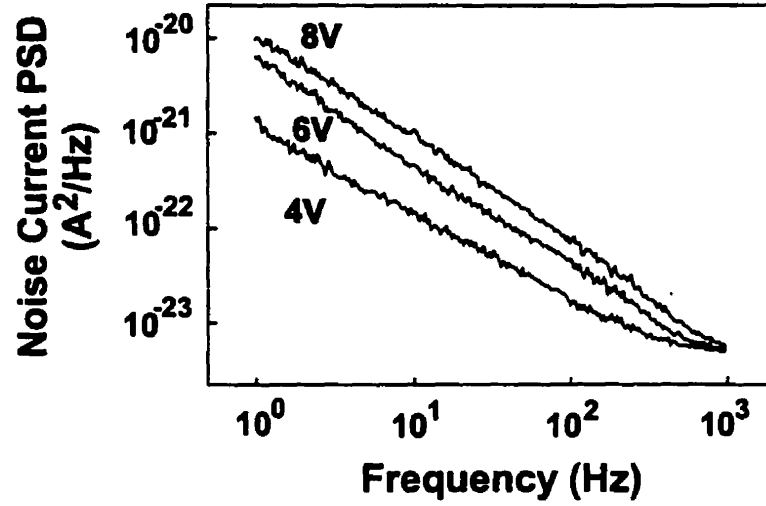
Figure 4.2: Measured power spectral densities for a 200 μm × 200 μm device at the indicated values of the reverse bias.

4.2 Noise Behavior in a-Si:H Schottky diodes

Results of the noise behavior are shown in Figs. 4.2, 4.3, and 4.4 for $f \leq 100 \, kHz$ [47]. The spectra were retrieved from measured values of noise voltage PSD appearing across bias resistor, viz.,$< v_n^2 > /R^2$. A series of test measurements showed that the resistor noise in the low frequency regime was much smaller than the noise from the Schottky diode itself. However, the resistor thermal noise was found to dominate at higher frequencies, particularly at low reverse bias operation. This finding can be further studied in light of the measurement equivalent circuit presented in Fig. 4.5. The associated noise voltage sources can be found using

$$< v_1^2 > = 4kTBR_{dynm},$$

$$< v_2^2 > = 4kTBR \qquad (4.1)$$
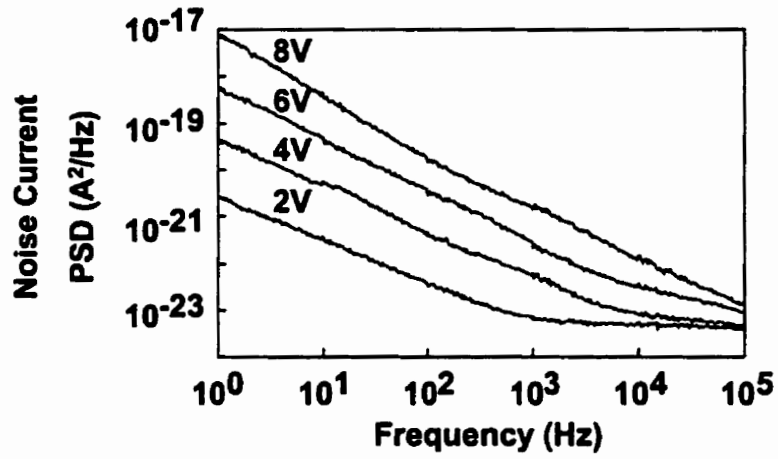
Figure 4.3: Measured power spectral densities for a 400 μm × 400 μm device at the indicated values of the reverse bias.
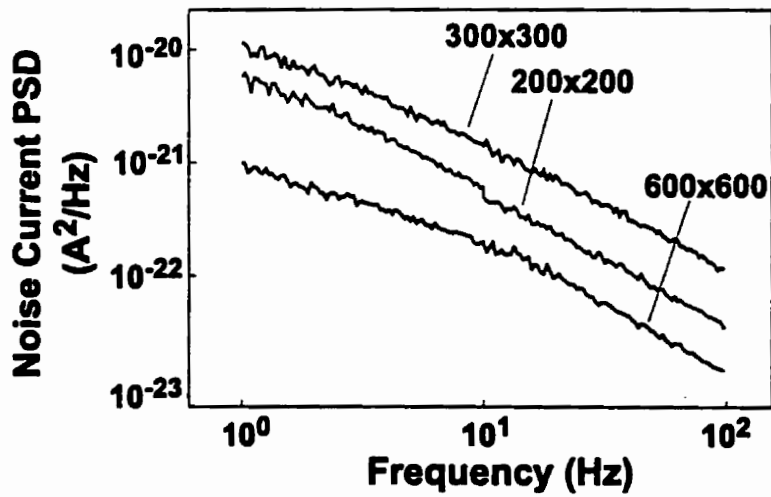
Figure 4.4: Measured power spectral densities for devices with various geometries (dimensions in μm) at 6 V reverse bias.
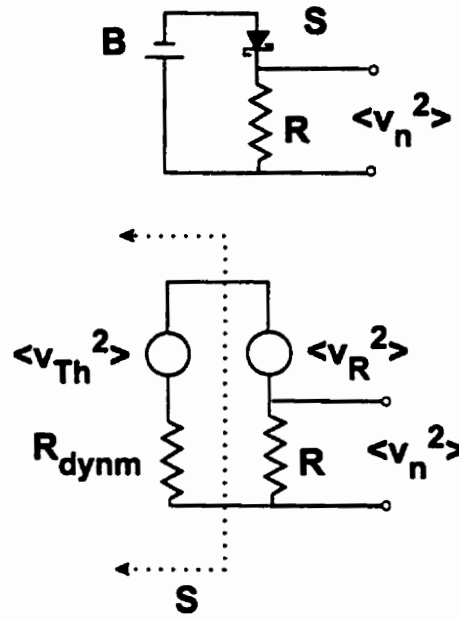
Figure 4.5: Schematic of the measurement circuit (top) and its equivalent noise circuit (bottom); B denotes the battery and S the Schottky diode.

where k is the Boltzman's constant, T is Temperature, B is the bandwidth, R is the bias resistor, and R_{dynm} is the dynamic resistance of the Schottky diode. Thus, the voltage appearing in the input of the LNA is given by [48]

$$< v_o^2 >=< v_{1o}^2 > + < v_{2o}^2 >, \tag{4.2}$$

or

$$< v_o^2 >= \frac{4kTBR_{dynm}R^2}{(R_{dynm} + R)^2} + \frac{4kTBR_{dynm}^2R}{(R_{dynm} + R)^2}, \tag{4.3}$$

or

$$< v_o^2 >= 4kTB\frac{R_{dynm}R}{(R_{dynm} + R)}. \tag{4.4}$$

Since in all the measurements, $R \ll R_{dynm}$, the dominant source of white noise at high frequencies comes from the bias resistor.

The spectra presented here were averaged over 100 waveform acquisitions. Sufficient time was provided for the reverse current to reach a reasonably steady value. The reverse current, measured before and after each spectrum acquisition, had a variation of less than 10%.

$1/f$ Noise

At low frequencies the measured noise current obeyed a $1/f^\alpha$ spectrum, with α ranging from 0.897 to 1.138. The measurements at various biases reveal the dependence of the noise current PSD on the reverse current as shown in Fig. 4.6. This dependence can be described by an empirical relation such as

$$< i^2_{1/f} >= \frac{K I^2_{rev}}{f}, \tag{4.5}$$

where K is the flicker noise parameter. Measurements on diodes with various geometries further revealed the dependence of the flicker noise parameter on the geometry of the device. This dependence, illustrated in Fig. 4.7, can be approximated as [49]

$$K \approx \frac{\gamma}{A}, \tag{4.6}$$

where A is the area of the diode , and γ is a parameter ranging from $(4 \ to \ 8) \times 10^{-8} \ cm^2$, which is affected by the electrical stressing of the diode. Therefore, the overall $1/f$ noise current takes the form

$$< i^2_{1/f} >\approx \frac{\gamma I^2_{rev}}{fA}. \tag{4.7}$$

Thermal Noise

The source of noise in these detectors is the thermal noise associated with the dynamic resistance of the reverse biased diode. This component can be studied in light of the
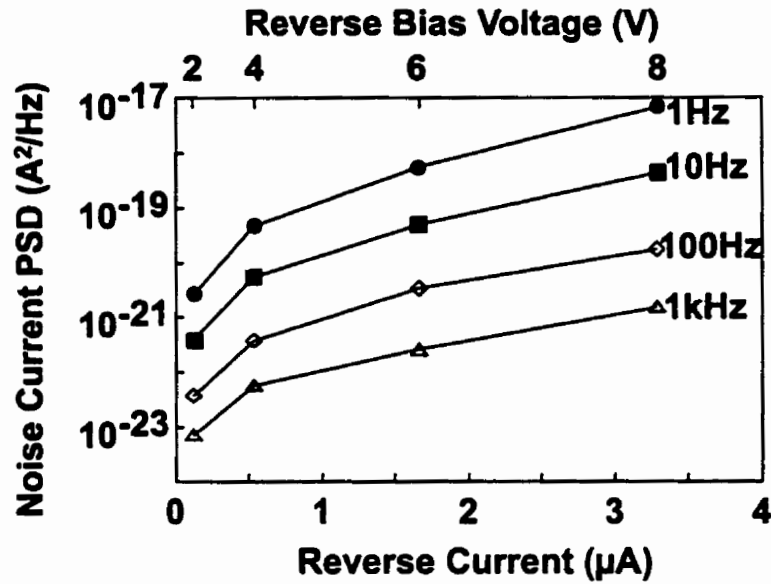
Figure 4.6: Measured power spectral densities as a function of bias for a 400 $\mu m \times$ 400 μm at the indicated frequencies.
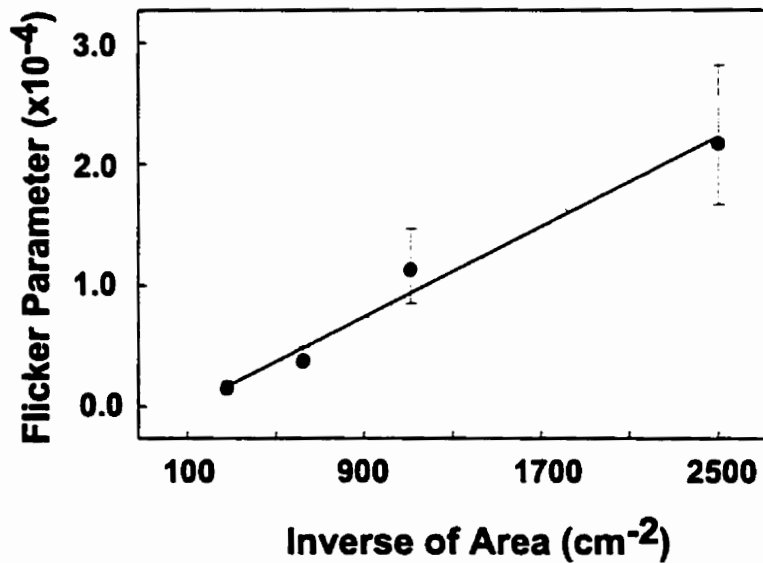
Figure 4.7: Variation of the flicker noise parameter, K in relation (4.5), with area of the diodes.
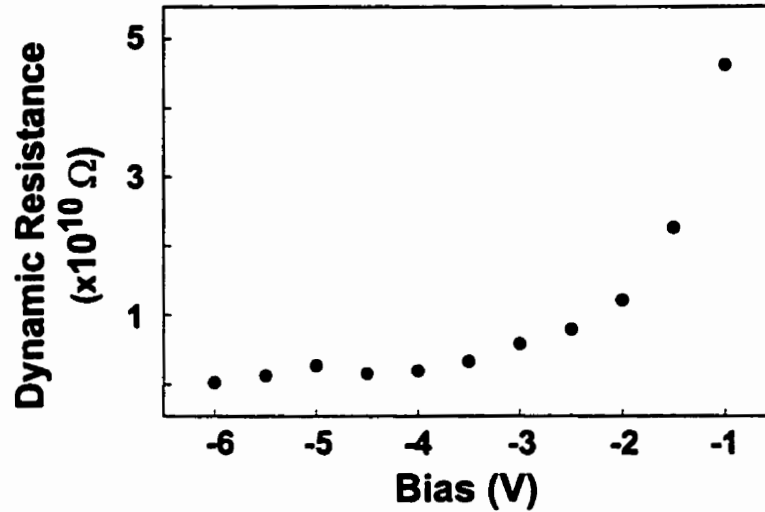
Figure 4.8: Typical measured variation of the dynamic resistance (dV/di) for Mo/a-Si:H Schottky diodes.

Johnson-Nyquist relation [50, 51, 52],

$$< v^2 >= 4kTBR_{dynm}, \qquad (4.8)$$

where k is the Boltzman's constant, T is Temperature, B is the bandwidth, and R_{dynm} is the dynamic resistance associated to the diode, which can be shown as

$$R_{dynm} = \frac{dV}{di}\|_{V=V_o}, \qquad (4.9)$$

where dV is the incremental variation of the applied bias around the DC bias point, V_o is the bias point, and di is the associated incremental current change. Such incremental variations can be further examined by using I-V relation for the reverse biased Schottky diodes, which can be approximated as

$$I(V) = I_o \exp\left(\frac{q}{kT}\|E\|\right). \qquad (4.10)$$

where I_o is the leakage current at zero bias, and E is the electric field at the interface, which is given by

$$E = -\sqrt{\frac{qN_D}{\epsilon_{si}\epsilon_o}}V, \qquad (4.11)$$

where V is the applied bias, N_D is the density of ionized sites, and ϵ_{si} is the relative dielectric constant of a-Si.

Expanding (4.10) using Taylor's expansion around a bias point (V_o) and ignoring higher order terms, yields [53],

$$I(V) = I(V_o) + I'(V_o)(V - V_o), \qquad (4.12)$$

where $I'(V_o)$ is the derivative of (4.10) at $V = V_o$. Rearranging (4.12), and using (4.9) gives,

$$R_{dynm} = \frac{\Delta V}{\Delta I} = \frac{1}{I'(V_o)}. \qquad (4.13)$$

Performing the differentiation for 4.10 results in

$$I'(V) = I(V_o)\sqrt{\frac{q^3 a^2 N_D}{kT\epsilon_{si}\epsilon_o}}\frac{1}{\sqrt{V_o}}\exp\left(\sqrt{\frac{q^3 a^2 N_D}{kT\epsilon_{si}\epsilon_o}}\sqrt{V_o}\right), \qquad (4.14)$$

By substituting (4.14) into (4.13), the dynamic resistance can be shown as

$$R_{dynm} = \sqrt{\frac{kT\epsilon_{si}\epsilon_o}{q^3 a^2 N_D}}\frac{\sqrt{V_o}}{I(V_o)}. \qquad (4.15)$$

A typical behavior of R_{dynm} with reverse bias is shown in Fig. 4.8.

Using (4.15) and (4.8), the noise current component resulting from the dynamic resistance of the Schottky diode can be shown by

$$< i_{th}^2 > = \frac{4kTB}{R_{dynm}}, \qquad (4.16)$$

or

$$< i_{th}^2 > = \frac{4kTB\sqrt{q^3 a^2 N_D}}{\sqrt{kT\epsilon_{si}\epsilon_o}} \frac{I(V_o)}{\sqrt{V_o}}. \tag{4.17}$$

Shot Noise

Current fluctuations in the Schottky diode give rise to shot noise. The shot noise component exhibits a dependence on the reverse current, which is given as

$$< i_{shot}^2 > = 2qI_{rev}, \tag{4.18}$$

where q is the electron charge. Due to the small values of the reverse current in the fabricated Schottky diodes (typically $1 - 100$ pA), the shot noise remains below the noise level of the measurement setup. This is illustrated in Fig. 4.9, where the overall computed noise is compared with the experimental results.

Total Noise

The overall noise in the Schottky diodes is sum of the individual components:

$$< i_{tot}^2 > \approx < i_{1/f}^2 > + < i_{Th}^2 > + < i_{shot}^2 > . \tag{4.19}$$

Replacing various components in (4.19), using (4.7), (4.17) and (4.18), yields

$$< i_{tot}^2 > \approx \frac{\gamma I_{rev}^2}{fA} + \frac{4kTB\sqrt{q^3 a^2 N_D}}{\sqrt{kT\epsilon_{si}\epsilon_o}} \frac{I(V_o)}{\sqrt{V_o}} + 2qI_{rev}. \tag{4.20}$$

Figure 4.9 illustrates the measured noise current PSD for a $200 \times 200\mu m^2$ detector. For comparison purposes, the computed values of various noise components are also included. Here, due to the measurement setup (see Section 4.2), the dynamic resistance of the diode and the load resistor are in parallel, so the thermal component of the noise is dominated by the load resistor.
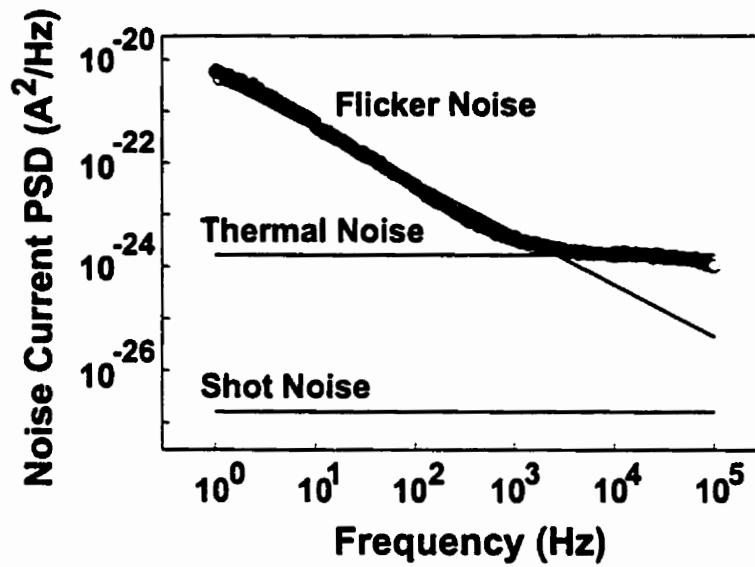
Figure 4.9: Computed $1/f$, thermal, and shot noise components as a function of frequency for a 200 μm × 200 μm device. Symbols denote the measured data, and solid lines denote the computed noise components for $\gamma = 7 \times 10^{-8}$, and $R_{load} = 10$ $k\Omega$.

Chapter 5

X-ray Sensitivity

This Chapter investigates the performance of the fabricated detectors in the presence of X-ray radiation. Experimental and numerical analyses of sensitivity have also been carried out to investigate the impact of various geometry and bias conditions on the sensitivity.

Section 5.1 introduces the principles of X-ray generation. This is followed in Section 5.2 by an examination of possible interactions an X-ray photon can undergo while moving through a medium. The energy loss and absorption mechanisms of the generated photoelectrons are the subject of Section 5.3. Section 5.4 introduces an approximate model to describe the transduction process, and this is followed by a description of the measurement setup in Section 5.5 along with experimental results in Section 5.6.

5.1 Generation of X-rays

X-rays are generated when electrons with high energy strike a target made from materials such as tungsten and molybdenum [54, 55, 56]. The high energy electron can interact

65
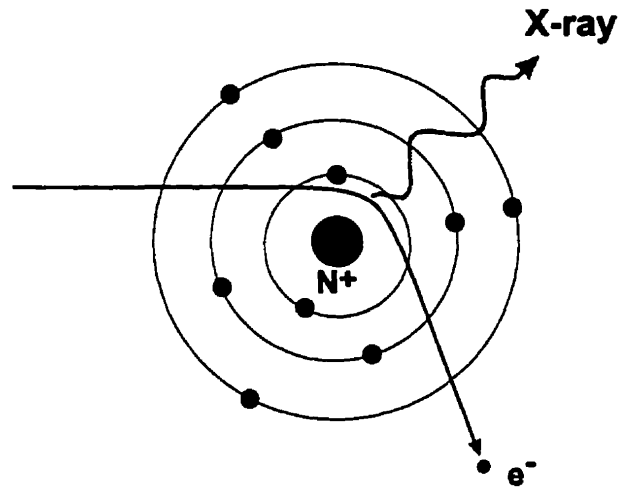
Figure 5.1: Deflection of energetic electrons near a nucleus.

with the nuclei of the target atom and produce so-called white radiation, or they can interact with atomic electrons to produce characteristic radiation. When an electron that is negatively charged passes near a positively charged nucleus, the electron is deflected from its original path by the columbic attraction to the nucleus. As a result of this deflection, the electron can lose its energy, which is emitted as X-ray radiation (Fig. 5.1). The energetic electrons can also interact with the atomic electrons of the target and remove them from inner shells (such as the K-shell). This places the atom in an excited state. Consequently, an electron from a higher energy level will move down in energy and fill the empty level in the K-shell. The energy difference between the two states is emitted as electromagnetic waves, yielding an X-ray photon.

In a medical X-ray source, the electron source and target material form the cathode and anode, respectively, of a vacuum tube [57, 54]. The electrons emitted by the cathode are accelerated in a high electric field towards the anode, causing X-ray emissions. The generated X-rays have a wide energy distribution; various factors determine this distribution, e.g., tube voltage, tube current, and the target material. The shape of the spectrum
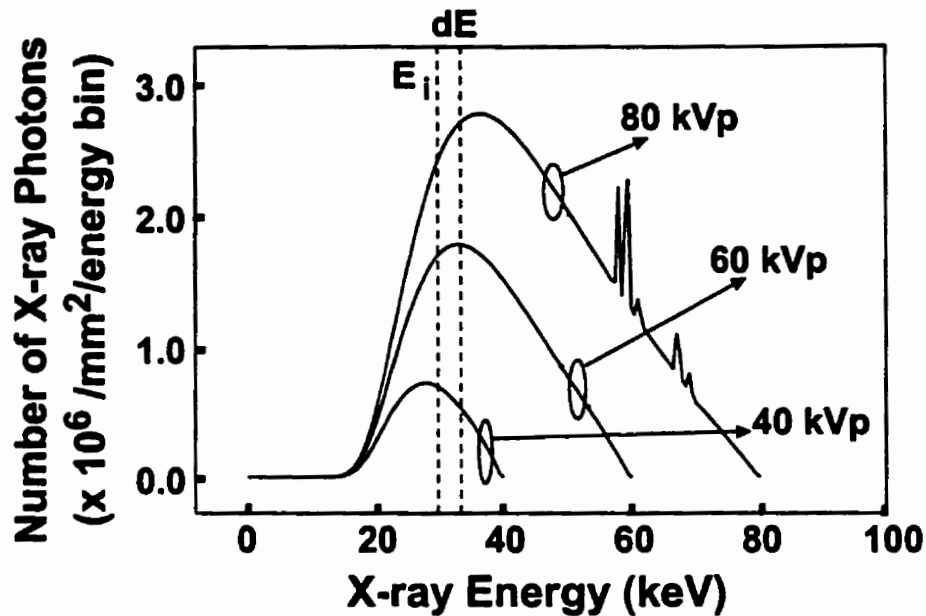
Figure 5.2: X-ray spectrum at a distance of 39 cm for tungsten target generated by XRAYLIB from University of Western Ontario; the tube current is 25 mAs.

is primarily determined by the target material, which for radiology applications is often tungsten [54]. The tube voltage defines the peak potential difference between the electrodes (expressed using the symbol kVp) and mainly determines the maximum energy of the X-ray photons. The tube current specifies the current between the electrodes (expressed using mAs) and predominantly controls the intensity of the X-ray beam.

The simulated X-ray spectra generated from a tungsten target (General Electric tube) for different tube potentials are shown in Fig. 5.2. This spectrum is produced using the XRAYLIB software compiled by University of Western Ontario, London, Ontario [58, 59]. As the tube potential is increased, the maximum photon energy is also increased; however, the overall shape of the spectrum remains approximately the same.

5.2   Interactions of X-ray Photons with Matter

In this section, various mechanisms of interaction between incoming X-ray photons and matter are studied. In general, the incoming X-ray photon may interact with matter in one of three ways depending on its energy:

- Photoelectric effect

- Compton interaction

    - Rayleigh scattering

    - Thomson scattering (classic limit)

- Pair production.

In pair production effect, the incoming photon loses its energy by creation of an electron-positron pair. Based on the energy conservation law, the minimum photon energy required for this interaction is $2m_o$, where m_o is the rest mass of the electron (≈ 0.511 MeV). In all of our experiments, the energy range of X-ray photons is much less than the required threshold energy for observing electron-positron pairs.

In Compton interactions, an X-ray photon interacts with an electron and transfers part of its energy to that electron. Due to this transfer of energy, the wavelength of the photon is changed. Related to Compton scattering are the classical Thomson and Rayleigh scattering events. In Thomson scattering, a photon is scattered by a free electron in the classic limit ($\frac{v}{c} \ll 1$). On the other hand, with Rayleigh scattering, the photon is coherently scattered by all the electrons of an atom. In both of these processes, no energy is transferred to the bulk material. Although a Compton interaction has a finite probability of occurring at low energies, this probability peaks in the range of a few hundred keV to a few MeV.
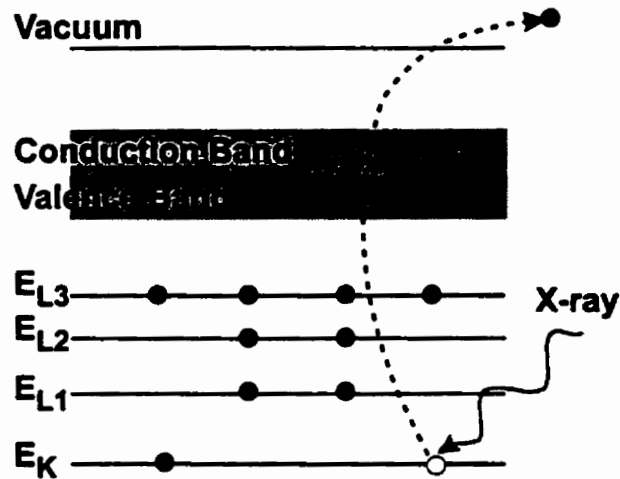
Figure 5.3: Photoelectric interaction between X-ray photon and atom.

The photoelectric effect is the dominant interaction at the low energy range (up to a few hundred keV). In this interaction, a photon transfers its energy to a bound electron and excites the electron to the vacuum level (Fig. 5.3).

From conservation of energy,

$$h\nu = E_{bind} + T, \tag{5.1}$$

where $h\nu$ is the photon energy, E_{bind} and T are the binding energy and final kinetic energy of the electron, respectively. The generated free electron, referred to as the photo-electron, can travel through matter and interact with other electrons. For sufficient initial kinetic energies, it can also ionize other atoms.

The ejection of photoelectrons from an atom is not an isotropic process, peaking around a particular direction. This direction is primarily determined by the energy of the incoming photons. For the energy range of interest ($10\ keV < E < 100\ keV$), the most probable emission direction makes an angle α with the incoming electrons. Here α ranges from $70°$ to $50°$ [60].

As with other nuclear interactions, the probability of a photoelectric interaction can be studied using the concept of an interaction cross-section. Here the photoelectric cross-section depends not only on the target material, but also on the energy of incoming photons. This dependence can be expressed empirically by the following approximate relation [54],

$$\sigma_{photo} \propto Z^3 E^{-3},\qquad(5.2)$$

where Z is the atomic number, and E is the energy of X-ray photon. However, the accuracy of relation (5.2) degrades at energy ranges close to the K-shell, which are of interest here. Based on the photoelectric cross-section, we can define a mean free path for photons as

$$\lambda_p = \frac{A_w}{\rho N_a \sigma_{photo(E,Z,\rho)}},\qquad(5.3)$$

where A_w is the atomic weight, N_a is the Avogadro's number ($= 6.02217 \times 10^{23}$ mol^{-1}), and ρ is the density. The attenuation of photon intensity can then be shown to be

$$I_p = I_{op}\exp\left(-\frac{x}{\lambda_p}\right),\qquad(5.4)$$

where I_p is the X-ray intensity after traveling through a thickness x of the target, and I_{op} is the initial intensity of X-ray photons. Often, obtaining an analytical relation for the mean free path of X-ray photons either results in complicated and inaccurate relations, or it is not possible at all. Therefore, tabulated values of mean free path from experimental observations are used.

These values reveal that the photoelectric absorption reaches its maximum at energies close to the K or L shell energies of the absorbing material and that it falls off for higher energies.

5.3 Transmission of Photoelectrons

In the proposed detection scheme, the ejection of photoelectrons and further multiplication in the a-Si:H layer are the key steps in the transduction process. Therefore, the performance and efficiency of these detectors are influenced by the transmission of photoelectrons through the metal layer and by interactions in the a-Si:H layer. The mechanism by which photoelectrons lose their energy and are absorbed in the material depends on the initial kinetic energy of the photoelectrons. During transmission through the target material, the photoelectrons experience various collisions with the other electrons and atoms. Often these interactions are classified into elastic and inelastic collisions [61]. During an elastic collision, a photoelectron experiences a deviation from its original direction without losing its energy. However, in an inelastic interaction, the photoelectron transfers some of its kinetic energy to other electrons, or loses energy by radiation.

Some of the possible inelastic collisions can be classified as processes that

- generate X-rays, e.g., Bremsstrahlung

- generate secondary electrons, e.g., collision loss with inner shell electrons, and excitation of the outer shell electrons

- result in collective interaction with many atoms, e.g., plasmons, and phonons.

Bremsstrahlung

Radiative loss of energy will occur for all electrons that interact with matter. One way of explaining this effect is to use the classical picture of electromagnetic radiation by an accelerated charge. In the low energy range, this energy loss mechanism is responsible for only a small percentage of the electron energy loss, so-called soft Bremsstrahlung

radiation. However, this mechanism becomes dominant for electron energies above, approximately [62],

$$E_B = \frac{800\ MeV}{Z + 1.2}.\tag{5.5}$$

Typical threshold energies are in the range of a few MeV, so this interaction has a minor effect on the energy range that is of interest in this research.

Collision Losses

In the energy range of 100 $keV > T > 10\ keV$, the interaction of photoelectrons with inner shell electrons is the predominant collision mechanism. Photoelectrons can remove atomic electrons from the inner shells, such as the K, L, and M shells. This causes ionization of the target atoms and generation of secondary electrons. In this energy range, various models have been proposed to explain the variation of the inner shell ionization collision cross section with different parameters, including the incoming electron energy [63, 64, 65, 66, 67, 68]. Moller's cross section is the most widely used model which for the differential cross section yields

$$d\sigma = \frac{2\pi r_e^2 mc^2}{\beta^2} \frac{dP}{P^2} \left[1 + \frac{P^2}{(T-P)^2} + \frac{\tau^2}{(\tau+1)^2} (\frac{P}{T})^2 - \frac{(2\tau+1)}{(\tau+1)^2} \frac{P}{(T-P)} \right],\tag{5.6}$$

where r_e is the classic electron radius (2.8179 × 10^{-13} cm), mc^2 is the electron rest mass, β is the velocity of the incident electron divided by the speed of light, P is the energy transfer to the medium, and τ is the ratio of the kinetic energy of the incident electron to its rest energy ($\tau = T/mc^2$). Relation (5.6) is based on the assumption that the energy transferred is larger than the binding energy of the electron. The validity of this assumption weakens at low energies (200 $eV < T < 5\ keV$), where the binding energy is comparable to the initial kinetic energy. Despite the wealth of knowledge in

the high energy range, the interaction mechanisms in the low energy range are still the subject of discussions [65, 66]. However, in the lack of a widely accepted model, the Moller cross section can still be used as an approximation.

Another useful parameter is the stopping power (S), which describes the energy loss of electrons while traveling in a material as

$$S = -\frac{dT}{dx},$$

(5.7)

where dT is the incremental energy loss while the electron is traveling an incremental distance dx in the matter, and this is based on the continuous slowing down approximation (csda). The energy loss is primarily achieved through inelastic collisions; therefore,

$$S = \frac{\rho N_a Z}{A_w} \int P \frac{d\sigma}{dP} dP.$$

(5.8)

From (5.8) and (5.6), the stopping power for impact ionization is given by

$$S = 2\pi r_e^2 mc^2 \rho Z \frac{N_a}{A_w} \left[\ln \left(\frac{T}{I_{ion}} \right)^2 + \ln \left(1 + \frac{\tau}{2} \right) + F(\tau) - \delta \right],$$

(5.9)

with

$$F(\tau) = (1 - \beta^2) \left[1 + \frac{\tau^2}{8} - (2\tau + 1) \ln 2 \right],$$

(5.10)

where I_{ion} is the mean excitation energy, and δ is the density-effect correction [62, 68]. Since the photo-generated electrons on average have a kinetic energy in the range of a few keV, relation (5.9) can provide a good approximation for the energy loss in the metal. Using the stopping power (5.7), a thickness (referred to as the range, R_e) can be defined in which the incoming electron completely loses its kinetic energy and stops, so

$$R_e = \int_0^{T_o} \frac{1}{S} dT,$$

(5.11)

where T_o defines the initial electron kinetic energy. Unfortunately, relation (5.9) does not lead to a closed form expression for the range of electrons. However, using a different
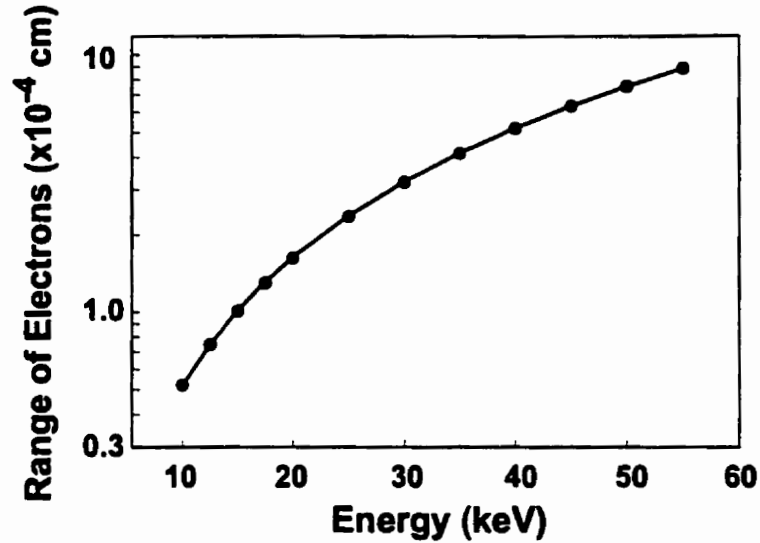
Figure 5.4: Range of electrons in bulk Mo as a function of their kinetic energy. Solid line indicates the fit using relation (5.12) and symbols denote values from ICRU report 37.

approach, Kanaya *et. al.* have suggested [63],

$$R_e = \frac{A_w T_o^{5/3}}{15.874\pi a^{1/3}\lambda_e q^{10/3} N_a \rho Z},$$ (5.12)

where λ_e is a fitting parameter (suggested value of ≈ 0.182), and

$$a = 0.8853 a_H Z^{-1/3},$$ (5.13)

where a_H is the Bohr radius of hydrogen atom (5.292×10^{-9} *cm*). Figure 5.4 illustrates the fit between the range obtained from (5.12) and the tabulated values published by International Commission on Radiation Units and Measurements (ICRU) [64]. The fit yields $\lambda_e \approx 0.1532$.

Kanaya's theory also yields a closed form relation for the mean free path, where the intensity of the incoming electrons diminishes to $1/e$ of its initial value, as

$$\lambda_c = \frac{5.025 \times 10^{-12} A T^{5/3}}{\rho \lambda_e Z^{8/9}} \frac{1}{1 + 0.187 Z^{2/3}}, \tag{5.14}$$

Another source of energy loss is due to collisions of photoelectrons with the outer shell electrons of the target material, such as valence band electrons. This is a major energy loss mechanism for low energy electrons ($T < 200$ eV), by which the initial photoelectron energy is finally transferred into creation of e-h pairs inside a-Si:H. Given the lack of an analytical model, empirical values are the only sources of information about the average energy that is expended towards creation of an e-h pair.

Phonon and Plasmon Excitations

Photoelectrons can also lose their energies by interaction with phonons. However, a phonon vibration causes only a very small energy loss of < 1 eV; therefore, it is assumed to be negligible in this study.

In the energy range of 50 $eV < T < 1$ keV, the photoelectrons can also interact with a gas of free electrons, and excite electron oscillations known as plasmons [69, 70]. In reality, these electrons are loosely bound to the atoms but, since their binding energy is much smaller than the incoming electron energy, they can be approximated as a gas of free electrons [71, 72, 73]. The cross-section of electrons in this range can be shown to be [69]

$$\sigma = \frac{\Delta T}{4 a_h T} \ln(\theta_{cut}/\theta_E), \tag{5.15}$$

where θ_{cut} is the cut off angle, ΔT is the energy loss ($\approx 10 - 15$ eV), and θ_E is given by

$$\theta_E = \frac{\Delta T}{2T}. \tag{5.16}$$

The mean free path can be shown to be [74],

$$\lambda_e^{-1} = \sqrt{3} \frac{a_h R_y r_e^{-3/2}}{T} \ln((\frac{4}{9\pi})^{2/3} \frac{T r_e^2}{R}), \tag{5.17}$$

where $R_y = 13.6 \ eV$ is the Rydberg constant, and r_a is the average electron distance. Since the energy loss by this mechanism is small compared to the energy losses that electrons suffer from impact ionization, the contribution of this mechanism is considered negligible for this study.

5.4 An Approximate Model

The detector quantum yield (the ratio between measured number of electrons to the incoming X-ray photons) can be further studied by arranging the detector transduction process into various stages of conversion (Fig. 5.5). Thus, the overall performance of the detector (G) for a mono-energetic X-ray beam can be shown in terms of the efficiencies of different stages as,

$$G = \eta(\zeta\gamma\chi + \kappa),\tag{5.18}$$

where η is the photoelectron generation efficiency, ζ is the ejection efficiency of the photoelectrons, γ is the e-h generation efficiency in the a-Si:H by the ejected photoelectrons, χ is the e-h separation efficiency in a-Si:H, and κ is the contribution to the thermionic emission caused by photoelectrons absorbed in the Mo layer. Relation (5.18) is particularly important in order to examine the impact of different parameters on the detector performance.

Photoelectron Generation

The photoelectric absorption of X-ray photons in the Mo layer is the first stage, and for every photon absorbed, an energetic electron is released. The photoelectron generation efficiency (η) can be determined from [62],

$$\eta = \frac{n_{abs}}{n_{inc}} = \left[1 - \exp(-\frac{x}{\lambda_p})\right],\tag{5.19}$$
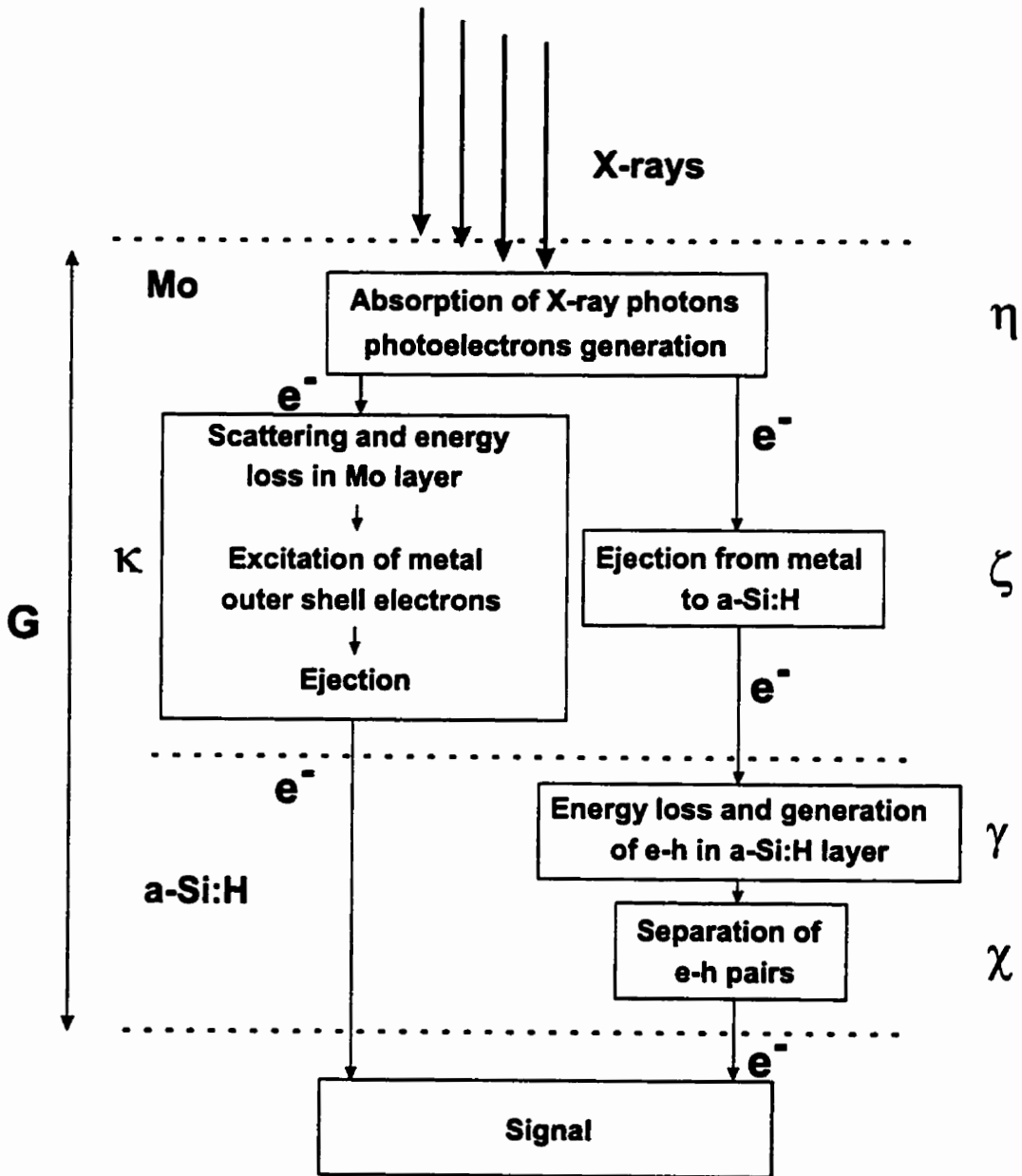
Figure 5.5: Schematic representation of the transduction process with Mo/a-Si:H Schottky diodes; greek symbols refer to the efficiency of each process.

where $1/\lambda_p$ is the energy-dependent photoelectric attenuation coefficient, x is the thickness of the film, n_{abs} is the number of absorbed X-ray photons, and n_{inc} is the number of X-ray photons impinging on the surface of the detector. For this study, the values of photoelectric attenuation coefficient for bulk molybdenum are used, as provided by XRAYLIB [58]. These values, related to atomic structure, are expected to be similar in thin films.

The initial photoelectron kinetic energy, as shown previously in relation (5.1) is given by,

$$T = h\nu - E_{bind}. \tag{5.20}$$

Photons with energies less than E_{bind} do not interact with atomic electrons. Hence, the E_{bind} in relation (5.20) is determined by the energy of the X-ray photon, from the possible values of $E_K = 19.97\ keV$ and $E_L = 2.87\ keV$, for molybdenum.

After ejection from the atom, most of the photoelectrons travel towards the a-Si:H along a path which makes an angle α with the original X-ray direction. For this study, an average value of 60° is assumed.

Photoelectron Transmission

Not all the energetic photoelectrons reach the a-Si:H layer; some of them undergo various inelastic scattering events and lose their energies to the metal film. The distance that photoelectrons travel before being scattered is given by the mean free scattering path (λ_e), and it depends on the kinetic energy of the electrons. In this study, it is assumed that the dominant energy loss mechanism is the inner shell impact ionization process, and relation (5.14) has been used to obtain approximate values for the mean free path. Hence the number of photoelectrons escaping from the metal film can be approximated

as [62]

$$n_e = n_{eo} \exp\left(-\frac{y}{\cos(\alpha)\lambda_e}\right),$$ (5.21)

where n_e is the number of photoelectrons reaching the a-Si:H, n_{eo} is the initial number of photoelectrons, and y is the distance that photoelectrons travel. Since the photoelectric absorption occurs in a thin layer of Mo, the X-ray intensity can be assumed approximately constant through out the Mo thin film (see for example Section 10.9 in [75]), leading to a uniform distribution of generated photoelectrons. Therefore, the photoelectrons travel different distances to reach the a-Si:H layer (Fig. 5.6). The ejection efficiency (ζ) can be found by summing contributions from different parts of the Mo layer,

$$\zeta = \int_o^{t_{Mo}} \frac{1}{t_{Mo}} \exp\left(-\frac{y}{\cos(\alpha)\lambda_e}\right) dx,$$ (5.22)

where t_{Mo} is the thickness of the Mo layer. In relation (5.22), it is assumed that the number of photoelectrons in a strip of thickness dx is given by,

$$dn = \frac{n_{e-tot}}{t_{Mo}} dx,$$ (5.23)

where n_{e-tot} is the total number of generated photoelectrons, which is approximately equal to the total number of absorbed photons. Integration of (5.22) yields,

$$\zeta = \frac{\cos(\alpha)\lambda_e}{t_{Mo}} \left[1 - \exp\left(-\frac{t_{Mo}}{\cos(\alpha)\lambda_e)}\right)\right].$$ (5.24)

Electron Hole Pair Generation Efficiency

After ejection from the Mo layer, the energetic photoelectrons encounter various scattering events and lose their energies inside the a-Si:H film. It is assumed that the impact ionization with inner shell electrons causes the major energy loss for photoelectrons in a-Si:H, as well. From Kanaya's relation, the electron energy in the a-Si:H, after traveling
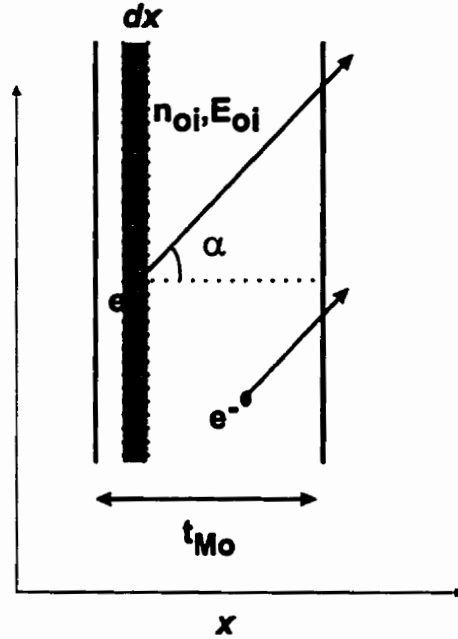
Figure 5.6: Transport of photoelectrons before ejection from Mo layer.

a distance x, can be estimated from

$$T = (1 - \frac{x}{R_{Si}})^{3/5}T_{Si},\qquad(5.25)$$

where R_{Si} is the energy dependent range of photoelectrons defined by the total distance that electrons travel before being completely stopped, and T_{Si} is the initial kinetic energy of the electrons when they reach the a-Si:H film. Thus, the energy loss of photoelectrons in the a-Si:H film (ΔT_{Si}) can be approximated as

$$\Delta T_{Si} = \left\{ 1 - \left[1 - \frac{t_{Si}}{\cos(\alpha)R_{Si}} \right]^{3/5} \right\} T_{Si},\qquad(5.26)$$

where t_{Si} is the thickness of the a-Si:H. Part of the deposited energy is transferred to excite electrons from valence to conduction bands in the a-Si:H to generate multiple e-h pairs. Often the efficiency for converting the deposited energy to e-h pair creation is expressed by an empirical factor known as the W factor, which reflects the average

energy that a photoelectron loses to generate one e-h pair. Thus, the generation efficiency can be shown as,

$$\gamma = \left\{ 1 - \left[1 - \frac{t_{Si}}{\cos(\alpha)R_{Si}} \right]^{3/5} \right\} \frac{T_{Si}}{W}. \tag{5.27}$$

For thicknesses greater than the projected range ($t_{Si} > R_{Si} \cos(\alpha)$), the γ reduces to

$$\gamma = \frac{T_{Si}}{W}, \tag{5.28}$$

where most of the ejected photoelectrons stop in a-Si:H layer.

For the fabricated a-Si:H films, a W factor of 3.7 eV generates the best fit to the experimental data. This is comparable to 3.68 eV for crystalline silicon [1].

Separation Efficiency

After the generation, the effective separation of the e-h pairs is crucial, owing to the small diffusion length in a-Si:H. Hence, it can be assumed that the main contribution to the signal is raised from e-h pairs generated inside the depletion region, where the electric field enhances the separation of the pairs. Considering this effect, the separation efficiency can be approximated by

$$\chi = \frac{w}{t_{Si}}, \tag{5.29}$$

where w is the depletion width.

Relation (5.29) is based on the assumption that the generated charge does not disturb the electric field inside the depletion region. It is also assumed that the net bias across the Schottky diode remains constant. The accuracy of this model degrades as the number of generated electron hole pairs increases since this alters the electric field inside the depletion region. Here, a complete numerical solution of Poisson's equation and continuity relation are required, which is beyond the scope of this thesis.

Thermal Emission

In addition to the ejected photoelectrons, the photoelectrons absorbed in the Mo layer also contribute to the signal. The energy that these photoelectrons lose in the Mo (ΔT_{mo}) can be shown as

$$\Delta T = T \left[1 - \exp \left(-\frac{x}{\cos(\alpha)\lambda_e} \right) \right], \tag{5.30}$$

where T is the initial kinetic energy of electrons (5.20). Part of the energy lost by these photoelectrons is then transferred to excite the outer shell electrons of the metal. If the excited electrons acquire energies comparable to the barrier height ($\approx 0.77\ eV$), they can take part in the thermionic emission over the barrier. However, only those electrons within the carrier-carrier scattering length of the Mo/a-Si interface can contribute to the current. Hence, the efficiency for the thermionic emission over the barrier can be shown as,

$$\kappa = \frac{\Delta T}{u} \frac{s}{t_{Mo}}, \tag{5.31}$$

where u is the average energy that photoelectrons spend to excite an electron to a state above the barrier height ($\approx 1\ eV$ assumed), and s defines the average distance that electrons travel before being scattered. Although, the scattering length for metals can be as high as 1 μm [76], a thickness in the range of 80 nm is found to produce the best fit to the experimental results. The smaller carrier-carrier scattering length can be explained by considering the larger density of structural defects and interface effects.

Summary of Transduction Efficiencies

A summary of the various transduction processes along with their typical numerical values are given in Table 5.1. These values are calculated for a monoenergetic X-ray beam of 20 keV. This is comparable to the average energy of a medical X-ray source of 40 kVp.

	Governing equation and parameter values	Mo		W	
		Typical	Cumulative	Typical	Cumulative
η	(5.19) $\lambda_{p-Mo} \approx 12\ \mu m$, $t_{Mo} \approx 0.4\ \mu m$	0.033	0.033	0.05	0.05
ζ	(5.24) $\lambda_{e-Mo} \approx 0.58\ \mu m$	0.55	0.0165	0.508	0.0254
γ	(5.28) $T_{Si} \approx 17.5\ keV$	5830	96.2	5830	148
χ	(5.29) $w \approx 0.3\ \mu m$, $t_{Mo} \approx 0.4\ \mu m$	0.8	76.8	0.8	118
κ	(5.31) $T \approx 17.5\ keV$, $\zeta \approx 0.5$	2000	143	2150	220

Table 5.1: A summary of various transduction efficiencies, their governing-equation numbers, and typical values for Mo and W. The cumulative values represent the accumulated gain in each stage of the transduction process.

Spectrum of X-ray Energies

Since a medical X-ray source generates a broad spectrum of X-ray energies, the overall performance can only be found by numerical summation of the efficiencies over the entire range of X-ray energies obtained from XRAYLIB. This is achieved by dividing the spectrum into narrow energy ranges, where it is assumed that the energy is constant at E_i (as shown in Fig. 5.2).

Heating

Part of the absorbed X-ray energy can also be transferred to heat and can thereby cause a temperature increase. This upper bound for increase in temperature can be estimated by

assuming that the absorbed energy in the metal film is entirely transferred to heat, so

$$Q = E_{abs} = \sum_i n_{abs,i} E_i, \tag{5.32}$$

where $n_{abs,i}$ is the number of X-ray photons absorbed from the ith energy interval, E_i is the energy of ith interval, and Q is the heat absorbed in Mo layer. The temperature increase ($\Delta\theta$) can be shown as,

$$\Delta\theta = c_{Mo} V_{pixel} \rho_{Mo} Q \tag{5.33}$$

where ρ_{Mo} is the density of Mo ($\approx 10.2~g/cm^3$), c_{Mo} is the specific heat of Mo ($\approx 0.25~Jg^{-1}K^{-1}$), and V_{pixel} is the volume of a pixel ($= 200 \times 200 \times 0.5~\mu m^3 = 2 \times 10^{-8}~cm^3$).

This temperature difference can introduce an increase in the reverse current given by,

$$\frac{\Delta I}{I} = \frac{\phi_{eff}}{k\theta} \frac{\Delta\theta}{\theta}, \tag{5.34}$$

where ϕ_{eff} is the effective barrier height, ΔI is the variation in the reverse current, and I is the reverse current.

From XRAYLIB, a maximum energy of $4.9 \times 10^{-10}~J$ is found to be absorbed in the Mo film of a pixel ($= 200 \times 200 \times 0.5\mu m^3$) at 40 kVp, 25 mAs, and 39 cm for 500 ms exposure; this yields a temperature increase of 0.01 K. Assuming room temperature, and a barrier height of 0.77 eV in (5.34), yields a change in reverse current, and hence in measured voltage, of 0.1%. This is significantly lower than the experimental change in voltage of $\approx$ 14%.

Other sources of temperature variations can be overcome by calibration prior to X-ray exposure.

5.5 Measurement Setup

The sensitivity measurements of the fabricated detectors have been performe⊏ medical X-ray source at the Robarts Research Institute, University of Western In addition to these studies, elementary characterization has been performec⊏ scientific source at the University of Waterloo.

The read-out scheme was based on sensing the accumulated charge alor⊏ capacitor, illustrated in Fig. 5.7. The Schottky diode was biased using a Keithle⊏ Measure Unit (SMU) model 236 with a voltage resolution of 10 μV. The load ⊏ was a high quality polyester type, with a value of 150 $pF \pm 2\%$. The voltage a⊏ load capacitor was buffered by an OP-80 operation amplifier from Analog Devi⊏ a low input current ($\approx 0.2 \ pA$). Subsequently, the voltage was measured by a 2001 Digital Multi-meter, with a resolution of 10 μV in the fast integration m⊏ data acquisition was performed by a PC, which also controlled the SMU.

The bias on the Schottky diode was alternatively switched between rev⊏ (800 ms @ $- 2 \ V$) and zero bias ($1 - 2 \ s$), owing to the delay of the PC. In bias period, the load capacitor was reset by the Schottky diode, which is forwar⊏ during this period. This scheme was adopted since the other scheme of resetting capacitor causes a dissipation of charge through the leakage current, hence degra⊏ signal. The pulse height was chosen to be $-2 \ V$ in order to avoid metastabilit⊏ intrinsic to a-Si:H Schottky diodes (see Section 3.4). The pulse width was deterr⊏ considering the characteristics presented in Fig. 5.8. Although very long pulse⊏ faster stabilization of the Schottky diodes, the voltage increase across the load c⊏ causes degradation in the charge separation efficiency.

The chosen magnitude of the load capacitor was based on a trade-off between resolution and maintaining the reverse bias on the Schottky diode. A small c⊏
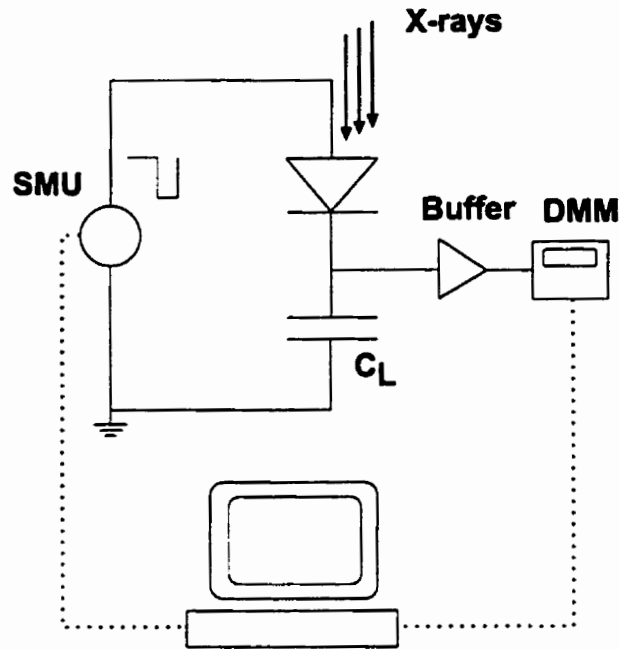
Figure 5.7: Schematic diagram of the setup used for X-ray measurements.

permitted a very accurate sensing of charge; however, the voltage along the Schottky quickly decreased to zero, hence degrading the charge separation. Although a large capacitor could sustain the voltage along the Schottky diode for a longer period of time, this undermines the sensitivity of the measurement.

With a reverse bias on the Schottky diode, the X-ray source was turned on. Prior to X-ray experiment, sufficient time was given for the Schottky diode reverse current to stabilize. The larger reverse current obtained by presence of X-rays has accumulated on the load capacitor (Fig. 5.9). The X-ray exposure period (500 ms) was always shorter than the reverse bias period.

Since the secondary X-ray radiation from the standard IC packages can disturb the accuracy of the measurements, a new packaging scheme was developed. In this method the dice was attached directly to a specially designed PC board (Fig. 5.10). Another

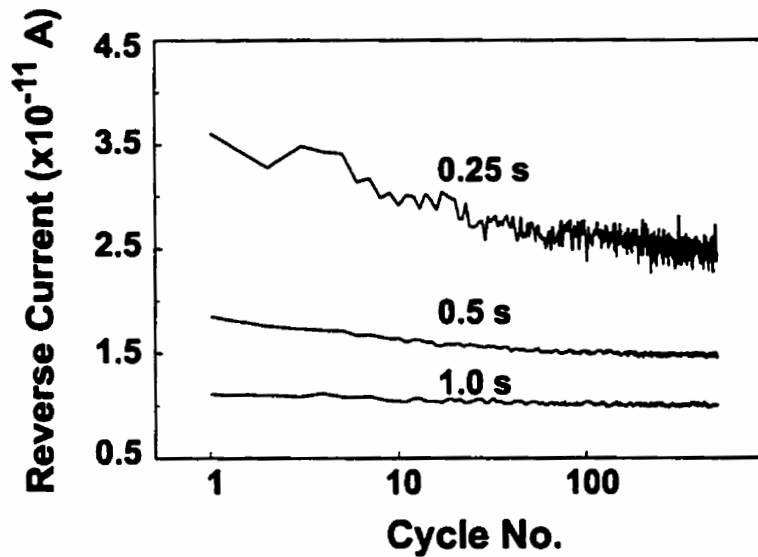Figure 5.8: The time-dependent variation of the reverse current with number of pulse cycles in Mo/a-Si:H Schottky diodes, for different pulse durations indicated in graph. The pulse was alternatively switched in equal intervals between $-2, 0, +2$ V.
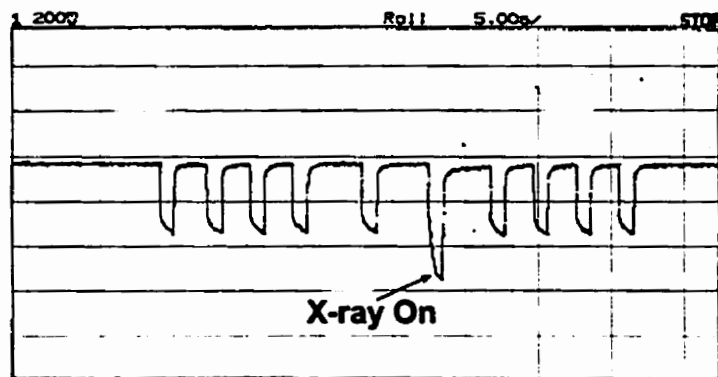

Figure 5.9: Typical voltage response measured with an oscilloscope across a 150 pF load capacitor for 500 ms of X-ray exposure, with X-ray source at 90 kVp and 25 mAs.

advantage of this scheme was the reliable co-assembly of the diode with read out electronics. This is particularly important for the measurement accuracy, in view of the small size of signals involved.

The sensing element and read out electronics were housed in a specially designed shielding box. This shielding is essential not only to prevent electromagnetic interferences degrading the signal, but also to shield the read out electronics from direct x-ray exposures (Fig. 5.11).

5.6   Experimental Results

Typical X-ray measurement results of a $(200\mu m)^2$ Mo/a-Si:H Schottky diode operated at 2 V reverse bias are illustrated in Fig. 5.12. These confirm the linear response of the detector to the number of absorbed photons, obtained from XRAYLIB. Similar studies on the detector using various X-ray source currents with a constant X-ray source voltage also verified the linear response with the number of absorbed photons. The efficiency of the detector, which is shown in Fig 5.13, particularly improves at low X-ray voltages $(\approx 40 - 60\ kVp)$.

Figure 5.14 illustrates the impact of the Mo thickness on the performance of the detector. At low thicknesses, the performance is limited by the absorption of X-ray photons inside Mo layer. An increase in the thickness of Mo leads to an increase in the number of absorbed photons, hence the output signal. However, beyond an optimum thickness, the number of electrons reaching a-Si:H depletion region is limited by the scattering and absorption inside the Mo film. For the X-ray source voltage of 60 kVp, it is found that a thickness of Mo around $\approx$ 500 nm yields the optimum performance. At higher energies, this optimum thickness moves to thicker films.
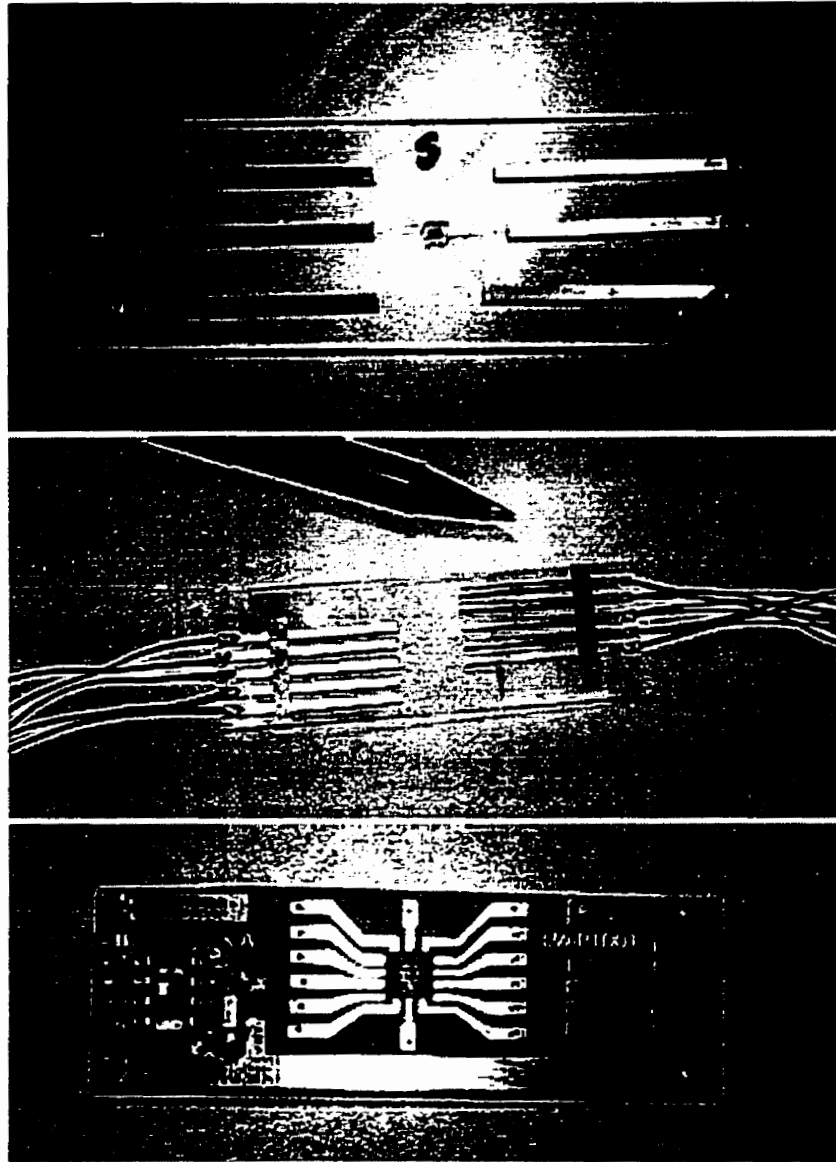
Figure 5.10: Various packaging designs used in characterization: initial glass holder design (top), improved glass holder with protective copper lines (middle), and the pc-board (bottom).
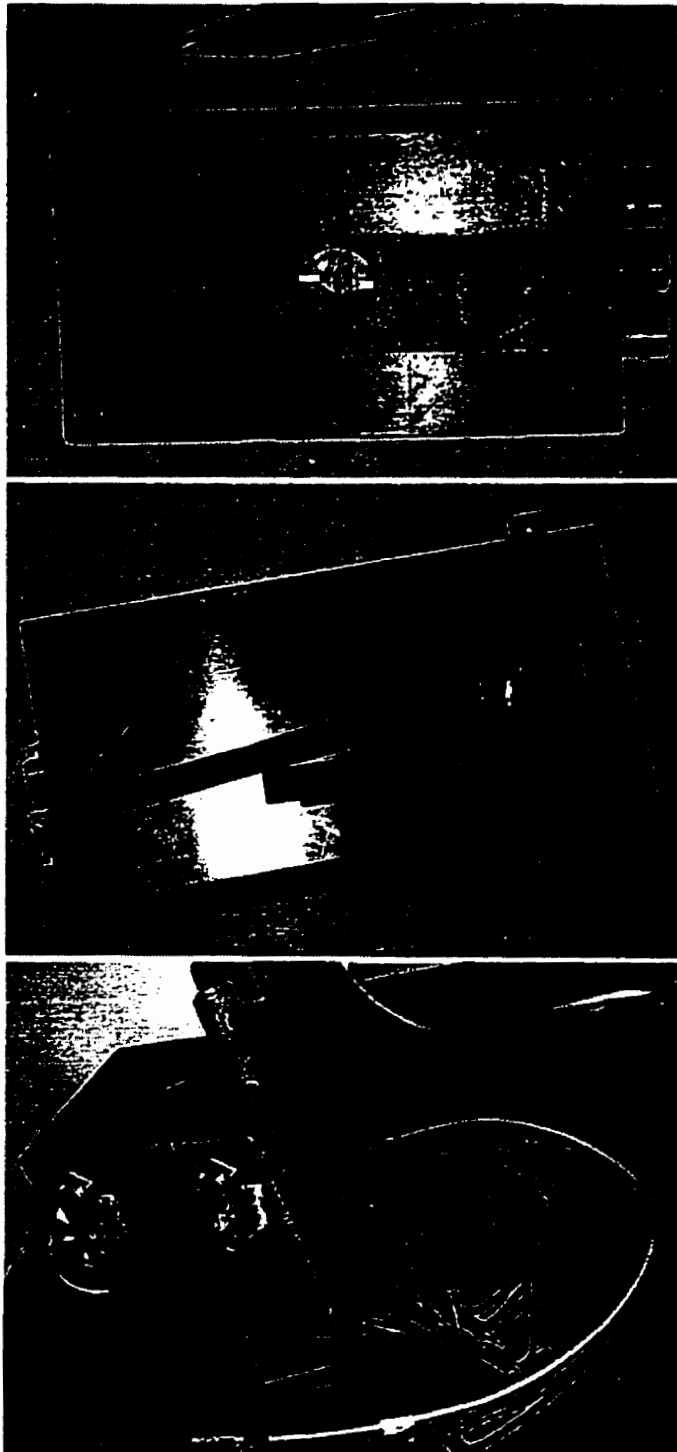
Figure 5.11: Various metal shield enclosures used in characterization: initial lead box (top), thin copper box (middle), and thick copper cage (bottom).
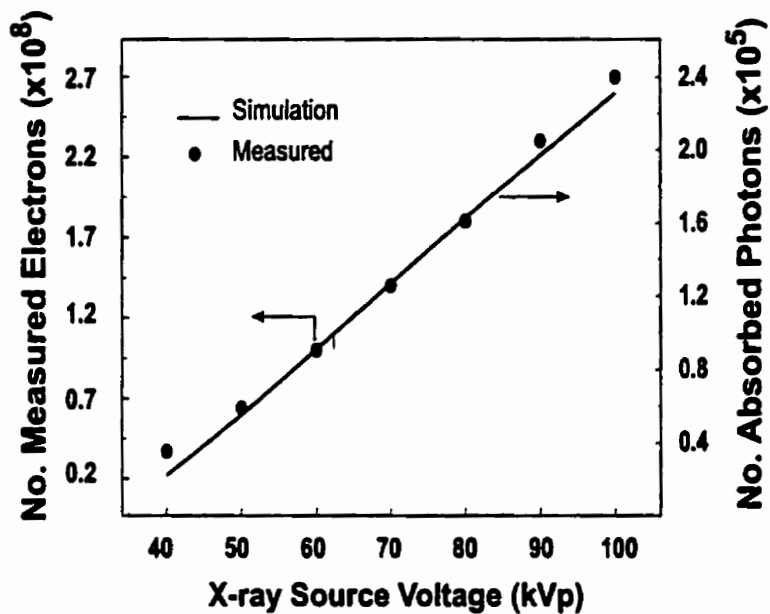
Figure 5.12: Response of detector for various X-ray source voltages (kVp), collected over a period of 500 ms.

Figure 5.13: Response of detector for various X-ray source voltages (kVp) normalized to the number of incoming photons, collected over a period of 500 ms and 25 mAs.

Figure 5.14: Variation of detector response with thickness of Mo layer, taken at 60 kVp and 25 mAs. The extrinsic quantum yield is defined as the ratio between numbers of measured electrons and the incoming X-ray photons.
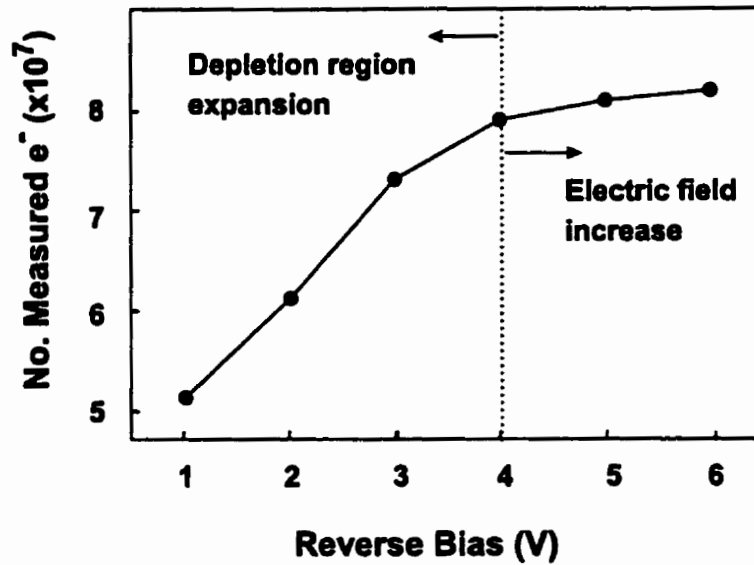
Figure 5.16: Measured number of electrons for various reverse voltages, at 60 kVp and 25 mAs.

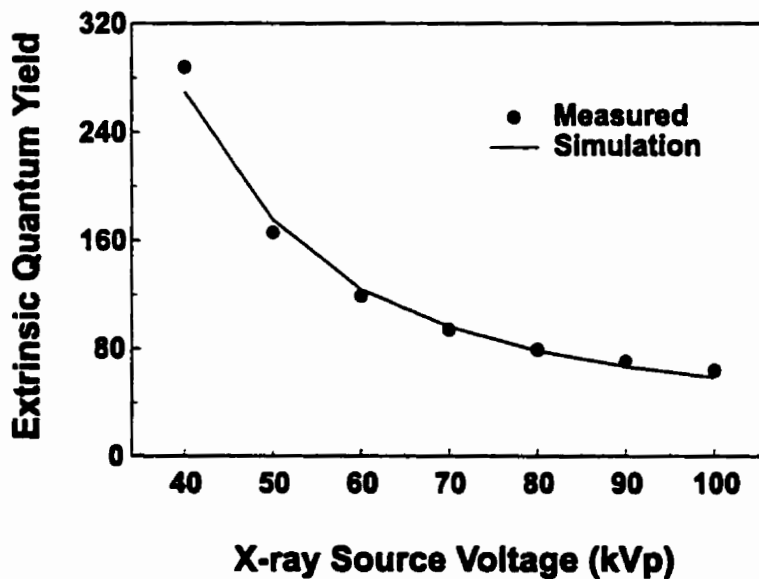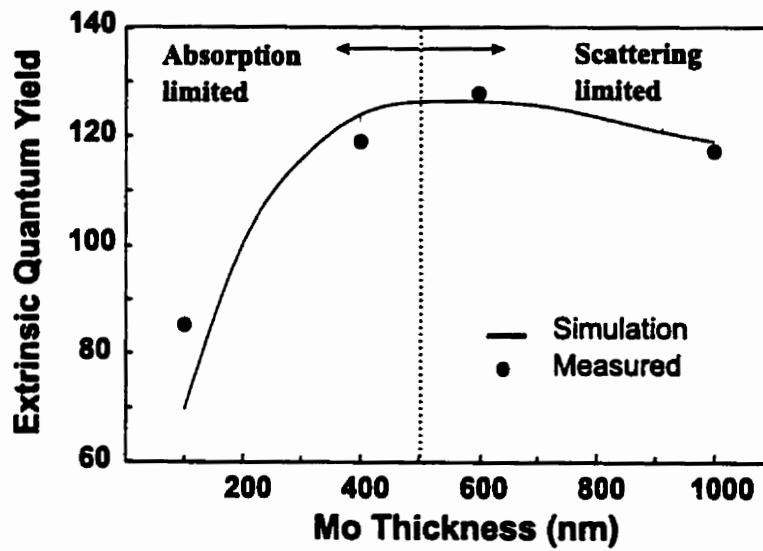operating X-ray detectors at different biases. Fig. 5.16 illustrates the variation of number of collected electrons with the applied bias. At low voltages, the signal increases with the square root of the applied reverse bias. Here, the depletion width expands and the generated e-h pairs are separated more effectively by the electric field inside the depletion region. The continued increase in signal at higher biases is the result of further increase the electric field inside the device and the consequent enhancement of charge collection.

The impact of the detector geometry on the performance was also investigated. However, the differences in the separation efficiencies prevent a meaningful comparison between the performance of detectors with different areas. In such cases, not only does the depletion capacitance increase with area, but the leakage current also grows with area leading to a lower potential across the detector. Both of these mechanisms can contribute to a lower separation efficiency.

The detector characteristics are summarized in Table 5.2 based on studies of noise,

Electrical noise	$\approx 8 \times 10^5$ electrons
Stability	$\approx 10^7$ electrons
Detector saturation	$\approx 5 \times 10^8$ electrons
Dynamic Range	50 : 1

Table 5.2: Various detector characteristics expressed in no. of electrons; time period 500 ms.

leakage, and X-ray sensitivity from previous chapters.

Chapter 6

Conclusion

In this thesis, we demonstrate the feasibility of a novel direct X-ray detection scheme based on heavy metal/amorphous silicon Schottky diodes for large area X-ray imaging applications. This approach does not require an extra layer for conversion of X-rays to visible light, or a thick layer of selenium.

The effects of deposition conditions, material properties, and interface properties have been studied to determine the material most suitable for detector fabrication. We chose Mo as the Schottky metal since it has full compatibility with the standard thin film transistor fabrication process, high temperature stability, low mechanical stress, and a smooth interface.

In terms of electrical stability, it has been determined that the operation of the detector at low biases yields the minimum time-dependence of the reverse current. At medium biases, the time-dependent variations of the reverse current are noticeably larger, and mainly originate from variations of the Schottky energy barrier. Therefore from stability standpoint, the use of metals which yield a higher Schottky barrier is desirable.

At low frequencies, the electrical noise is found to decrease with reverse current;

96

therefore, low voltage operation is also desirable for noise reduction. Moreover, it is found that the noise current PSD decreases with increasing detector area. However, this can potentially degrade the spatial resolution in large area applications.

The optimum Mo thickness is determined largely by the energy of X-rays. For low energies, the optimum value is about 500 nm, and thicker films are required at higher energies. In terms of a-Si:H thickness, it is found that a film with thickness of ≈ 1 μm produces the optimum performance. The optimum bias conditions are based on a compromise between stability, noise, leakage current, and signal. Although, a low bias results in stable characteristics, low noise, and low leakage current, it yields lower charge collection efficiency. At higher biases, the charge collection improves, but the stability, noise, and leakage current degrade. Employing other metals (e.g., W), would yield a larger barrier height with a-Si:H, thus allowing higher voltage operation to enhance charge collection. A larger barrier height would also result a wider depletion region and reduction in the density of trapped charges which yields stability improvements in the detector. This requires further work on deposition conditions, and in particular, on reduction of internal stress in deposited films.

Appendix A

Optical Absorption

The optical measurements have been performed using the setup shown in Fig. A.1.

The transmission intensity was first measured with a glass substrate, and then with the glass substrate and the thin layer of a-Si:H. The difference between these two measurements is proportional to the absorption in the film. However, this needs to be corrected to account for the reflectance occurring at the interfaces between the a-Si:H film/air, and a-Si:H/glass,

$$I = I_o(1 - I_{ref}) \exp(-\alpha_{opt} d). \tag{A.1}$$

Here, I is the transmitted intensity, I_o is the transmitted intensity without the film, I_{ref} is the reflected fraction, α is the optical absorption of the film, and d is the thickness of the film. For this configuration, the reflection can be shown by [76],

$$I_{ref} = \frac{r_{12}^2 + r_{23}^2 + 2r_{12}r_{23}\cos(\beta_a)}{1 + r_{12}^2 r_{23}^2 + 2r_{12}r_{23}\cos(\beta_a)}, \tag{A.2}$$

where

$$r_{12} = \frac{n_1 - n_2}{n_1 + n_2}, \tag{A.3}$$
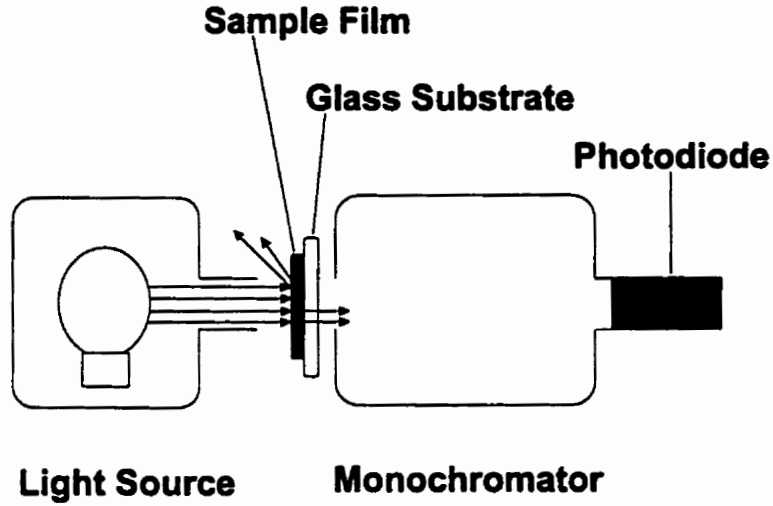
Figure A.1: The schematic of the optical setup used to measure the absorption coefficient of a-Si:H.

$$r_{23} = \frac{n_2 - n_3}{n_2 + n_3}, \tag{A.4}$$

$$\beta_a = 4\pi \frac{d}{\lambda} n_2, \tag{A.5}$$

where n_1, n_2, and n_3 are the refractive index of air, a-Si:H, and glass, respectively, and λ is the wavelength. Using $n_1 = 1.0$, $n_2 = 3.4$ [22], $n_3 = 1.544$ (Corning data sheet), and $\lambda = 600$ nm yields $I_{ref} = 0.21$. Incorporating this into the measurement results gives the dependence shown in Fig. A.2, which gives an optical band gap of 1.82 eV. This is in agreement with the values reported in ref. [22, 77].
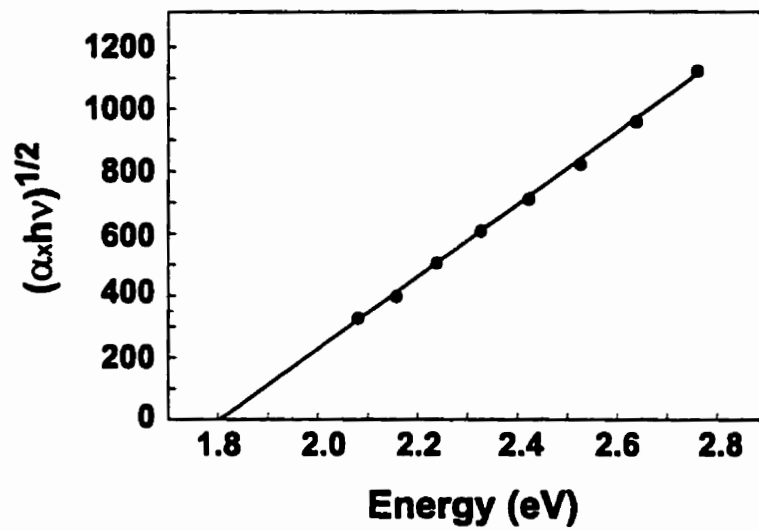
Figure A.2: The Urbach's plot for intrinsic a-Si:H.

Appendix B

Wafer Cleaning

All semiconductor wafers are subject to an initial cleaning in hot organic solvents to remove the residual impurities. The cleaning procedure used in this research for preparation of glass substrates are listed in Table B.1. This constitutes the first of two process steps known as RCA clean [78].

Step	Solution	Time (min)	Temp. (C)
1	$NH_4OH : H_2O_2 : H_2O$ 1 : 1 : 5	15	80°
2	H_2O	5	Room
3	H_2O	15	80°
4	IPA vapor	15	$60^\circ - 80^\circ$

Table B.1: Process steps used for initial cleaning of the glass wafers.

Bibliography

[1] F. H. Attix, *Introduction to Radiological Physics and Radiation Dosimetry*. New York: John Wiley & Sons, 1986.

[2] R. L. Weisfield, "High performance input scanning arrays using amorphous silicon photodiodes and thin-film transistors," in *Mat. Res. Soc. Symp. Proc. Amorphous Silicon Technology*, vol. 258, pp. 1105–1114, 1992.

[3] R. A. Street, X. D. Wu, R. Weisfield, S. Nelson, and P. Nylen, "Color document imaging with amorphous silicon sensor arrays," in *Mat. Res. Soc. Symp. Proc. Amorphous Silicon Technology*, vol. 336, pp. 873–878, 1994.

[4] J. Boudry and L. E. Antonuk, "Radiation damage of amorphous silicon photodiode sensors," *IEEE Trans. Nucl. Sci.*, vol. 41, no. 4, pp. 703–707, 1994.

[5] I. Fujieda, S. Nelson, R. A. Street, and R. L. Weisfield, "Radiation imaging with 2-D a-Si sensor arrays," *IEEE Trans. Nucl. Sci.*, vol. 39, no. 4, pp. 1056–1062, 1992.

[6] L. E. Antonuk, J. Boudry, W. Huang, D. L. McShan, E. J. Morton, J. Yorkston, M. J. Longo, and R. A. Street, "Demonstration of megavoltage and diagnostic X-ray imaging with hydrogenated amorphous silicon array," *Med. Phys.*, vol. 19, no. 6, pp. 1455–1466, 1992.

[7] L. E. Antonuk, J. Yorkston, W. Huang, J. Boudry, E. J. Morton, M. J. Longo, and R. A. Street, "Factors affecting image quality for megavoltage and diagnostic X-ray a-Si:H imaging arrays," in *Mat. Res. Soc. Symp. Proc. Amorphous Silicon Technology*, vol. 258, pp. 1069–1074, 1992.

[8] L. E. Antonuk, J. Yorkston, W. Huang, J. Boudry, E. J. Morton, and R. A. Street, "Large area, flat-panel a-Si:H arrays for X-ray imaging," in *SPIE 1896 Medical Imaging: Physics of Medical Imaging*, pp. 18–29, 1993.

[9] L. E. Antonouk, Y. El-Mohri, W. Huang, J. Siewerdsen, J. Yorkston, and R. A. Street, "A large area, high resolution a-Si:H array for X ray imaging," in *Mat. Res. Soc. Symp. Proc. Amorphous Silicon Technology*, vol. 336, pp. 855–860, 1994.

[10] L. E. Antonuk, J. Boudry, C. W. Kim, M. Longo, E. J. Morton, J. Yorkston, and R. A. Street, "Signal, noise, and readout considerations in the development of amorphous silicon photodiode arrays for radiotherapy and diagnostic X-ray imaging," in *SPIE 1443 Medical Imaging V: Image Physics*, pp. 108–119, 1991.

[11] H. Takahashi, K. Harada, M. Nakazawa, K. Hasegawa, K. Mochiki, Y. Hayakawa, and T. Inada, "Development of a new X-ray radiography system with 16 amorphous silicon linear sensors," *IEEE Trans. Nucl. Sci.*, vol. 40, no. 6, pp. 2026–2029, 1993.

[12] T. Jing, C. A. Goodman, J. Drewery, G. Cho, W. S. Hong, H. Lee, S. N. Kaplan, A. Mireshghi, V. Perez-Mendez, and D. Wildermuth, "Amorphous silicon pixel layers with cesium iodide converters for medical radiography," *IEEE Trans. Nucl. Sci.*, vol. 41, no. 4, pp. 903–909, 1994.

[13] L. E. Antonuk, J. Yorkston, W. Huang, J. Boudry, E. J. Morton, M. J. Longo, and R. A. Street, "Radiation response characteristics of amorphous silicon arrays

for megavoltage radiotherapy imaging," *IEEE Trans. Nucl. Sci.*, vol. 39, no. 4, pp. 1069–1073, 1992.

[14] R. L. Weisfield, R. A. Street, R. Apte, and A. Moore, "An improved page-size 127μm pixel amorphous silicon image sensor for X-ray diagnostic medical imaging applications," in *SPIE 3032 Medical Imaging: Physics of Medical Imaging*, pp. 14–21, 1997.

[15] W. Zhao and J. A. Rowlands, "A large area solid-state detector for radiology using amorphous selenium," in *SPIE 1651 Medical Imaging VI: Instrumentation*, pp. 134–143, 1992.

[16] W. Zhao, J. A. Rowlands, and S. Germann, "Digital radiology using self-scanned readout of amorphous selenium: design considerations for mammography," in *SPIE 2432 Medical Imaging: Physics of Medical Imaging*, pp. 250–259, 1995.

[17] D. L. Lee, L. K. Cheung, and L. S. Jeromin, "A new digital detector for projection radiolography," in *SPIE 2432 Medical Imaging: Physics of Medical Imaging*, pp. 237–249, 1995.

[18] K. Aflatooni, A. Nathan, and R. Hornsey, "A novel detection scheme for large area imaging of low energy X-rays using amorphous silicon technology," in *Technical Digest, 9th Int. Conf. on Solid State Sensors and Actuators, June 16-19*, (Chicago), pp. 3260–3262, 1997.

[19] K. Aflatooni, A. Nathan, and R. Hornsey, "a-Si:H Schottky diode direct detection pixel for large area X-ray imaging," in *Technical Digest, IEEE IEDM*, 1997. in press.

[20] Y. Naruse and T. Hatayama, "Metal/amorphous silicon multilayer radiation detectors," *IEEE Trans. Nucl. Sci.*, vol. 36, no. 2, pp. 1347–1352, 1989.

[21] I. Takayanagi, K. Nagai, H. Tetsuka, Y. Inoue, S. Araki, S. Mochimaru, Y. Iketaki, Y. Horikawa, and K. Matsumoto, "Amplified MOS imager for soft X-ray imaging," *IEEE Trans. Elec. Dev.*, vol. 42, no. 8, pp. 1425–1432, 1995.

[22] R. A. Street, *Hydrogenated Amorphous Silicon*. London: Cambridge University Press, 1991.

[23] A. M. Miri, *Development of a Novel Wet Etch Fabrication Technology for Amorphous Silicon Thin-Film Transistors*. PhD thesis, University of Waterloo, 1995.

[24] J. L. Vossen and W. Kern, *Thin Film processes II*. Academic Press, 1991.

[25] J. L. Vossen and W. Kern, *Thin Film processes I*. Academic Press, 1978.

[26] M. Shur and M. Hack, "Physics of amorphous silicon based alloy field-effect transistors," *J. Appl. Phys.*, vol. 55, no. 10, pp. 3831–3342, 1989.

[27] M. Hack, M. S. Shur, and J. G. Shaw, "Physical models for amorphous-silicon thin-film transistors and their implementation in a circuit simulation program," *IEEE Trans. Electron Devices*, vol. 36, no. 12, pp. 2764–2769, 1989.

[28] M. Shur, M. Hack, J. G. Shaw, and R. A. Martin, "Capacitance-voltage characteristics of amorphous silicon thin-film transistors," *J. Appl. Phys.*, vol. 66, no. 7, pp. 3381–3385, 1989.

[29] N. Kramer and C. V. Berkel, "Reverse current mechanisms in amorphous silicon diodes," *Appl. Phys. Lett.*, vol. 64, no. 9, pp. 1129–1131, 1994.

[30] R. A. Street, "Long-time transient conduction in a-Si:H p-i-n devices," *Phil. Mag. B*, vol. 63, no. 6, pp. 1343–1363, 1991.

[31] J. K. Aron and S. J. Fonash, "Origins of reverse bias leakage currents in hydrogenated amorphous silicon p-i-n detector structures," *Appl. Phys. Lett.*, vol. 60, no. 6, pp. 757–759, 1992.

[32] J. K. Aron and S. J. Fonash, "Using reverse bias currents to differentiate between bulk degradation and interfacial degradation in hydrogenated amorphous silicon p-i-n structures," *J. Appl. Phys.*, vol. 72, no. 9, pp. 4483–4485, 1992.

[33] R. Hornsey, K. Aflatooni, and A. Nathan, "Reverse current transient behavior in amorphous silicon schottky diodes at low biases," *Appl. Phys. lett.*, vol. 70, no. 24, pp. 3260–3262, 1997.

[34] K. Aflatooni, R. Hornsey, and A. Nathan, "Time dependence of the reverse current in amorphous silicon schottky diodes," in *Mat. Res. Soc. Symp. Proc. Amorphous Silicon Technology*, 1997. in press.

[35] H. Kida, K. Hattori, H. Okamoto, and Y. Hamakawa, "Measurement of deep states in undoped amorphous silicon by current transient spectroscopy," *J. Appl. Phys.*, vol. 59, no. 12, pp. 4079–4086, 1986.

[36] H. Scher and E. W. Montroll, "Anomalous transit-time dispertion in amorphous solids," *Phys. Rev. B*, vol. 12, no. 6, pp. 2455–2477, 1975.

[37] T. Tiedje and A. Rose, "A physical interpretation of dispresive transport in disordered semiconductors," *Solid state communications*, vol. 37, pp. 49–52, 1980.

[38] M. W. Carlen, Y. Xu, and R. Crandall, "Observation of slow dangling-bond relaxation in p-type hydrogenated amorphous silicon," *Phys. Rev. B*, vol. 51, pp. 2173–2179, 1995.
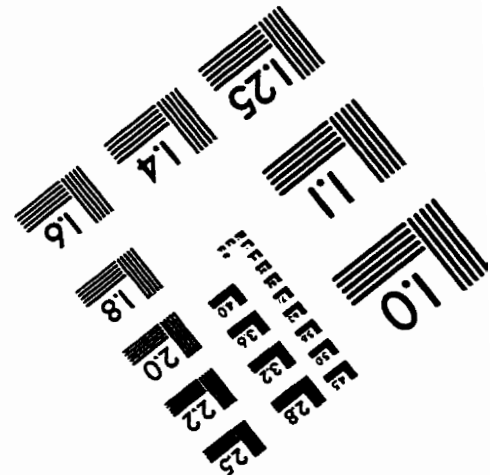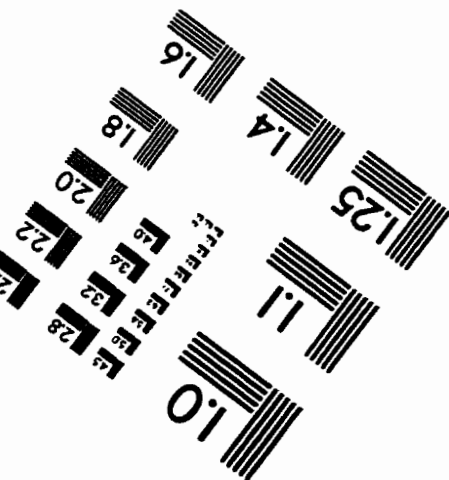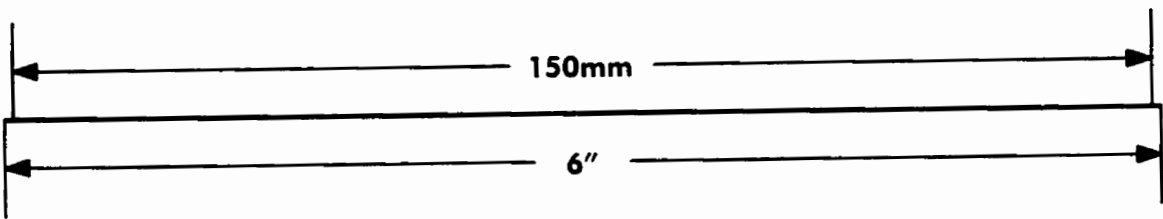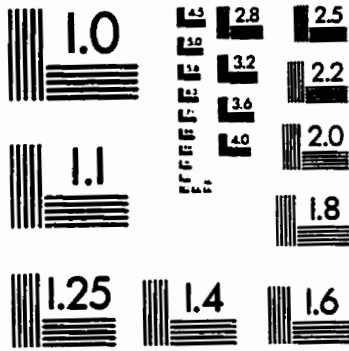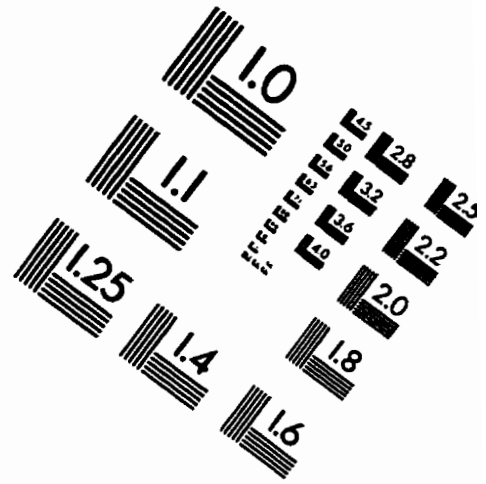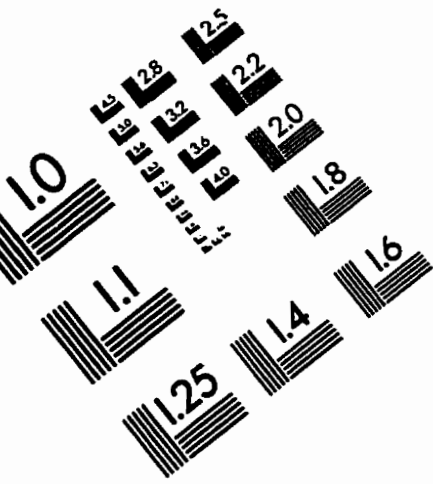
[39] S. M. Sze, *Physics of Semiconductor Devices*. New York: John Wiley & Sons Inc., 1981.

[40] S. Gasiorowicz, *Quantum Physics*. New York: John Wiley & Sons Inc., 1974.

[41] E. H. Rhoderick and R. H. Williams, *Metal-Semiconductor Contacts*. Oxford: Oxford Science Publications, 1988.

[42] K. J. B. M. Nieuwesteeg, M. van der Veen, and T. J. Vink, "On the current mechanism in reverse-biased amorphous-silicon Schottky contacts II. reverse bias current mechanism," *J. Appl. Phys.*, vol. 74, no. 4, pp. 2581–2589, 1993.

[43] K. J. B. M. Nieuwesteeg, M. van der Veen, and T. J. Vink, "On the current mechanism in reverse-biased amorphous-silicon Schottky contacts I. zero bias barrier heights and current transport mechanism," *J. Appl. Phys.*, vol. 74, no. 4, pp. 2572–2580, 1993.

[44] K. Maeda, W. Chiyoda, I. Umezu, and A. Kuroe, "Depletion layer width in undoped a-Si:H Schottky barrier revealed by reverse bias photocurrent," *J. Appl. Phys.*, vol. 75, no. 7, pp. 3522–3529, 1994.

[45] J. D. Cohen, T. M. Leen, and R. J. Rasmussen, "Observation of a novel relaxation process associated with electronic transitions from deep (D) defects in hydrogenated amorphous silicon," *Phys. Rev. lett.*, vol. 69, no. 23, pp. 3358–3361, 1992.

[46] J. Boudry and L. E. Antonuk, "current-noise-power spectra for amorphous silicon photodiode sensors," in *Mat. Res. Soc. Symp. Proc. Amorphous Silicon Technology*, vol. 297, pp. 975–980, 1993.

[47] K. Aflatooni, A. Nathan, and R. Hornsey, "Low frequency noise behavior in a-Si:H Schottky barrier devices," in *Mat. Res. Soc. Symp. Proc. Amorphous Silicon Technology*, vol. 420, pp. 747–752, 1996.

[48] F. R. Conner, *Noise*. London: Edward Arnold, 1973.

[49] M. Pentzand and M. Shott, *Handling Experimental Data*. Milton Keynes: Open University Press, 1989.

[50] F. N. H. Robinson, *Noise In Electrical Circuits*. London: Oxford University Press, 1962.

[51] A. H. W. Beck, *Statistical Mechanics, Fluctuations, and Noise*. London: Edward Arnold, 1976.

[52] M. J. Buckingham, *Noise In Electronic Devices And Systems*. New York: John Wiley & Sons, 1983.

[53] M. R. Spiegel, *Mathematical Handbook*. New York: McGraw Hill, 1992.

[54] K. K. Shung, M. B. Smith, and B. M. W. Tsui, *Principles of Medical Imaging*. London: Academic Press, 1992.

[55] H. E. Johns, *The Physics of Radiology*. Springfield: Charles C Thomas Publishing, 1966.

[56] E. F. Kaelble, *Handbook of X-rays*. New York: McGraw Hill Book Company, 1967.

[57] B. D. Cullity, *Elements of X-ray Diffraction*. London: Addison-Wesley Publishing, 1978.

[58] I. A Cunningham, Robarts Research Institute, University of Western Ontario, Canada, personal communications.

[59] D. M. Tucker, G. T. Barnes, and D. P. Chakraborty, "Semiempirical model for generating tungsten target x-ray spectra," *Med. Phys.*, vol. 18, no. 2, pp. 211–218, 1991.

[60] C. M. Davisson and R. D. Evans, "Gamma-ray absorption coefficients," *Rev. Mod. Phys.*, vol. 24, no. 2, pp. 79–107, 1952.

[61] D. B. Williams and C. B. Carter, *Transmission Electron Microscopy*. Plenum Press, 1996.

[62] W. R. Leo, *Techniques for Nuclear and Particle Physics Experiments*. Berlin: Springer-Verlag, 1994.

[63] K. Kanaya and S. Okayama, "Penetration and energy loss theory of electrons in solid targets," *J. Phys. D: Appl. Phys.*, vol. 5, pp. 43–58, 1972.

[64] International Commision on Radiation Units and Measurements (ICRU) Report No. 37, *Stopping powers for electrons and positrons*, 1984.

[65] Y. Kim and M. E. Rudd, "Binary-encounter-dipole model for electron-impact ionization," *Phys. Rev. A*, vol. 50, no. 5, pp. 3954–3967, 1994.

[66] J. C. Ashley, C. J. Tung, R. H. Ritchie, and V. E. Anderson, "Calculation of mean free paths and stopping powers of low energy electrons ($\leq$ 10 kev) in solids using a statistical model," *IEEE Trans. Nucl. Sci.*, vol. NS-23, pp. 1833–1836, 1976.

[67] T. M. Jenkins, W. R. Nelson, and A. Rindi, *Monte Carlo Transport of Electrons and Photons*. New York: Plenum Press, 1988.

[68] W. R. Nelson, H. Hirayama, and D. W. O. Rogers, *The EGS4 Code System*. Stanford Univeristy, Stanford, California: Stanford Linear Accelerator Center, 1985.

[69] L. Reimer, *Transmission Electron Microscopy*. Berlin: Springer-Verlag, 1993.

[70] D. C. Joy, A. D. Romig, and J. I. Goldstein, *Principles of Analytical Electron Microscopy*. New York: Plenum Press, 1986.

[71] T. A. Carlson, *X-ray Photoelectron Spectroscopy*. Stroudsburg: Dowden, Hutchinson & Ross Inc., 1978.

[72] S. Hufner, *Photoelectron Spectroscopy*. Berlin: Springer-Verlag, 1995.

[73] H. Raether, *Excitation of Plasmons and Interband Transitions by Electrons*. Berlin: Springer-Verlag, 1988.

[74] H. Ibach, *Electron Spectroscopy for Surface Analysis*. Berlin: Springer Verlag, 1977.

[75] R. A. Smith, *Semiconductors*. Cambridge: Cambridge University Press, 1987.

[76] C. Kittel, *Introduction to Solid State Physics*. New York: John Wiley & Sons, 1986.

[77] J. R. Reitz, F. J. Milford, and R. W. Christy, *Foundations of Electromagnetic Theory*. London: Addison-Wesley Publishing Company, 1979.

[78] J. Kanicki, *Amorphous and Microcrystalline Semiconductor Devices Vol. I & II*. Boston: Artech House, 1992.

[79] S. K. Ghandi, *VLSI Fabrication Principles*. New York: John Wiley & Sons, 1994.

IMAGE EVALUATION
TEST TARGET (QA-3)